VERTICAL INTEGRATION OF INKJET-PRINTED RF CIRCUITS AND SYSTEMS (VIPRE) FOR WIRELESS SENSING AND INTER/INTRA-CHIP COMMUNICATION APPLICATIONS

A Dissertation
Presented to
The Academic Faculty

By

Benjamin S. Cook

In Partial Fulfillment
of the Requirements for the Degree
Doctor of Philosophy
in
Electrical and Computer Engineering

School of Electrical and Computer Engineering
Georgia Institute of Technology
May 2014

VERTICAL INTEGRATION OF INKJET-PRINTED RF CIRCUITS AND SYSTEMS (VIPRE) FOR WIRELESS SENSING AND INTER/INTRA-CHIP COMMUNICATION APPLICATIONS

Approved by:

Dr. Manos M. Tentzeris, Advisor
Professor, School of ECE
Georgia Institute of Technology

Dr. Katherine Duncan
Research Scientist
U.S. Army

Dr. Gregory D. Durgin
Associate Professor, School of ECE
Georgia Institute of Technology

Dr. Hervé Aubert
Professor, ENSEEIHT
Institut National Polytechnique de Toulouse, France

Dr. Andrew Peterson
Professor, School of ECE
Georgia Institute of Technology

Date Approved: March 21st, 2014

ACKNOWLEDGMENTS

I would like to express my deepest gratitude to my advisor and mentor, Dr. Tentzeris, for his guidance and support during the last few years. Dr. Tentzeris has allowed me to grow as a researcher, and leader through encouraging independent thought, self-guidance, and leadership, which are invaluable skills. He has also been a great colleague and friend that I can always count on.

I would like to thank Dr. Edward Wheeler and Dr. Tina Hudson for inspiring me to pursue a career in research. Both of these people have had a major impact on my life over the last decade, and I wouldn't be where I am without them.

Most importantly, I'd like to thank my family, Peter, Lori, Kelsi, and Joshua Cook for being there every step of the way and encouraging me to not only do my best in research, but in life and relationships. Their support and love will never be forgotten.

TABLE OF CONTENTS

LIST OF TABLES

LIST OF FIGURES

SUMMARY

Inkjet-printing is a technology which has for the last decade been exploited to fabricate flexible RF components such as antennas and planar circuit elements. However, the limitations of feature size and single layer fabrication prevented the demonstration of compact, and high efficiency RF components operating above 10 GHz into the mm-Wave regime which is critical to silicon integration and fully-printed modules. To overcome these limitations, a novel vertically-integrated fully inkjet-printed process has been developed and characterized up to the mm-Wave regime which incorporates up to five highly conductive metal layers, variable thickness dielectric layers ranging from 200 nm to 200 um, and low resistance through-layer via interconnects. This vertically-integrated inkjet printed electronics process, tagged VIPRE, is a first of its kind, and is utilized to demonstrate fully additive RF capacitors, inductors, antennas, and RF sensors operating up to 40 GHz. In this work, the first-ever fully inkjet printed multi-layer RF devices operating up to 40 GHz with high-performance are demonstrated, along with a demonstration of the processing techniques which have enabled the printing of multi-layer RF structures with multiple metal layers, and dielectric layers which are orders of magnitude thicker than previoulsy demonstrated inkjet-printed structures. The results of this work show the new possibilities in utilizing inkjet printing for the post-processing of high-efficiency RF inductors, capacitors, and antennas and antenna arrays on top of silicon to reduce chip area requirements, and for the production of entirely printed wireless modules.

CHAPTER 1

INTRODUCTION

Ever since the advent of the printing press in the early 1400's in Mainz, Germany, printing has been an unequaled method of reproduction for manuscripts and artwork. The printing process, developed by a hand of entrepreneuring inventors including Gutenberg, Fust, and Schoeffer, in 1450 was a tightly guarded secret as it was the first technological development that enabled the comparatively cheap and rapid multiplication of manuscripts, which at the time were in high demand and commanded steep prices [1]. For nearly a decade, the process remained closely guarded within the printing guilds of Mainz, until the sack of the city in 1462. Following the sack of the city, the members of the printing guilds dispersed, and took the knowledge of the printing process with them. As the knowledge disseminated, printing took off like wildfire across Europe which enabled a new age of accessibility to knowledge and the literary arts [1, 2].

Just as the first printing press revolutionized the reproduction of manuscripts and books over half a millennium ago by drastically cutting costs and increasing production capacity, modern day inkjet-printers are revolutionizing electronics fabrication by allowing for faster, cheaper, more flexible, and more accessible methods to pattern and package electronic circuits and systems. Current methods of patterning electronics are typically subtractive, which require the selective removal of material from a bulk sheet to leave the desired pattern [3]. This selective removal, or etching, requires expensive masks which define the pattern to be etched, and harsh chemicals to remove the unwanted material. The masking and etching steps must then be repeated for each layer of patterned material that is deposited. This methodology makes subtractive processing time intensive, and creates a large amount of material and chemical waste. Inkjet printing, however, has the innate advantage of being a non-contact and additive fabrication and patterning process, meaning that the materials which are patterned to form the electronics systems are directly deposited in the desired

pattern in a layer-by-layer fashion [3]. This additive technique decreases fabrication time, eliminates the need for expensive masks, and also minimizes the material and chemical waste produced from the fabrication process.

The initial applications targeted by inkjet-printing are large-area, low-frequency electronics that benefit from reel-to-reel and roll-to-roll manufacturing which has been adapted from the newsprint industry. These applications include low-cost and disposable printed RFID tags for asset tracking [4–6], printed electrodes for solar cells and flexible screens [7–10], flexible single-layer printed circuit boards [6, 11, 12], and printed sensors and sensor arrays for large area and wearable electronics [11, 13]. However, just as the integrated circuit industry that was started by Jack Kilby in 1958 advanced from low-frequency, large-area circuits, to modern day nano-scale compact processes operating in the THz regime [14], inkjet-printed electronics, which is currently in its beginning stages, is seeing a push to reach higher frequencies, smaller and more compact vertically-integrated stack-ups, and cheaper and faster production.

One of the key target areas where inkjet-printed electronics have the potential to be a majorly disruptive technology in the next decade is the direct-write conformal packaging of RF systems deposited directly on-chip or on-package. This advancement will allow the printing of conformal antennas onto cell phone casings and automobiles, and post-processing of high-Q passives, high-efficiency antennas, and sensors directly on-chip to remove packaging costs and parasitics. To enable this breakthrough, advances in inkjet-printing are required. These advancements include moving from single-layer to multi-layer inkjet processes to enable higher levels of integration, optimizing the process to enable high efficiencies at RF by creating RF-process specific inks and stack-ups, and demonstrating vertically integrated printed RF components which operate into the mm-Wave regime.

1.1 Research Objectives

The objective of this dissertation is to demonstrate vertical integration of multi-layer inkjet-printed RF passives, antennas, and sensors which operate into the mm-Wave regime. Specifically, the dissertation encompasses:

1. The formulation and characterization of new conductive and dielectric inks which will be integrated into an inkjet-fabrication process for vertically-integrated multi-layer RF components

2. The creation and optimization of a low-cost, multi-layer metal-insulator-metal (MIM) inkjet-printed stack-up which can be used on virtually any substrate referred to as the VIPRE process (vertically-integrated printed RF electronics process)

3. The demonstration of multi-layer vertically-integrated inkjet-printed RF passives such as lumped components, sensors, and antennas which operate into the mm-Wave regime

1.2 Thesis Outline

This organizational structure of this Thesis is as follows:

1. Chapter 2 presents a background and comparative analysis on current additive and subtractive fabrication techniques used for RF components and packaging.

2. Chapter 3 presents an in-depth analysis of inkjet-printing fundamentals for electronics fabrication.

3. Chapter 4 presents ink formulation and process characterization for the multi-layer VIPRE process.

4. Chapter 5 presents the first demonstrations of printed RF vertically-integrated lumped components which are fabricated using the VIPRE process.

5. Chapter 6 presents the first demonstrations of printed vertically-integrated mm-Wave antennas and antenna arrays which are fabricated using the VIPRE process.

6. Chapter 7 presents an electronics-integrated microfluidics platform which is enabled by the VIPRE process, several microfluidic-integrated RF devices including varactors, tunable filters, and a wireless lab-on-chip are demonstrated.

CHAPTER 2

REVIEW OF TECHNIQUES IN ELECTRONICS FABRICATION

The first patents for electronics patterning techniques were filed in the early 1900's which defined methods of replacing hand-wiring of circuits with patterned conductive traces on an insulating surface - the basis of the modern-day printed circuit board (PCB), or printed wire board (PWB). By patterning the conductive traces directly onto an insulating board, circuits became much cleaner and easier to assemble for mass-production environments. These initial PCB's were typically produced by stamping traces out of copper foil and laminating them to a base substrate. Discrete components such as inductors, capacitors, and transistors were then soldered onto the boards. As PCB technology advanced, multi-layer boards, which enabled higher levels of integration, were created by stacking or laminating multiple PCBs together, and new patterning methods were introduced that were able to produce finer feature sizes.

This trend towards more compact integration led to the integrated circuit revolution in the 1950's which used similar patterning methods to not only pattern metal traces, but also insulators and active layers, which allowed for the complete integration of traces, lumped components, and transistors onto a single chip. This removed the need for bulky discrete components, and enabled scaling in device size and operating frequency. Until recently, these high-frequency patterned RF systems were fabricated using subtractive processes which are not conducive to low-cost, large-area, and flexible electronics. However, the recent introduction of additive processes, such as inkjet-printing, has brought a disruptive technology to the field of RF system fabrication. Additive processes have the potential to produce completely new types of RF systems which are flexible and conformal, lower-cost, larger area, and more environmentally friendly than traditional subtractively fabricated systems. The following section contains a comparative analysis of modern day additive and subtractive processes used in traditional RF system fabrication.

2.1 Patterning Techniques in the Electronics Industry

2.1.1 Subtractive Processing

2.1.1.1 Mechanical Milling

Mechanical milling is one of the simplest patterning methods used in the electronics industry. Fig. 1 shows a simplified version of the milling process in which a laminated metal cladding is selectively cut away from the host substrate by a rotary bit. Milling is an ex-

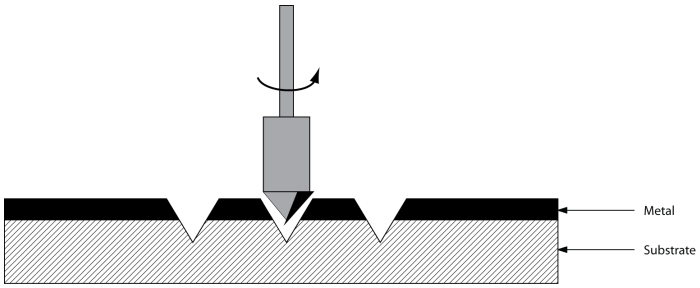

Figure 1. Mechanical milling of a single-sided copper clad laminate

cellent process for prototyping as no masks or stencils are required to transfer the pattern. Mechanical milling can cut away a broad range of materials including metals, ceramics, and oxides with feature sizes down to 200 um. The process can also be used to drill completely through the host substrate to create through holes or vias for multi-layer boards [15]. Mechanical milling creates rough or jagged edges which are caused by the mechanical rotation and ripping of the bit. ”V”-shaped trenches in the host substrate caused by the tapering of the bit can also cause problems at higher frequencies. If large-area boards are required, the processing time can be quite long, in excess of hours, depending on the amount of material removed [15].

2.1.1.2 Laser Ablation

Laser ablation, much like mechanical milling, is an excellent technology for prototyping environments as no masks or stencils are required for patterning. Patterning is performed by a high power ultraviolet (UV) or infrared (IR) laser that passes over the host substrate as shown in Fig 2.

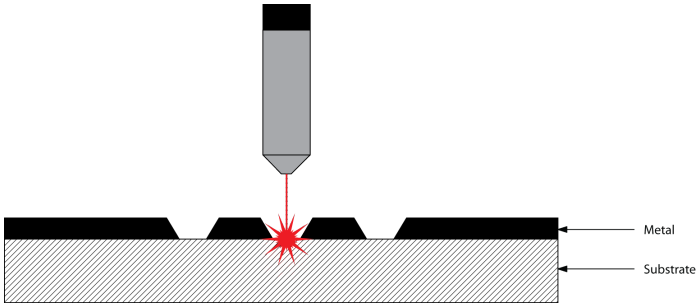

Figure 2. Laser ablation of a single-sided copper clad laminate

Laser ablation has several advantages over mechanical milling, including smaller feature sizes down to 20 um, and straighter, cleaner side walls [16]. With proper tuning, the process can leave the host substrate nearly un-touched. Like mechanical milling, laser ablation can be used to drill vias for multi-layer laminate boards. Because of the high precision of laser ablation, it has been used as a patterning tool in micro-fabrication applications [17]. Laser ablation is a slow process that requires the laser to scan over all regions of a material to be removed. During long fabrication runs, the change in temperature of the laser tube can cause a change in etching characteristics. One of the major disadvantages of laser ablation is that many materials release toxic gasses when vaporized by the laser. Ventilation and filtering systems are required to remove these hazardous gasses.

2.1.1.3 Photolithography

The most popular patterning technique used today for circuit fabrication is photolithography. The photolithography process shown in Fig. 3 begins with coating the material to be patterned with photoresist, which is a chemically initiated polymer which changes its chemical solubility upon exposure to UV light. After coating the surface with resist, a photo mask which selectively allows the passage of UV light, is used to pattern the resist layer. After exposure through the mask, the areas of photoresist which were exposed are removed in a developer bath. This opens a hole to the below layer which can then be removed via chemical, vapor, or reactive ion etching. The remaining photoresist is then removed using a chemical resist stripper.

Photolithography is able to pattern extremely fine features, currently in the range of several nanometers. These small feature sizes are what enable the extremely high levels of integration on modern day integrated circuits. A wide range of materials can be patterned including polymers, metals, oxides, and semiconductors. However, photolithography is a time and resource intensive process. For each patterned layer, material deposition followed by chemical etching is required, each of which are time intensive and create chemical waste. With modern day IC processes that require upwards of 10-20 patterned layers, the patterning time and chemical waste become appreciable.

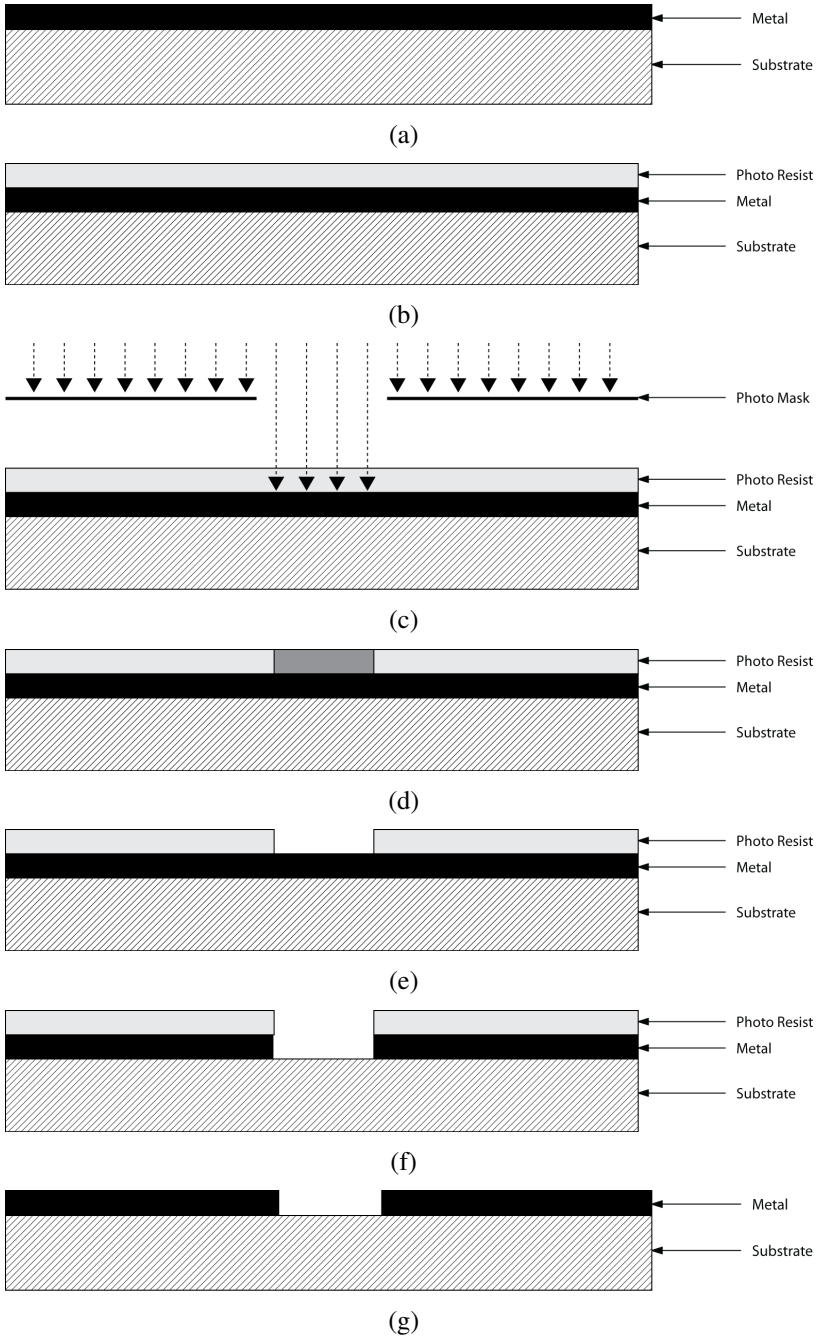

Figure 3. Photolithography fabrication process - (a) Blank wafer, (b) photoresist coating, (c) UV exposure, (d) photoresist solubility change, (e) photoresist development, (f) material etching, and (g) photoresist stripping

2.1.2 Additive Processing

2.1.2.1 Stamping/Microcontact Printing

Stamping, also called microcontact printing, bridges the gap between subtractive and additive processing. Stamping is very similar to the familiar stamp used for stamping letters and documents. To create the stamp, a master template is made, usually by subtractive processing of a silicon wafer. This is the only subtractive step in the process and must only be done once. A polymer which will form the final stamp is either spin coated, or pressed onto the master to create a negative of the master pattern. The polymer stamp is then peeled away from the master template. To pattern with the stamp, the stamp is dipped in an ink, or solution that contains the material to be patterned, and pressed against the host substrate.

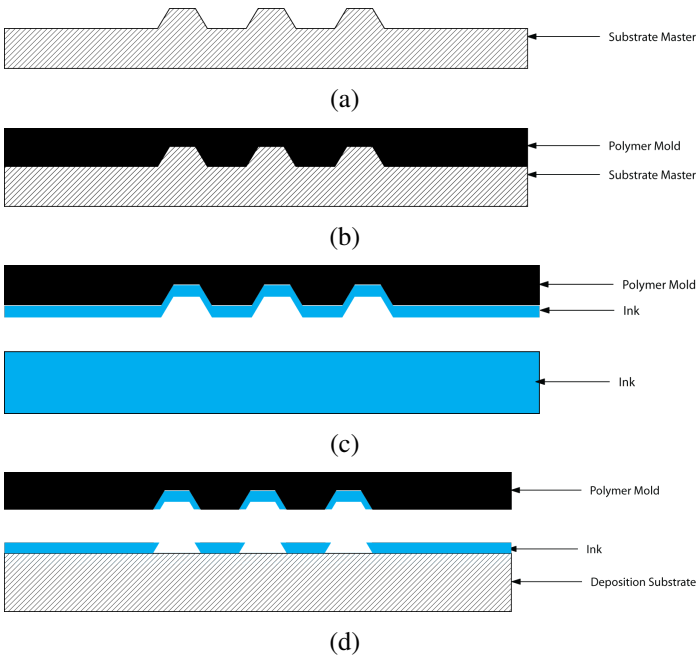

Figure 4. Stamping or microprinting process - (a) Master template, (b) forming a stamp from the master template, (c) dipping the stamp into an ink bath, and (d) contacting the stamp to the deposition substrate

Once the master for a stamping process is made, it is very easy to rapidly pattern large quantities of devices as large areas can be patterned at once, and a single stamp can be

re-used many times. Stamping is commonly used to directly pattern photoresist without the need for masks or UV exposure as current stamping techniques can realize feature sizes of 100 nm or less [18]. Stamping has the disadvantage of being a contact printing process, making patterning multiple layers on top of one another, and controlling layer thickness difficult.

2.1.2.2 Gravure Printing

Gravure printing, also known as flexographic printing, shown in Fig. 5, is the mass-production adaptation of microcontact printing. Gravure printing is most commonly used in the newsprint industry. To transfer a pattern, a gravure roller, which is a cylinder engraved with the negative of the desired pattern spins in an ink bath. As the gravure roller rotates, a doctor blade wipes off the excess ink. When the roller comes in contact with the substrate, the pressure from the pressure roller causes the ink to be transferred onto the substrate.

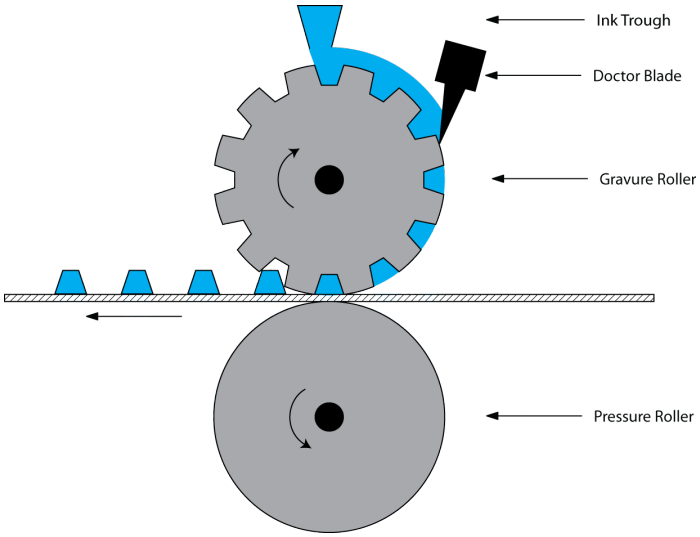

Figure 5. Gravure printing for mass-production environments

The rolling nature of gravure printing allows substrates to be patterned at extremely rapid rates on the order of meters per second. Several gravure rollers can be placed in succession to pattern multiple material layers in a rapid series deposition process with feature sizes of 5-10 um [19]. Gravure printing is not typically used for small-volume

runs as the process is complex and requires large volumes of ink to feed the gravure rolls. However, it is currently the fastest and most reliable additive process for large-volume manufacturing.

2.1.2.3 Screen Printing

Screen printing, up until recently, was the most common additive fabrication technique for electronics. The screen printing process shown in Fig. 6 begins with the creation of a silk screen mask which is a patterned mesh. The mesh is left open where the pattern is to be deposited, and blocked elsewhere. The mask is placed over the host substrate, and ink is deposited onto one side of the mask and pushed across with a squeegee. As the ink passes over holes in the mesh, it is pushed through and deposited onto the substrate in the desired pattern. To pattern multiple layers, a new mask is placed over the host substrate and the process is repeated.

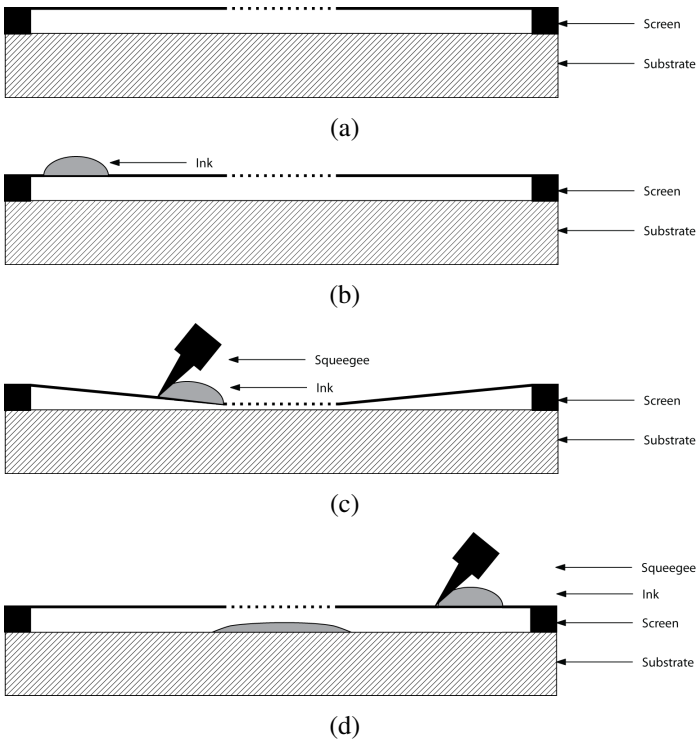

Figure 6. Screen printing process - (a) Silk screen mesh mask placed over substrate, (b) ink deposited onto mask, (c) squeegee slides ink across mask, and (d) ink is deposited through mask holes

Screen printing, like microcontact printing, can deposit a wide variety of materials including conductive inks, dielectrics, oxides, ceramics, and semiconductors with feature sizes down to 50 um [20–23]. While screen printing is an additive process, it still requires the creation of masks, though they are much cheaper than those for photolithography. Screen printing also requires excess ink to cover the entire mask which produces material waste.

2.1.2.4 Inkjet Printing

Inkjet-printing is a process which revolutionized the in-home printing industry in the 1990's, and has received a great amount of interest in the electronics industry over the last decade. Unlike the other additive deposition methods, inkjet-printing is a direct, non-contact patterning technique which does not require masks or stencils, and minimizes wasted ink. The inkjet process, shown in Fig. 7, utilizes an ink reservoir connected to an actuator to deposit discrete drops of ink as the nozzle passes over the host substrate. To pattern multiple materials, multiple nozzles can be used in parallel to directly deposit several materials in a layer-by-layer fashion.

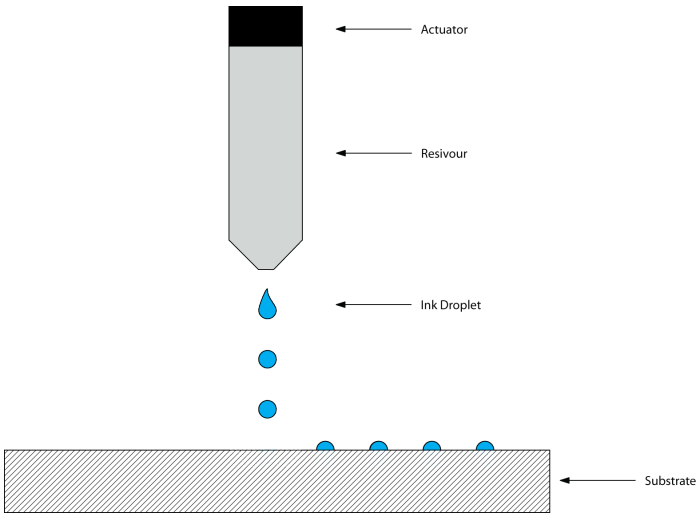

Figure 7. Inkjet-printing using drop-on-demand technology

Inkjet-printing can pattern a wide variety of materials including conductors, dielectrics,

ceramics, oxides, and semiconductors at feature sizes down to 1 um [3, 24–26]. Inkjet-printing is a non-contact deposition process which means it does not require contact with the host substrate to deposit patterned materials. This makes patterning flexible and delicate substrates simple, and does not disturb previously patterned layers. A wide array of variables including ink formulation, ink/substrate interactions, and drying and curing processes must be taken into account to create a working process. This makes inkjet-printing is a difficult process to tune, especially when multi-layer processing comes into play.

2.2 Process Comparison

A comparison of the patterning processes discussed in this chapter is displayed below in Table 1 [3, 15–27].

Table 1. Comparison of additive and subtractive patterning techniques [3, 15–27]

Technology	*Feature Size (um)*	*Multi-Layer*	*Cost*	*Speed*	*Waste*	*Area (m^2)*
Milling	200	No	Low	Slow	High (Dust)	0.1
Laser Ablation	20	No	High	Slow	Medium (Vapors & Dust)	0.05
Photolithography	.01	Yes	High	Slow	High (Chemical)	.66
Microcontact Printing	.1	Yes	Medium	Medium	Negligible	0.01
Gravure Printing	5 - 10	Yes	High	Fast	Medium (Excess Ink)	∞
Screen Printing	10 - 20	Yes	Medium	Fast	Low (Excess Ink)	0.8
Inkjet Printing	1-20	Yes	Low	Fast	Negligible	∞

Each process has distinct advantages for specific applications. Additive processing has shown many advantages when it comes to the low-cost patterning of large-area flexible

and vertically integrated electronics. Of current additive processes, inkjet-printing demonstrates comparatively small features at an extremely low-cost, with minimal waste, and allows for non-contact multi-layer patterning. Inkjet-printing can also be easily scaled to mass production, and large-area printing. It is because of these reasons that inkjet has become the recent focal point of low-cost electronics fabrication industry, and will be the focus of this proposal.

CHAPTER 3

REVIEW OF INKJET-PRINTING TECHNIQUES AND PROCESSING

Inkjet printing is conceptually a relatively simple process. An ink is loaded into a reservoir which feeds a nozzle. This nozzle is moved horizontally over a substrate and an actuator is used to eject a drop of ink from the nozzle. The ink droplet then hits and adsorbs to the surface of the substrate as seen in Fig. 7. By determining when drops are ejected as the nozzle passes over the substrate, patterned features are created.

However, while the theory of operation is simple, the details that go into making a successful and reliable process for inkjet-printed multi-layer RF electronics, or any inkjet-printing process for that matter, are quite complex. Key factors that must be tuned to create a successful printing process for RF electronics include:

- Nozzle type and characteristics (Piezo, Thermal, Electrostatic, Acoustic, Actuation Waveform)
- Ink formulation (Material Loading, Viscosity, Surface Tension, Carrier Fluid)
- Substrate or top-layer surface properties (Roughness, Free Surface Energy, Ink Chemical Compatibility)
- Post-Print Curing (Drying Pressure and Temperature, Thermal Annealing, UV Exposer, Laser Annealing)

Inkjet-printed electronics are still in the early stages of development, and key areas of research are targeting nozzle design to obtain smaller feature sizes, ink formulation to produce better conductive inks and dielectrics to allow for higher frequency operation, and substrate modification to provide better printing surfaces for electronic inks. This section presents an in-depth look at current inkjet-printed electronics technology.

3.1 Inkjet Printing Modalities

There are two distinct modes of inkjet-printing as displayed in Fig. 8 - Continuous which is used in industrial and mass-production environments, and Drop-on-Demand (DOD) which is used in small-volume and prototyping environments [3, 28].

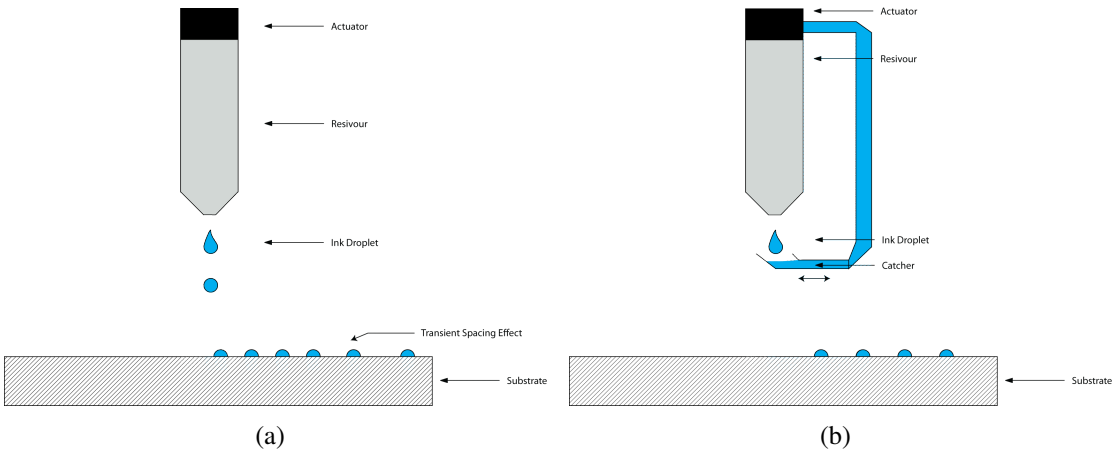

Figure 8. Printing Modalities - (a) Drop-on-Demand, and (b) Continuous Inkjet

3.1.1 DOD Inkjet-Printing

DOD printing shown in Fig. 8(a) is the most common printing modality used today in consumer and small-volume printers because of its simplicity. In DOD printing, the print nozzle is passed over the substrate, and an actuator ejects a droplet wherever patterned material is required. In areas where no material is required, the actuator does not fire. This method works very well for small-volume and prototype environments and is more flexible on the variety of inks it can jet. However, DOD printing suffers from transient effects upon actuator start-up and the increased risk of nozzle clogging due to ink drying when droplets are not being ejected.

3.1.2 Continuous Inkjet-Printing

For industrial environments where quality and cost are a crucial factor, continuous inkjet-printing shown in Fig. 8(b) minimizes transient and clogging issues. Continuous inkjet-printing continuously fires the actuactor at a fixed frequency to eject ink droplets. To perform patterning, a ”catcher”, which is a plate situated below the nozzle, actuates into and out of the path of the droplets only allowing the droplets to pass when pattern material is required. The catcher typically has an ink-recycling mechanism which then feeds the retrieved ink back into the ink reservoir.

3.2 Actuators and Inkjet-Printer Nozzles

The actuator that ejects the ink is the first critical variable to fix in the printing process as it determines the types of inks that can be used, as well as the feature size of the process. There are four common actuators used for inkjet-printing including thermal, piezo, electrodynamic, and acoustic actuators which are shown in Fig. 9 [3, 25, 26, 28].

3.2.1 Thermal

Thermal actuators are the most common of the inkjet-printing actuators and are well known for being the actuator of choice for consumer photo-printers as they are cheap and work with a wide range of inks. Thermal actuators work by triggering a heating element which is within or near the ink reservoir. As the ink increases in temperature in the area localized to the heating element, a phase transition of the ink occurs from liquid to vapor which causes a rapid volume expansion. This volume expansion increases the pressure in the cavity causing a drop to be ejected. Thermal inkjet nozzles are the cheapest and most reliable, but eject larger drops than the other actuators, which are in the range of 80 - 100 pL [3].

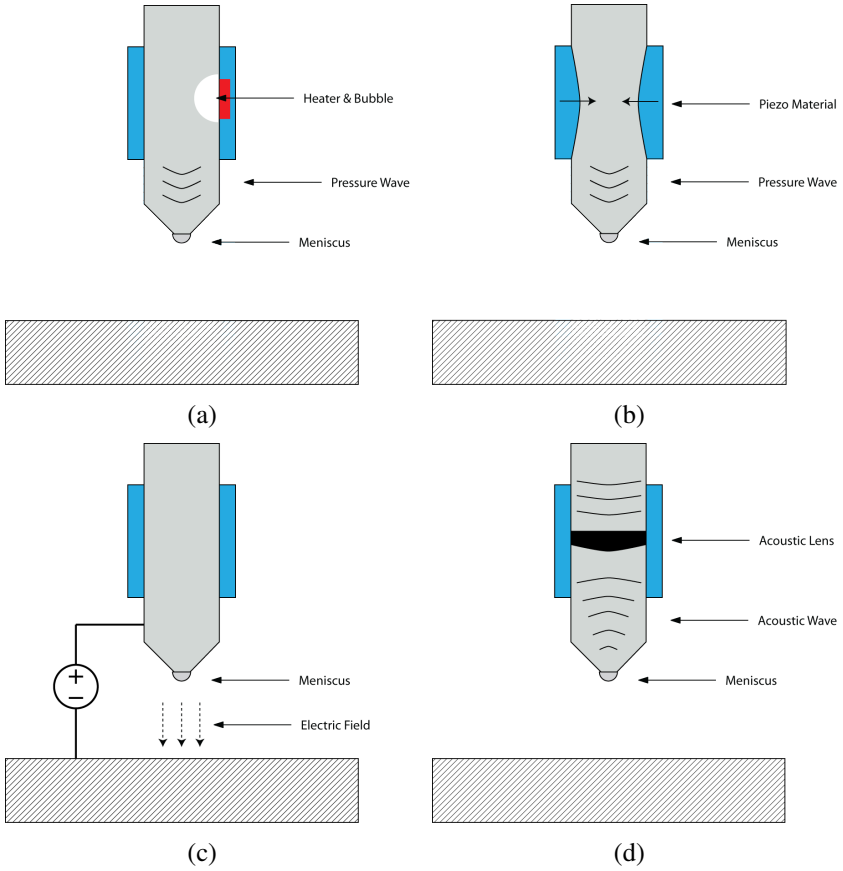

Figure 9. Inkjet Actuation Modalities - (a) Thermal, (b) Piezo, (c) Electrodynamic, and (d) Acoustic

3.2.2 Piezo

Piezo actuators are another commonly used type of actuator as they work with a wide variety of inks and produce much smaller droplets than thermal actuated inkjet nozzles. Piezo actuators work by placing a piezo material around, or inside the ink reservoir. To eject a drop, the piezo actuator is triggered to contract and expand which causes a build-up of pressure and then vacuum within the chamber allowing precise control on the formation of the drop. Because expansion and contraction can be controlled, drop volumes below 1 pL can be obtained [3]. However, small nozzle openings are required to obtain small drops which leads to eventual nozzle clogging.

3.2.3 Electrodynamic

Electrodynamic actuation of print nozzles is a method used when extremely fine feature sizes are required with the caveat that the ink contains free ions. To eject a drop, a voltage is applied between the nozzle, and a conductive platen on which the substrate rests as shown in Fig. 9(c). This voltage creates an electric field which causes the ions in the ink to accumulate near the meniscus at the opening of the nozzle thus deforming the meniscus into a cone. When the voltage is removed, the meniscus re-forms, ejecting a drop in the process. Electrodynamic actuation can produce drops with volumes below 1 fL which is much lower than other actuation methods [3, 25]. Because the electrostatic force breaks small holes in the meniscus, large nozzle openings can be used to prevent clogging while still obtaining extremely small feature sizes. However, electrodynamic inkjet systems work with only a single nozzle due electrical isolation issues between nozzles.

3.2.4 Acoustic

Acoustic actuated inkjet nozzles have the advantage of large nozzle openings to prevent clogging while still producing small feature sizes. To eject a droplet, an ultrasonic acoustic wave is focused onto the fluid meniscus using a lens. This concentration of acoustic energy causes a transient surface force which overcomes the surface tension of the meniscus for a short period of time allowing a drop to escape. By controlling the focal point of the lens, variable volume drops can be obtained in the 50 fL range [26]. However, to date, multiple acoustic nozzles have not been demonstrated working in parallel due to size constraints.

3.3 Electronic Ink Formulation for Inkjet-Printing

To fabricate multi-layer electronics using inkjet-printing, inks which can deposit metals, dielectrics, and in some cases semiconductors are required. The formulation of an electronic ink is a difficult and multivariate problem. First, a liquid carrier system which can disperse or dissolve the material to be patterned must be selected. This liquid carrier must be able to disperse or dissolve the material to be deposited while keeping the ink viscosity and surface tension within the range printable by the selected printer nozzle. The liquid carrier must also exhibit a high enough boiling point and low enough vapor pressure to avoid drying and clogging of the nozzle. On top of these requirements, the properties of the substrate, or material onto which the ink will be deposited must be considered to ensure there is good wet-ability, adhesion, and that there are no chemical interactions between the substrate/material and the ink.

3.3.1 Fluid Mechanics of Ink Formulation

Creating inks which are able to generate stable droplets for DOD inkjet-printing is a difficult process which requires the consideration of the physics and fluid mechanics of the formulated ink. The physical constants of the inks which must be considered are the Reynolds (Re), Weber (We), and Ohnesorge (Oh) numbers of the fluid which are defined as follows [29] where ρ is the density, η is the dynamic viscosity, γ is the surface tension, υ is the velocity, and a is the characteristic length, or radius of the droplet:

$$Re = \frac{\upsilon \rho a}{\eta} \tag{1}$$

$$We = \frac{\upsilon^2 \rho a}{\gamma} \tag{2}$$

$$Oh = \frac{\sqrt{We}}{Re} = \frac{\eta}{\sqrt{\gamma \rho a}} \tag{3}$$

Reis et al. found that the Ohnesorge number, which relates the viscous forces to inertial and surface tension forces of the ink is required to be in the range of $1 < Z < 10$ where $Z = 1/Oh$ [30]. At values of $Z < 1$, viscous dissipation prevents the drops from exiting the nozzle, and at values of $Z > 10$, multiple satellite drops are ejected with the primary drop.

Duineveld et al. found that another limiting factor in the formulation of high quality drops is the influence of the ink-air surface tension at the nozzle [31]. To overcome the surface tension at the boundary, a minimum energy is required which can be described by the Weber number which is the ratio between the inertial force and the surface tension force. Eq. 4 shows the criterion for the Weber number of the fluid where d_n is the nozzle diameter.

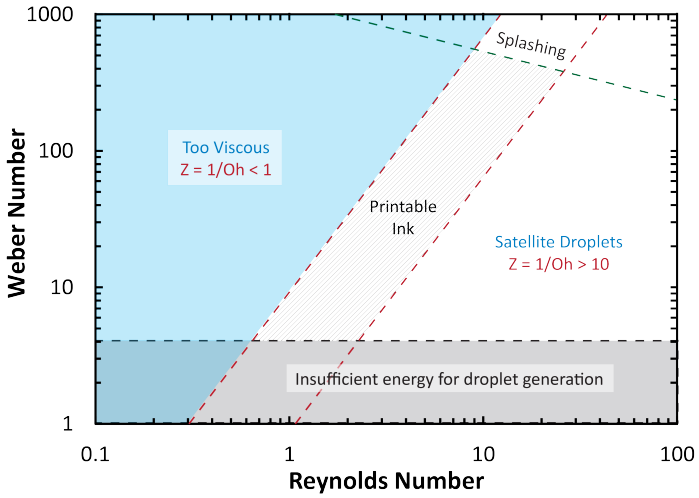

Figure 10. Mapping of physical properties of an ink to jettability and drop formation [29]

$$We = \upsilon_{min}\left(\frac{\rho d_n}{\lambda}\right)^{1/2} > 4 \tag{4}$$

A third criterion bounds the relationship between the Reynolds and Weber number to ensure that no splashing occurs when the drop impacts the substrate as described in Eq. 5 where f(R) is a function of surface roughness [32].

$$We^{1/2}Re^{1/4} > f(R) \tag{5}$$

By combining these three constraints, a map can be constructed to determine the optimal Weber and Reynolds number to obtain a jettable ink. The map shown in Fig. 10 is an excellent tool for selecting the solvent system used for creating electronic inks. By taking a closer look and extrapolating the effects based on individual variables, an ink tuning map can be constructed which is shown in Fig. 11. The two most important components of the ink, viscosity η and surface tension γ, are completely independent variables. By tuning γ, either by adding a co-solvent, or surfactant, one can move up and down the vertical axis, and by tuning the η by either adding a co-solvent or viscosity modifier, one can move left and right on the horizontal axis. The values for η and γ which move the ink into a printable range are dependent on $a, \rho, and \upsilon$. Once η and γ are set, changing the other three variables has very little effect on the printability of the ink.

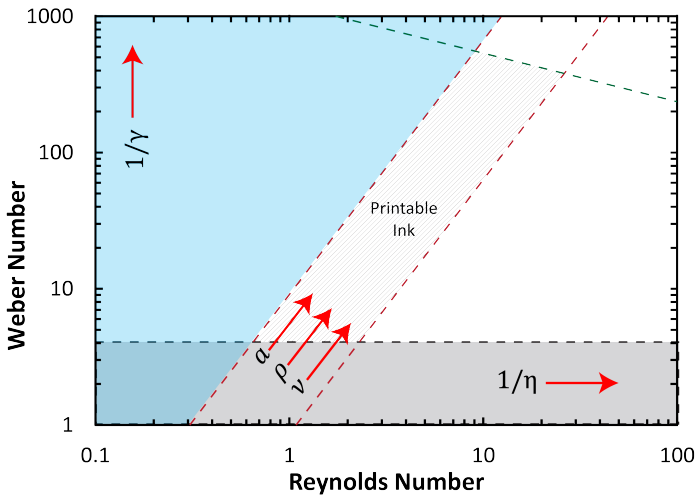

Figure 11. Mapping of physical properties of an ink to jettability and drop formation [29]

Taking these parameters into consideration, the typical formulation of an ink to meet these conditions is shown in Table 2. First, a liquid solvent is chosen which can dissolve/disperse the delivered material well. This solvent much have an adequate viscosity and surface tension for the nozzle used for the printer. The solvent must also have a high enough boiling point as to mitigate drying at the nozzle/air interface when not jetting. If these conditions cannot be met by using a single solvent, a co-solvent may be added which

is miscible in the primary solvent, and is also a low-medium solvent for the material to be delivered to modify the viscosity, surface tension, and boiling point/vapor pressure of the mixture [28, 33]. Surfactants and other additives such as dispersants and pH buffers may also be added when solvent systems alone cannot meet these conditions [28].

Table 2. Typical composition of an electronic ink

Component	**Purpose**
Solvent (50 - 80%)	Primary solvent and carrier fluid
Co-Solvent (5 - 50%)	Increase boiling point, modify surface tension,
Delivered Material (0.5 - 40%)	Key component, material that forms the final film
Surfactant (0 - 2%)	Modify surface tension, improve wetting characteristics
Others (1%)	Dispersants, pH Buffers, De-Foamers

3.4 Jetting and Drop Formation for Piezo-Based Inkjet Nozzles

After an ink has been formulated to meet the specifications of a selected DOD printer nozzle, adjusting the droplet formation, velocity, and volume are dependent on the nozzle temperature, and the jetting waveform which is applied to the piezo actuator.

3.4.1 Jetting Temperature

While it is preferable to jet at room temperature to avoid increased ink drying rates at the nozzle opening, the viscosity and surface tension of out-of-spec and hard-to-jet inks can be modified by varying their temperature. As temperature increases, both the viscosity, and surface tension of most fluids decrease [34, 35]. For example, water experiences a 50% decrease in viscosity, and a 10% decrease in surface tension by increasing the temperature form 25°C to 50°C.

3.4.2 Jetting Waveform and Fluid Density Effects

The majority of the work on drop formation and jet-ability comes in designing jetting waveforms for micron-sized piezo inkjet nozzles. Several analytic and numerical models are available in the literature which model the behavior of an ink within a piezoelectric print head. A typical waveform utilized in piezo inkjet print heads is shown in Fig. 12.

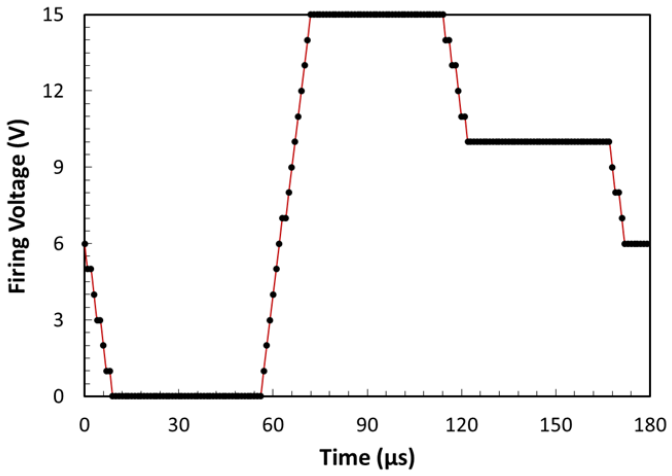

Figure 12. Model waveform for a piezo inkjet nozzle

The first progression of the waveform causes a contraction of the piezo which generates a negative pressure by increasing the volume in the fluid channel. This negative pressure wave propagates both towards the nozzle and towards the ink reservoir. These pressure waves are reflected at both the reservoir and nozzle which act as open and closed ends of the channel. When the negative pressure wave reflects off of the nozzle, it causes the meniscus to contract. Next, a positive pressure wave is applied by expanding the piezo actuator which superimposes a positive pressure wave on the reflected waves at the exact time that they reach the actuator. This causes the waves traveling towards the reservoir to cancel, and the waves traveling towards the nozzle to add constructively. This resonance causes a buildup of pressure which eventually allows for a drop to be ejected from the nozzle [36–39]. The resultant fluid flow is demonstrated in Fig. 13. In general, the speed of a pressure wave in a medium is expressed as:

$$\upsilon_p = \sqrt{\frac{K}{\rho}} \tag{6}$$

$$T_w = \frac{2X_{nozzle}}{\upsilon_p} \tag{7}$$

Where υ_p is the speed of the pressure wave, K is the modulus of elasticity, and ρ is the

fluid density. Therefore, the waveform must be tailored to have a period T_w such that it matches the time it takes for the pressure wave to travel twice the distance from the nozzle to the source of the pressure wave X_{nozzle} in a material with modulus of elasticity K, and density ρ.

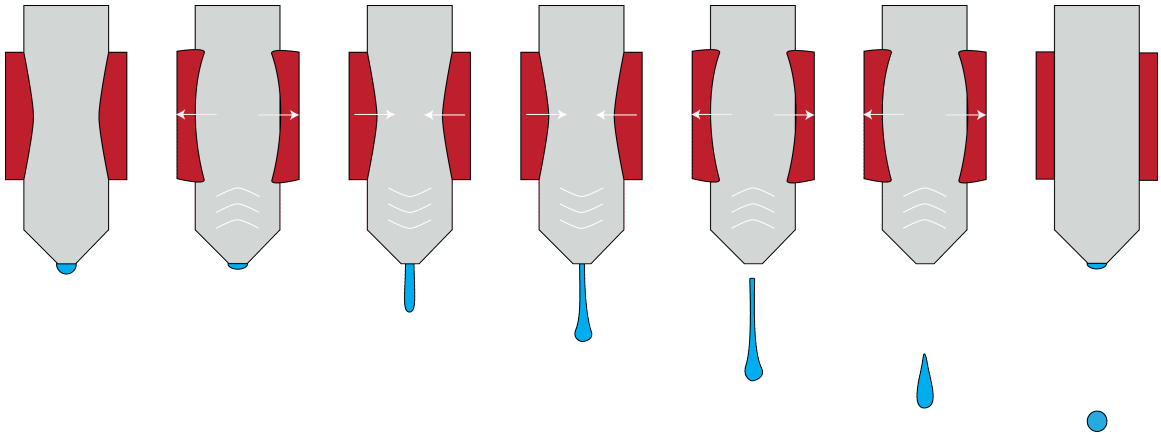

Figure 13. Dropplet progression for a standard piezo DOD print nozzle waveform

While Fig. 13 demonstrates ideal jetting performance for an ink which matches the requirements of a nozzle, inks which have an *Oh* number where $Z < 1$ will typically be unable to exit the nozzle due to viscous dissipation, or where $Z > 10$ will typically demonstrate satellite droplets as described in 3.3 shown in Fig. 14. However, even when an ink is in the ideal range, optimal jetting still requires tuning of the jetting waveform.

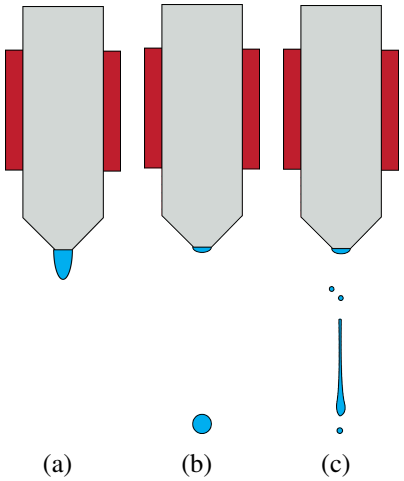

Figure 14. Drops where - (a) $Z < 1$**, (b)** $1 < Z < 10$ **(c)** $Z > 10$

3.5 Substrate Preparation for Inkjet-Printing

Once an ink is tuned for the specified printer nozzle, which has strict requirements on the fluid viscosity and surface tension, the properties of the substrate onto which the ink will be deposited must be considered to ensure proper wetting and feature formation. The critical parameters to consider for the substrate are the free surface energy (γ_{total}) which is related to the contact angle of the droplet on the substrate (θ_c), and the surface roughness.

3.5.1 Free Surface Energy and Contact Angle

The most important parameter of the substrate to consider for fluid wetting is the free surface energy. When a drop of liquid comes into contact with the substrate, surface forces are experienced at the solid-liquid boundary γ_{SL}, the solid-air boundary γ_{SV}, and the liquid-air boundary γ_{LV} as shown in Fig. 15. These forces are determined by surface tension of the ink γ_L, and the surface energy of the substrate γ_S.

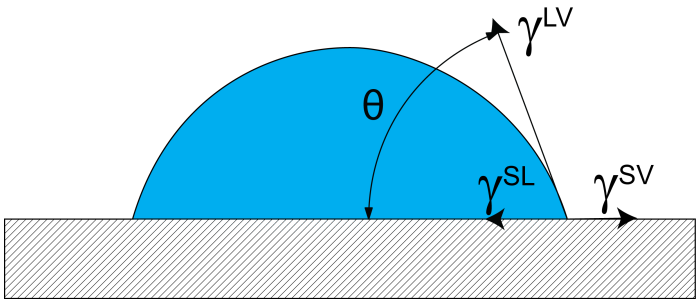

Figure 15. Surface tension and contact angle of a droplet on a substrate

The interaction of these three forces determine the contact angle of the droplet on the substrate as shown in Eqs. 8, and 9 [40]. The contact angle is directly related the wet-ability of the substrate.

$$cos(\theta) = \frac{\gamma_S - \gamma_{SL}}{\gamma_L} \tag{8}$$

$$\gamma_{SL} = \gamma_L + \gamma_S - 2\sqrt{\gamma_L \gamma_S} \tag{9}$$

By understanding the surface energy of the substrate and the surface tension of the fluid, the wetting behavior of the ink can be determined. When the surface energy of the substrate is much lower than the surface tension of the ink ($\gamma_S < \gamma_L$), poor wetting will occur and the ink will ball on the surface. As γ_S increases with respect to γ_L, the contact angle decreases until the critical surface tension γ_C is reached and the ink completely wets the substrate producing a uniform, flat film. This is depicted in Figs. 16 and 17.

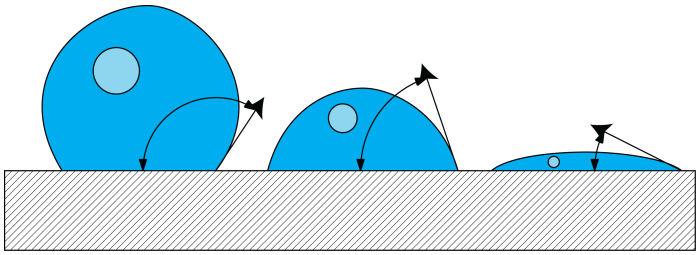

Figure 16. Contact angle based on differences in surface tension - Left to right: $\gamma_S < \gamma_L$, $\gamma_S \approx \gamma_L$, and $\gamma_S > \gamma_L \approx \gamma_c$

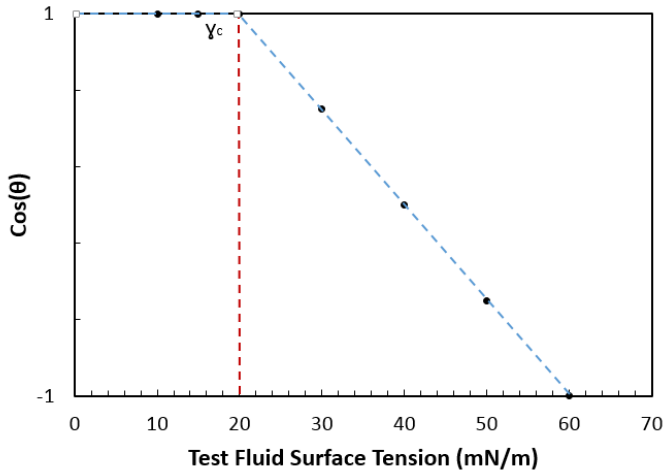

Figure 17. Critical surface tension plot of a substrate with a set surface energy

In order to properly wet the substrate, while not sacrificing feature size due to excessive ink spreading, the surface energy of the substrate should be tuned to be approximately 10 to 20 mN/m above the surface tension of the fluid, which yields a contact angle in the range of 10 to 15°. The final diameter of the drop, d_{final} can be determined by the drop volume and its contact angle with the substrate as described by Yarin et al. in Eq. 10.

$$d_{final} = d_0 \sqrt[3]{\frac{8}{tan(\frac{\theta eq}{2})(3 + tan^2(\frac{\theta eq}{2}))}} \tag{10}$$

The initial drop diameter in flight is d_0 and the equilibrium contact angle after the transient settling time is θ_{eq} [41]. When the equilibrium contact angle is 10°, d_{final} is approximately $3d_0$. The drop diameter on the substrate versus the contact angle is shown in Fig. 18. The higher the contact angle, the better the feature size obtainable becomes. However, this is a direct trade-off with wet-ability.

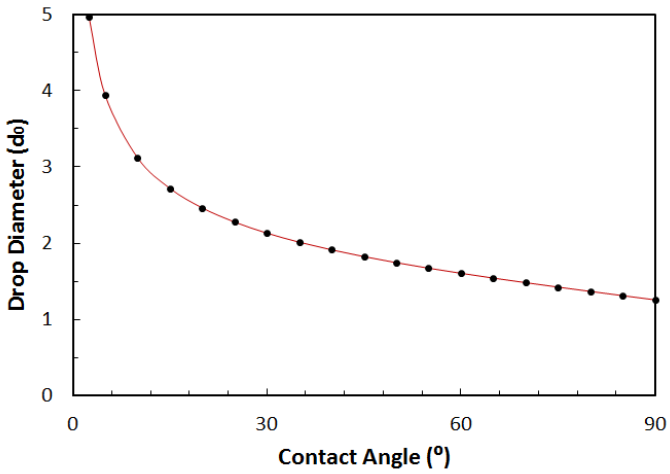

Figure 18. Drop size on substrate relative to the drop size in air versus contact angle

The printing of structures requires extending past printing individual drops to printing coalesced lines and features consisting of overlapping drops. When drops are overlapped, they tend to coalesce and form a continuous liquid bead. However, the spreading behavior of coalescing drops differs from that of an individual drop. At low drop spacing, where the drop spacing d_s is defined as the distance between the centers of two sequential drops and the spacing is much less than the drop diameter d_{final}, a printed bead becomes unstable and forms periodic bulges as surface tension of the fluid cannot hold the large amount of liquid in the bead. As the drop spacing increases, line stability increases until the drop spacing p nears the drop diameter d_{final}. At this point, scalloping occurs. As the drop spacing increases even further, individual drops appear.

Stringer et al. performed an analysis on line stability versus drop spacing and horizontal nozzle speed over the substrate [42]. Fig. 19 shows line formation regions versus normalized print head traverse speed which is defined as $U_T^* = \frac{\upsilon U_T}{\gamma_{LV}}$ where υ is the dynamic viscosity and U_T is the printhead speed in (m/s).

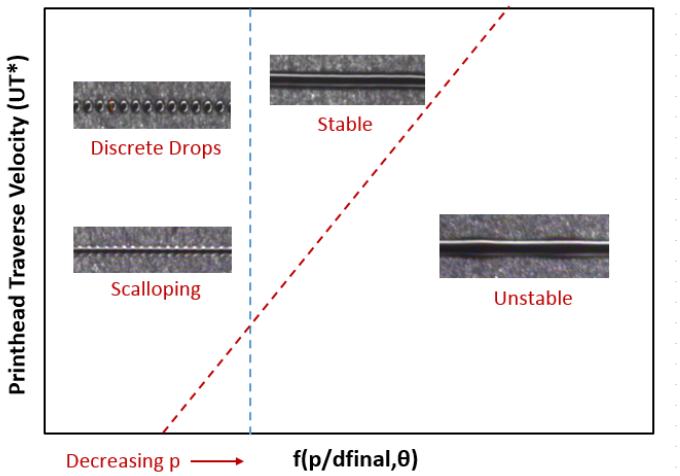

Figure 19. Stability of line formation versus print head speed and drop spacing

The maximum droplet spacing to create a line in the stable region, p_{max} is expressed in Eq. 11 where d_{final} is the drop diameter on the substrate, and θ_{eq} is the static or equilibrium contact angle [42].

$$p_{max} = \frac{2\pi d_0}{3d_{final}^2\left(\frac{\theta_{eq}}{sin^2\theta_{eq}} - \frac{cos\theta_{eq}}{sin\theta_{eq}}\right)} \tag{11}$$

Once the region is calculated in which line stability is achieved as shown in Fig. 19, the line width W can be calculated using Eq. 12.

$$W = \sqrt{\frac{2\pi d_0^3}{3p\frac{\theta_{eq}}{sin^2\theta_{eq}} - \frac{cos\theta_{eq}}{sin\theta_{eq}}}} \tag{12}$$

3.5.2 Free Surface Energy and Contact Angle Modification

Inkjet nozzles have a specific range of surface tension and viscosity for the ink under which conditions the nozzle will jet. Therefore, the surface energy of the ink cannot be changed

to ensure proper wetting and feature formation dependent on the substrate surface energy. To ensure that proper wetting and feature formation are obtained, the surface energy of the substrate must be set in the range of 10 - 20 mN/m above that of the ink.

Several methods have been demonstrated which allow for the modification of substrate surface energy to improve substrate print-ability for a given ink specification. If the surface energy of the substrate is too low to initially ($\gamma_S \leq \gamma_L$), several methods can be used to increase the surface energy including plasma excitation [43], UV Ozone [44], flame exposure, or chemical treatment with an acid. These methods work by breaking surface bonds to create dangling bonds which increase the net surface energy of the substrate. Self-assembled mono-layers (SAM) have also been demonstrated which bind to the substrate and for a thin monolayer which demonstrates a surface energy independent of the surface energy of the below substrate [45].

3.6 Temperature Effects on Inkjet-Printed Features

Once the ink has been deposited onto the substrate, solvent drying occurs at a rate based on the temperature of the substrate T_s, and the boiling point of the solvent $B.P._s$. In the case the boiling point of the solvent is much higher than the temperature of the substrate ($B.P._s \gg T_s$), the printed features will remain wet and slowly spread due to time-dependent advancing contact angles [46]. This is an unwanted situation as it increases feature size and causes blurring.

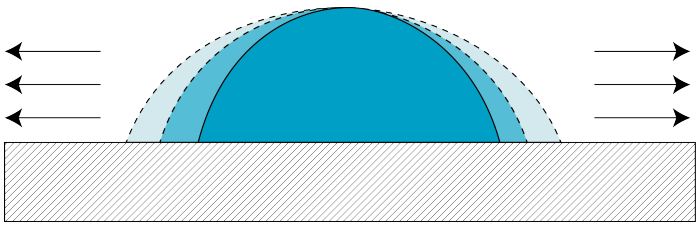

Figure 20. Advancing contact angle of ink droplet

The optimal drying conditions are when T_s is below $B.P._s$, yet high enough to cause controlled evaporation due to an increase in the vapor pressure of the solvent. In this case,

the drops are allowed to coalesce when they overlap, but the evaporation rate prevents drop spreading.

As T_s approaches $B.P._s$, rapid evaporation of the solvent occurs which causes coffee ringing of the droplets and produces films of individual dried droplets which do not flow together to form continuous features. The coffee ring effect is caused by a combination of faster evaporation at the edges of the droplet, and capillary action which draws fluid to the edges to replace the evaporating fluid [47–49]. This leaves larger deposits of material at the edges than at the center as shown in Fig. 21.

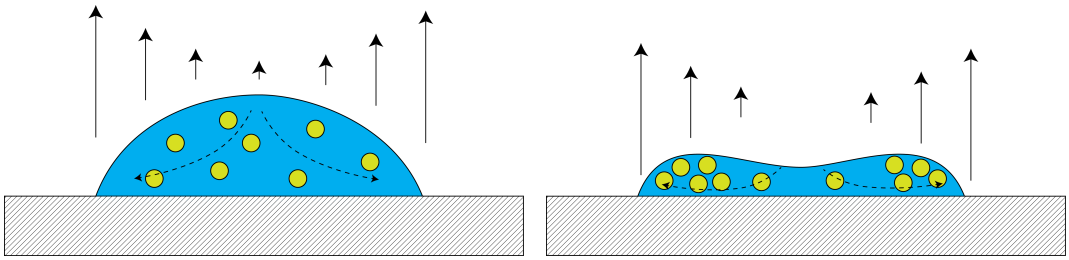

Figure 21. Coffee ring effect due to rapid solvent evaporation

The coffee ring also occurs when low w/w% of the loading material is present in the ink, or when highly volatile solvents with high vapor pressures are used. In this case, the use of a co-solvent can usually correct the issue.

3.7 Prior Art in Vertically-Integrated Inkjet-Printed RF Components

Until recently, the focus of inkjet-printed RF components research has been placed on exploring opportunities in low-cost, flexible, single-layer passive components such as antennas [11, 24, 50, 51] , filters [52–54], and planar lumped elements [55–58], on organic substrates such as paper or recyclable plastics. This initial work demonstrated the feasibility of inkjet-printed RF devices, and pushed the frequency of printed components to several GHz [24]. However, single layer processes lack the ability to reach the high levels of integration seen in modern IC processes, and little work has been done to bring together

both ink formulation and process characterization for RF, and the design of high frequency inkjet-printed RF components.

3.7.1 Conductive Inks

Highly conductive inks are essential to printed electronics, especially when fabricating high-frequency components. Initially, conductive inks were formulated by dissolving conducting polymers such as PEDOT:PSS, or carbon into a solvent that would yield films with low conductivities of 10^2 S/m [59,60]. However, these low conductivity solution-based inks were not feasible to use for high efficiency printed electronics. Chu et al. demonstrated one of the first depositions of silver by using a silver nitrate precursor in solution form which increased the conductivity of the deposited metal layer to 10^4 (S/m), however, temperatures in excess of 250°C were required to precipitate out the silver after printing [61]. The high temperatures required for these precursor-based inks eliminated the ability to print on polymer and organic substrates which are the main target for inkjet-printed electronics. Some of the first highly conductive inks that were able to be processed at low enough temperatures for polymer and organic substrates were demonstrated in early 2000 by Szczecha et al. and were made of metallic silver nanoparticle dispersions that could reach conductivities in excess of $5 * 10^5$ (S/m) with curing temperatures below 250°C [62]. Nano-scale particles exhibit a unique property in that the Eq. 13 where T_0 is the bulk melting temperature, σ is related to the thermal conductivity of the metal, and r is the radius of the particle.

$$T_m(r) = T_0(1 - \frac{\sigma}{r}) \tag{13}$$

Utilizing this property, recent works have demonstrated conductivities of silver nanoparticle ink on the order of $1.2 * 10^7$ (S/m), 5x lower than bulk silver, through creating smaller nanoparticles, and special curing techniques [24]. Current research is pursuing lower-cost conductive inks using materials such as copper and graphene; however, lower cost metals have issues with oxidation which prevent non-noble metallic nanoparticles from being used

without intert gas sintering environments.

3.7.2 Dielectric Inks

Creating vertically-integrated structures using inkjet-printing requires the printing of dielectric layers. The majority of the literature has focused on producing thin-film printed dielectrics for low-frequency printed transistor gates. These dielectrics are typically soluble organic polymers with relative permittivities (ϵ_r) of 3-5, loss tangents ($tan\delta$) in the range of .02-.05, and are approximately 100-500 nm thick when printed [63]. Several works have also demonstrated the printing of higher permittivity precursor-based ceramics with relative permittivities on the order of 1000 with thicknesses up to 400 nm [64, 65]. However, these higher permittivity inks require sintering at temperatures in excess of 1000°C which is too high for most flexible and large area applications. To enable high efficiency, wideband, vertically-integrated RF components, thicker and lower loss dielectrics are needed.

3.7.3 Laminate-Based Vertically-Integrated Structures

The first steps in integrating inkjet-printed structures into multi-layer systems was based on printing individual substrates and laminating them together with thin layers of glue, or bond ply sheets. In 2007, Kirschenmann et al. demonstrated an inkjet-printed proximity-fed laminate patch antenna operating at 5 GHz which allowed for much wider band operation than single-layer printed antennas [66]. Many other multi-layer printed laminates followed which demonstrated improved performance from the single-layer inkjet-printed RF devices. The multi-layer laminates allowed for wider bandwidth antennas [24, 67, 68] , higher valued capacitors and inductors [69, 70], and entirely new structures such as substrate-integrated waveguides (SIW) [71] which operated at higher frequency up to 12 GHz, and allowed for smaller, more compact design. However, the laminate technique requires the use of multiple substrate layers, is difficult to align, and poses problems for inter-layer connections and vias. These factors limit the maximum frequency of operation and the level of integration that can be obtained.

3.7.4 Direct-Write, Vertically-Integrated Structures

The real potential in inkjet-printed electronics is in the inherent ability to directly print multiple materials onto a single host substrate. Very little work has been presented in the literature on vertically-integrated inkjet-printed RF components. The first instances of vertically printed components in the literature are inkjet-printed MIM crossovers, capacitors, and inductors for low-frequency applications. In 2003, Liu et al. demonstrated a polymer capacitor [72] which had capacitances of 10 pF/mm^2 and a series resistance of 17 MΩ. Several improvements followed by changing the contacts to metal, creating thinner dielectrics, and introducing higher permittivity materials to be used for the dielectric [73–75]. In 2012, Li et al. demonstrated the first inkjet-printed capacitors operating up to 10 MHz with capacitances of up to 13 pF/mm^2 [76,77], however no Q values have been reported. Inductors have also been demonstrated which operate up to 1 MHz with values up to 200 nH [78], but again, no Q values have been reported.

The objective of the proposed research is to demonstrate vertical integration of multi-layer inkjet-printed RF components such as lumped elements, antennas, and sensors which operate at frequencies ranging into the mm-Wave regime. The proposed research will show entirely new possibilities in the field of vertically-integrated inkjet-printed components which are more compact, operate at higher frequency, and can be printed on virtually any substrate. The research advances the complete integration of printed systems by replacing discrete lumped components with printed lumped elements, and incorporating multi-layer, high-gain antennas and sensors.

CHAPTER 4

VIPRE PROCESS CHARACTERIZATION

As stated in Chapter 2, the outcome of this dissertation will be the first demonstration of fully inkjet-printed multi-layer RF components, antennas, and systems which operate up to the mm-Wave regime, and are enabled by the creation of the VIPRE process. The creation of the VIPRE process includes the formulation and characterization of conductive and dielectric inks that are long term stable. These inks have been integrated into a layer-by-layer deposition process (VIPRE) which is characterized at RF frequencies to allow for accurate design and fabrication of vertically-integrated RF components up to the mm-Wave regime.

4.1 Dimatix Printing Platform

The VIPRE process is designed for the Dimatix DMP printing platform. The Dimatix printing platform is a very versatile piezo drop-on-demand platform which is compatible with small research grade printers as well as large industrial grade printers [79]. The specifications of the DMP-2831 printer used in this work are shown in Table 3.

Table 3. Dimatix Specifications

Nozzle Type	Piezo
Minimum Drop Volume	1 pL (20um diameter)
Nozzle Quantity	16
Scan Method	Raster
Ink Viscosity	8-12 cP
Ink Surface Tension	20 - 40 mN/m
Fiducial Camera Alignment	25 um
Stage Repeatability	25 um

4.2 Ink Formulation and Characterization

The first step in the creation of the VIPRE process is the formulation and characterization of the electronic inks which will be the building blocks of the process. The library of inks available in the process consists of:

1. High-Conductivity Silver Ink: A silver nanoparticle ink which exhibits conductivities near that of bulk metals

2. High-Conductivity Copper Catalyst Ink: A copper catalyst-based ink which produces high conductivity conductors on porous substrates at a fraction of the cost of nanoparticle-based inks

3. Thick-Layer Polymer Dielectric Ink: A high w/w% polymer ink which can produce thick insulator layers above 6 um/pass to create printed laminates and low-capacitance cross-overs

4. Thin-Layer Polymer Dielectric Ink: A low w/w% polymer ink which can produce thin insulating layers below 500 nm/pass for high capacitance structures

4.2.1 Methods

When formulating inks, the procedure in Fig. 22 is followed.

1. First, the material to be deposited is selected.

2. A solvent, or solvent system including co-solvents is chosen which dissolves/disperses the material to be deposited, has a high enough boiling point to prevent solvent drying at the printer nozzle, and can meet the surface tension and viscosity requirements of the printer (Table 3) after being loaded with the material.

3. Once the material is loaded into the solvent system, the viscosity and surface tension of the ink is adjusted with viscosity modifiers and surfactants.

4. The printability of the ink is then tested and the jetting waveform and temperature are optimized

5. The curing conditions are finally optimized to produce the desired film characteristics

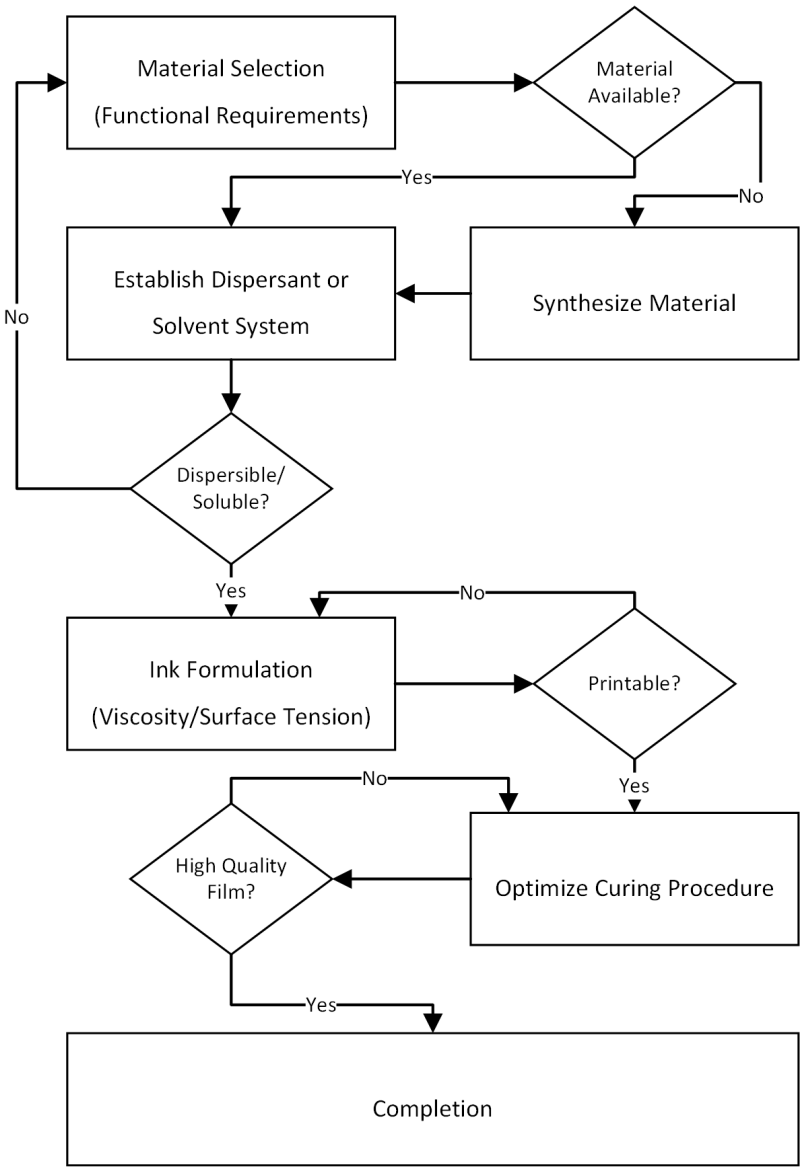

Figure 22. Process flow for formulating new electronic inks

4.2.1.1 Viscosity Measurement

To measure ink viscosity during viscosity tuning, the falling ball method is used to determine the static viscosity, and rotational shear stress analysis is used to determine the

dynamic viscosity.

For first-pass measurements, a Gilmont falling-ball viscometer (Gilmont GV-2200) is used which determines the viscosity by the fall time of a known-density sphere through a glass tube of nearly the same diameter which is filled with the fluid under test.

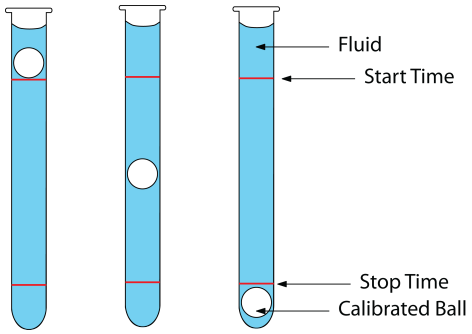

Figure 23. Falling ball viscometry

The relationship between the fall time of the sphere and the viscosity of the ink is shown in Eq. 14 where μ is the viscosity of the ink in centipoise (cP), K is the viscometer constant, ρ_b is the density of the ball in (g/ml), ρ_i is the density of the ink in (g/ml), and t is time in (min).

$$\mu = K(\rho_b - \rho_i)t \tag{14}$$

Once the static viscosity of the ink is determined to be within the range of the Dimatix print-head, a measurement of viscosity versus shear speed is performed using a Bohlin Gemini 2 rotational rheometer.

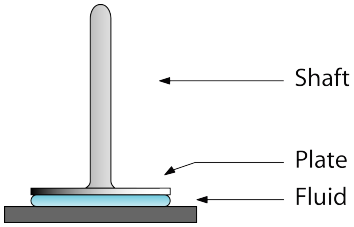

Figure 24. Rotational sheer rheometry

The rotational shear stress method places the fluid under test between two plates. As the top plate rotates at angular speed $\frac{d\gamma_{sheer}}{dt}$, the viscosity of the fluid presents a shear stress

τ. The viscosity η is related to the shear stress and shear speed by Eqs. 15 - 17 where T is the torque on the spindle, L is the length of the spindle, R_s is the spindle radius, R_c is the disk radius, ω is the rotational speed (rad/s), and x is the radial location where the shear rate is being calculated.

$$\eta = \frac{\tau}{\frac{d\gamma}{dt}} \tag{15}$$

$$\tau = \frac{T}{2\pi R_s^2 L} \tag{16}$$

$$\gamma_{sheer} = \frac{2\omega R_c^2 R_s^2}{x^2(R_c^2 - R_s^2)} \tag{17}$$

4.2.1.2 Surface Tension Measurement

To measure the surface tension of the ink, an Attension Theta Lite goniometer is utilized which calculates surface tension based on the pendant drop method. When a drop is suspended from a solid in air, the radius of curvature and drop shape is determined by the balance of gravitational and interfacial tension forces. The two most important parameters of the drop are the equatorial diameter D and the diameter d at distance D up from the bottom of the drop as shown in Fig. 25.

The interfacial tension can then be calculated using Eqs. 18 and 19 [80, 81] where $\Delta\rho$ is the difference between the density of the fluid and the density of air, g is the gravitational constant, and $S = d/D$. $B_i (i = 0, 1, 2, 3, 4)$ are empirical constants which can be found in [82].

$$\gamma_L = \frac{\Delta\rho g D^2}{H} \tag{18}$$

$$\frac{1}{H} = \frac{B_4}{S^a} + B_3 S^3 - B_2 S^2 + B_1 S - B_0 \tag{19}$$

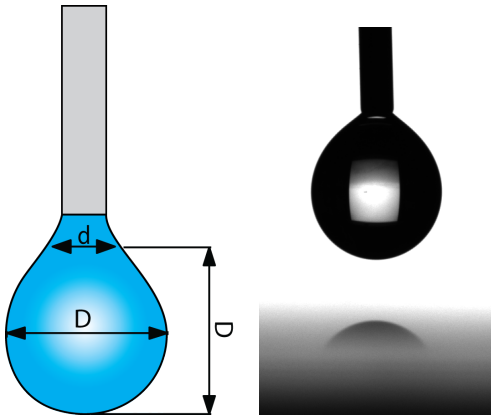

Figure 25. Pendant drop method for determining fluid surface tension (a) diagram, (b) physical pendant drop

4.2.2 Silver Nanoparticle Ink

Nanoparticle-based inks have recently shown promise in realizing high-conductivity conductors with low curing temperatures as discussed in Section 3.7.1. Except for the case of gold and silver, thermal treatments in air can result in significant oxidation of the metallic nanoparticles, particularly for relatively inexpensive non-noble metals, such as copper [83–85]. While inert or reducing gas atmospheres could be used to minimize or avoid such oxidation, processes that avoid such inert gas thermal treatments would be preferred for scalable manufacturing. The silver metallic-nanoparticle ink used in the VIPRE process is modified for the Dimatix platform from a commercial Suntronic U5603 ink. The final ink specifications are shown in Table 4.

Table 4. Silver Nanoparticle Ink Specifications

Material Loading	20 w/w% Silver Nanoparticles
Solvent	Ethanol & Ethylene Glycol 80 w/w%
Density	1.22 g/mL
Falling-Ball Viscosity	10.2 cP
Surface Tension	30 mN/m
Z (1/Oh)	1.88

4.2.2.1 Material

The ink is composed of 30 - 50 nm average diameter silver nanoparticles (Cabot Corp., Boston, MA) which are coated in a thin polymer ligand shell to prevent agglomeration when dispersed in a solution. Without a polymeric dispersant such as polyvinylpyrrolidone (PVP), the silver ions would strongly attract and form large clumps which would fall out of the dispersion and cause nozzle clogging and in-homogeneity throughout the ink [86, 87]. The nanoparticle dispersion is prepared commercially for safety reasons.

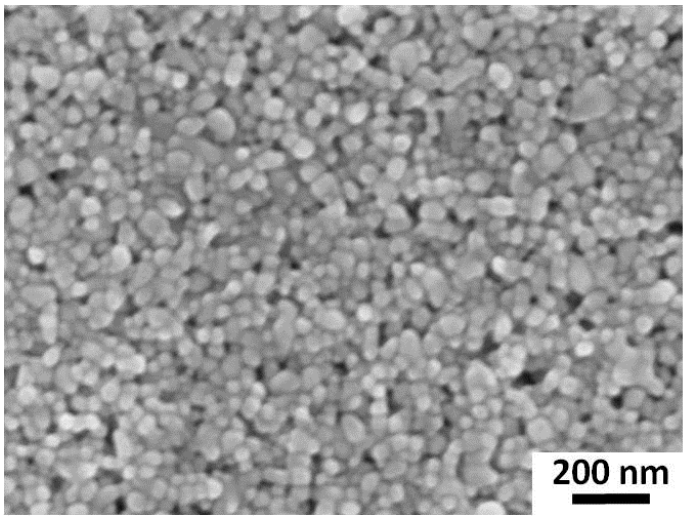

Figure 26. Silver nanoparticles as viewed under a scanning electron microscope

4.2.2.2 Solvent Selection

An alcohol-based solvent system is chosen that is a co-solvent mixture of ethanol and ethylene glycol. Ethanol is chosen as it disperses the PVP coated nanoparticles well. However, since ethanol has a low boiling point of 78.3°C, a low surface tension of 22 mN/m and a low viscosity of 1.6 cP, the co-solvent ethylene glycol which has a boiling point of 197.5°C, a surface tension of 48.4 mN/m and a viscosity of 16.1 cP is used to bring the ink into a printable range [88–90].

4.2.2.3 Viscosity and Surface Tension Measurements

The falling-ball measurements performed on the Gilmont-100 falling ball viscometer yield a static viscosity of 10.2 cP. The rheometric measurements, which are compared to the model ink supplied by the Dimatix Corporation yield a viscosity of approximately 12 cP over a shear speed of 1 to 40 rad/s as shown in Fig. 27. It can be noticed that the viscosity is very stable over sheer speed which is important for jetting stability over a variety of jetting speeds. The rheometric measurements also agree well with the falling-ball viscometer measurements.

Surface tension measurements of the silver nanoparticle ink are performed on the Attension Theta Lite goniometer which yield a surface tension of 30 mN/m at 25°C.

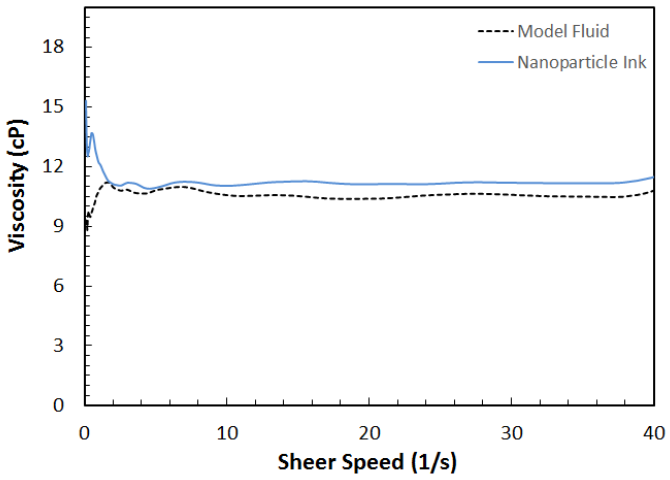

Figure 27. Silver nanoparticle ink rheometric measurement

4.2.2.4 Silver Nanoparticle Waveform and Nozzle Temperature

As the silver nanoparticle ink is well-matched with the viscosity and surface tension specifications of the Dimatix platform, the waveform shown in Fig. 40, which is used for the model Dimatix ink, jets the ink well at frequencies up to 15 kHz with the nozzle at room temperature.

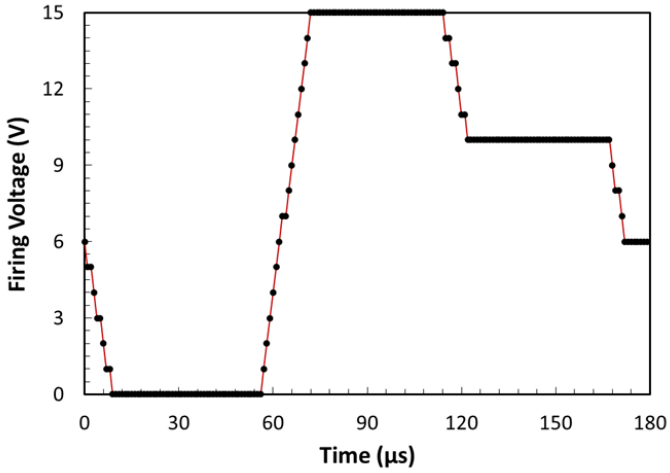

Figure 28. Waveform to jet silver nanoparticle ink

4.2.2.5 Printed Film Measurements and Optimization

After optimizing the ink and jetting conditions, tests are performed to determine the optimal drop spacing. The first in a series of tests is to determine the droplet diameter on the

substrate when the substrate has an optimal surface energy for the ink, which in the case of the inks used in the VIPRE process, is approximately 40 mN/m. An optical micrograph of the printed drops is shown in Fig. 29, and have an average diameter of 28 um.

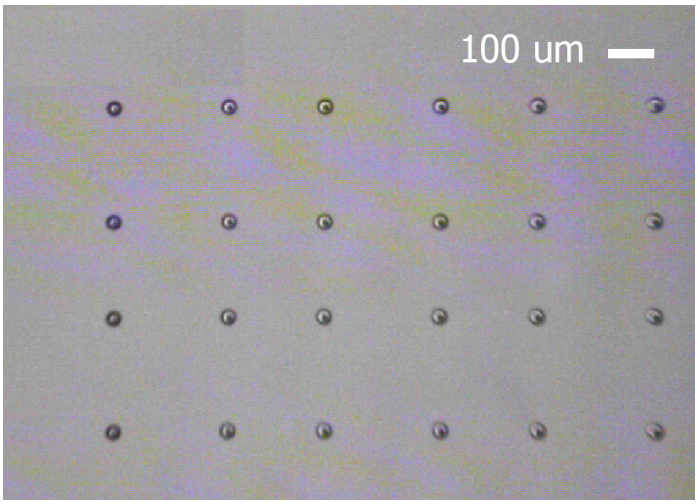

Figure 29. Silver drops on a 40 mN/m surface energy smooth polymer substrate

Drop spacing is then optimized by printing a series of lines with drop spacing ranging from 10 to 50 um. Optical micrographs of the printed lines are shown in Fig. 30. At 10 um drop spacing, the surface tension of the ink is not strong enough to hold the shape of the line, and periodic bulging occurs. Similar effects can be seen at 15 um spacing, but in a less pronounced manner. As the drop spacing increases to 20 um, the line begins to thin and stable line formation occurs. The line continues to thin until 40 um spacing is reached, at which point scalloping of the line occurs. Once 50 um drop spacing is reached, discrete drop formation occurs as the drop spacing is too wide for the transient drop expansion upon substrate contact to reach the previously printed droplets.

The lines are subsequently dried at 100°C and the line topology is measured using a KLA-Tencore D-100 stylus profilometer. The printed line width and thickness are presented in Fig. 31. It can be seen that at 10 um drop spacing, the line width is approximately 66 um with a thickness of 380 nm. As drop spacing increases, line width decreases as along with line thickness. In the stable region of 20 - 30 um spacing, the minimum line width

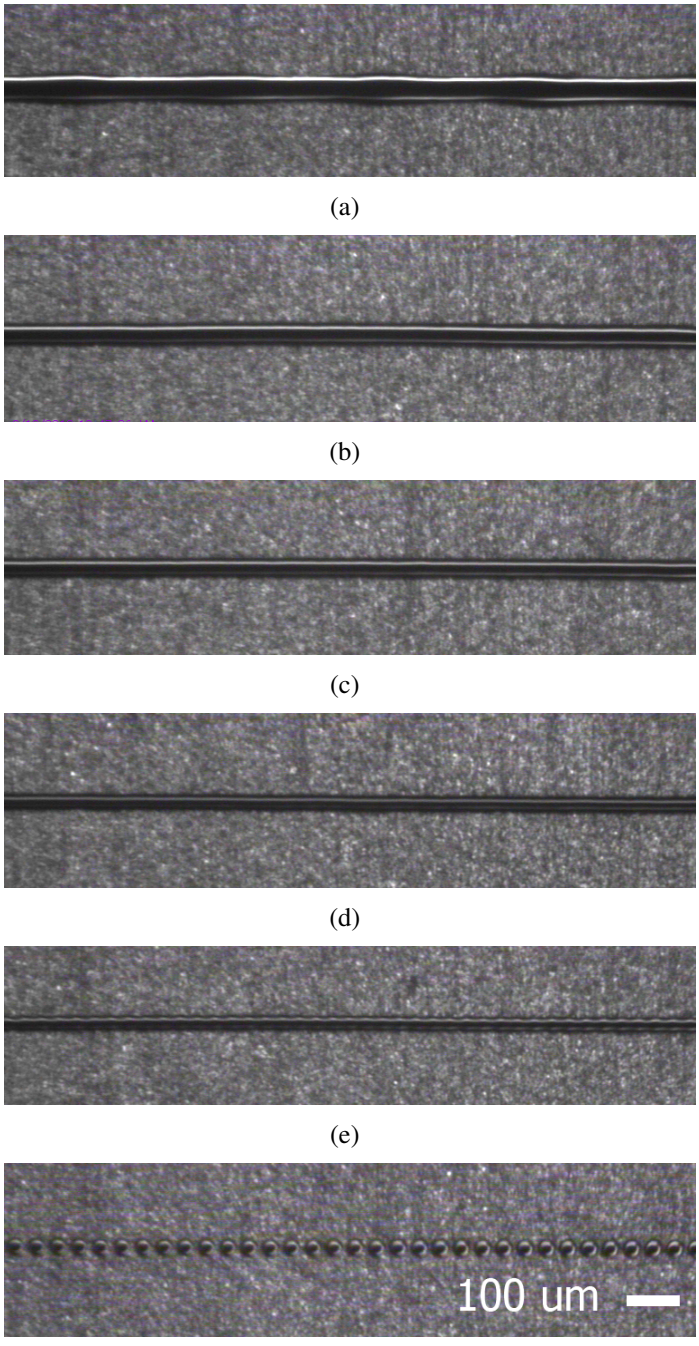

Figure 30. Silver nanoparticle ink drop space test with - (a) 10 um spacing, (b) 15 um spacing, (c) 20 um spacing, (d) 30 um spacing, (e) 40 um spacing, and (f) 50 um spacing

obtainable is 40 um with a thickness of 300 nm. The line width and thickness continue to decrease until the line breaks off to individual drops and the thickness increases as the ink becomes contained and does not spread to form continuous beads. A single drop has a

dried diameter of 30 um and thickness of 250 nm.

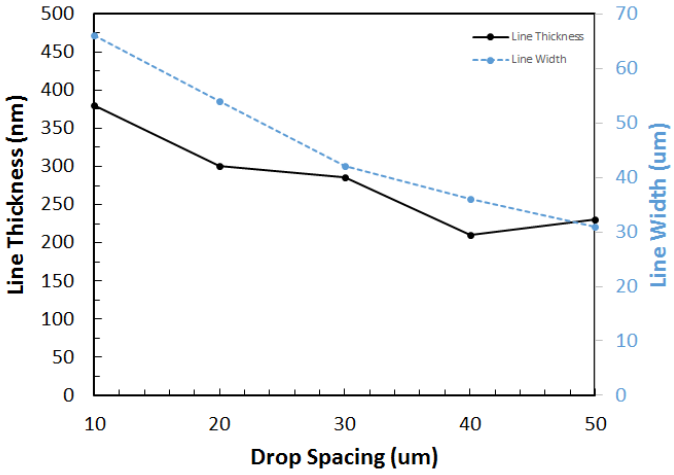

Figure 31. Line morphology of printed silver nanoparticle lines with varying drop spacing

While the characteristics of individual lines are important, the characteristics of features are more important for designers using the VIPRE process. With that in consideration, feature size, minimum spacing, and feature thickness for larger scale objects are measured. Feature size is obtained from the minimum line width which is approximately 40 um. Minimum spacing, which can be shown in Fig. 32, is also approximately 40 um. However, this occurs when 100 um spacing is specified which is due to ink spreading. When 50 um spacing is specified as in Fig. 32(a), the space is nearly closed due to bleed-over from to the transient expansion of droplets when they impact the substrate. A good rule of thumb with the dimatix platform is to expect a space which is smaller by the specified drop spacing on each side (i.e. $space = (GivenS\,pacing) - 2(DropS\,pacing)$)

The layer thicknesses of larger printed features using 20 um spacing are shown in Fig. 33. The results show that when larger features than a single line are printed, the thickness of the layer are slightly thicker than that of an individual line due to the fact that more ink is deposited in the same area. It can be seen that the layer thickness of one layer is approximately 450 nm. Successive printer passes linearly increase the layer thickness by 450 - 500 nm which allows a designer to choose thicknesses by specifying printer passes.

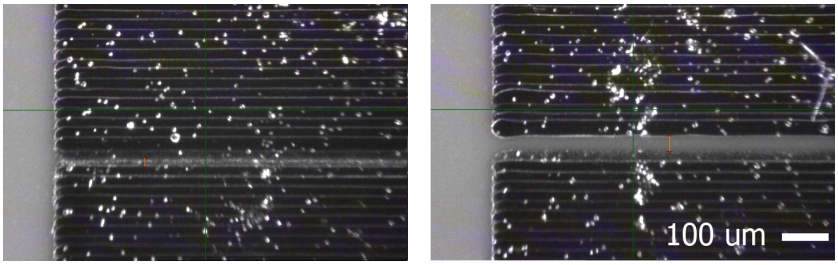

(a) (b)

Figure 32. Minimum space - (a) specified 50 um spacing, (b) specified 100 um spacing

An SEM cross section of the silver nanoparticle features is shown in Fig. 34.

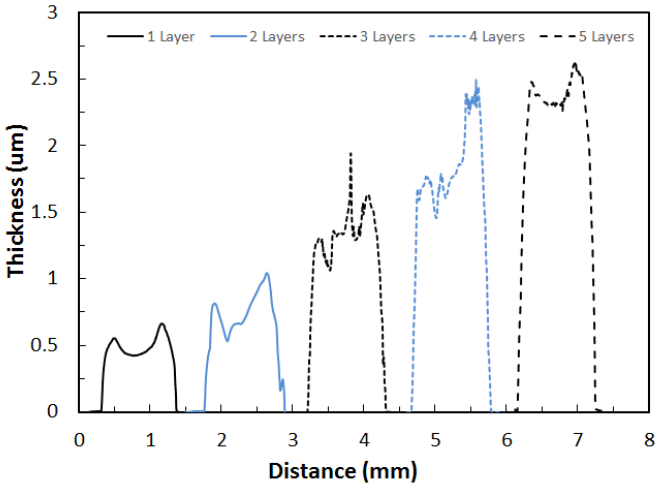

Figure 33. Feature thickness when multiple printer passes are performed at 20 um spacing

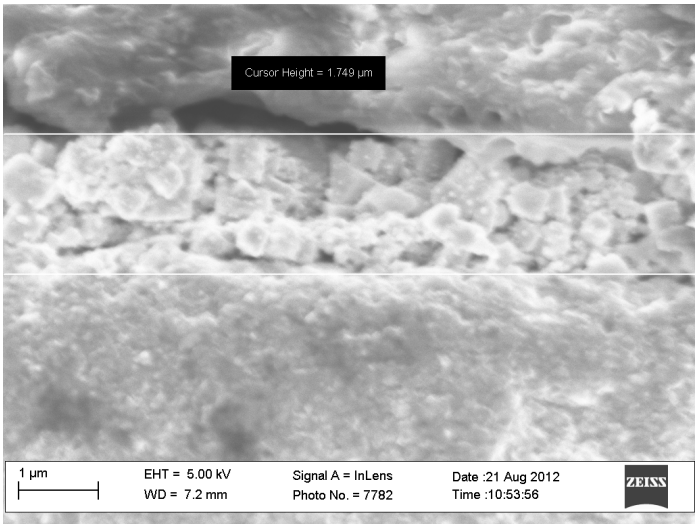

Figure 34. SEM cross section of three printed layers of silver nanoparticle ink at 20 um spacing

X-ray diffraction (XRD) and energy-dispersive x-ray (EDX) analyses of the films are shown in Fig. 35. The films are comprised predominantly of metallic silver with no appreciable detectable oxide formation (i.e., the thermal treatment of the silver nanoparticle films in air did not result in appreciable detectable silver oxide formation). Scherrer analyses of the XRD patterns yield average crystallite sizes of 21 nm for the Ag films.

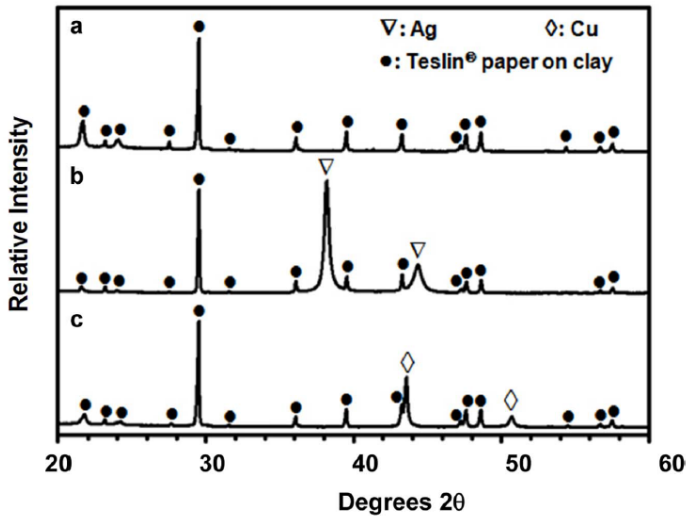

(a)

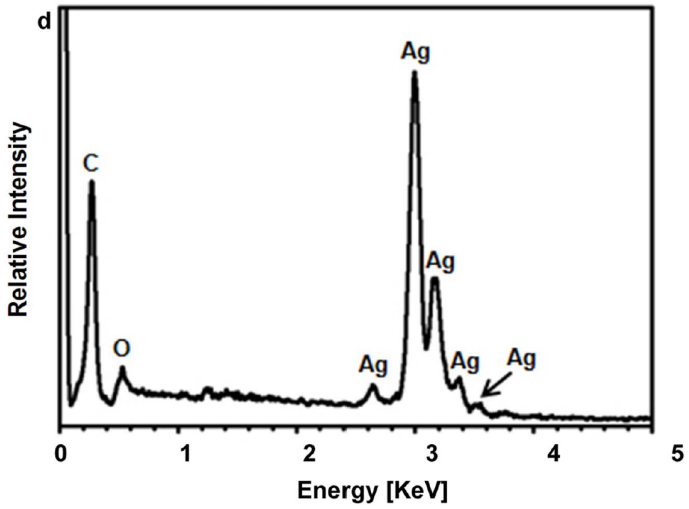

(b)

Figure 35. (a) XRD analysis of the silver films on Teslin paper, and (b) EDX analysis of silver films on Teslin paper

4.2.2.6 Electrical Characteristics

When printed, the silver nanoparticle features are in a non-conductive state as they are coated in the polymer ligand shell which was used to keep them dispersed within the solvent. To form conductive features, they must be sintered together. In this work, a full parametric characterization of the conductivity of silver nanoparticle features is conducted with heat and laser sintering for the first time [24].

First, test features are printed on a glass host substrate with 1 - 5 printed layers, and heated in a Thermo Scientific oven for one hour with temperatures varying from 100 - 200°C. The test structures are then measured using the 4-point probe method to extract the sheet resistance. Fig. 36 shows the sheet resistance versus temperature and number of printed layers. The sheet resistance varies from as high as 10Ω/□ to as low as 0.03Ω/□ which speaks to the importance of processing conditions to obtain high conductivity conductors.

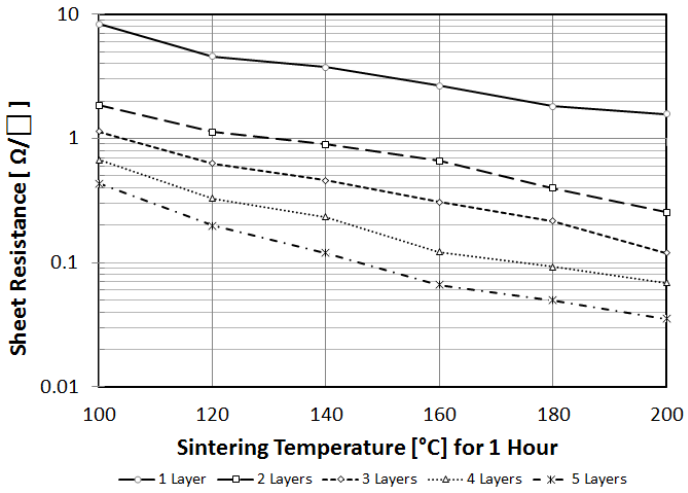

Figure 36. Sheet resistance of silver nanoparticle filmes under thermal curing

Fig. 37 shows the time dependent sheet resistance of silver nanoparticle features during heat sintering. It can be seen that the sheet resistance decreases until one hour is reached, at which point the sheet resistance remains constant. If sintering is continued for longer periods of time, heat-induced oxidation would eventually cause the sheet resistance to increase

again.

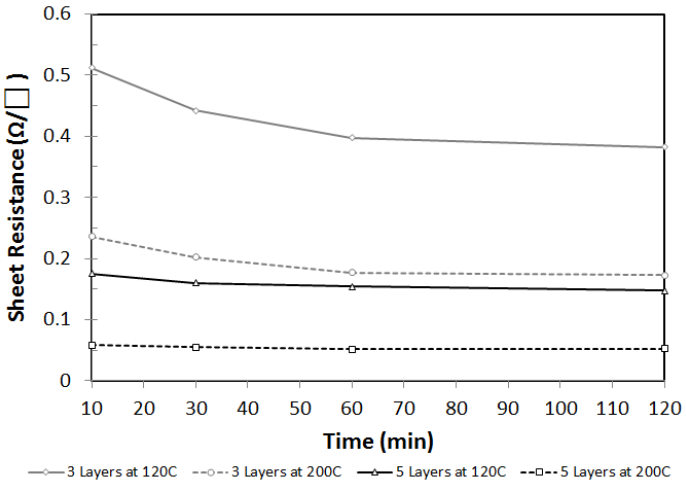

Figure 37. Sheet resistance of silver nanoparticle films over time under thermal curing

To reduce sintering time and cost, laser sintering is performed in which a 75 W CO_2, 10 um wavelength laser from Universal Laser Systems is raster scanned over the surface of the test features. The raster scanning of a 1 cm^2 area takes less than one second as opposed to the one hour of oven curing which is required to reach steady state in heat sintering. The results in Fig. 38 show that by using full laser power, sheet resistances for the printed nanoparticle films equivalent to sintering for one hour at 200°C are obtained.

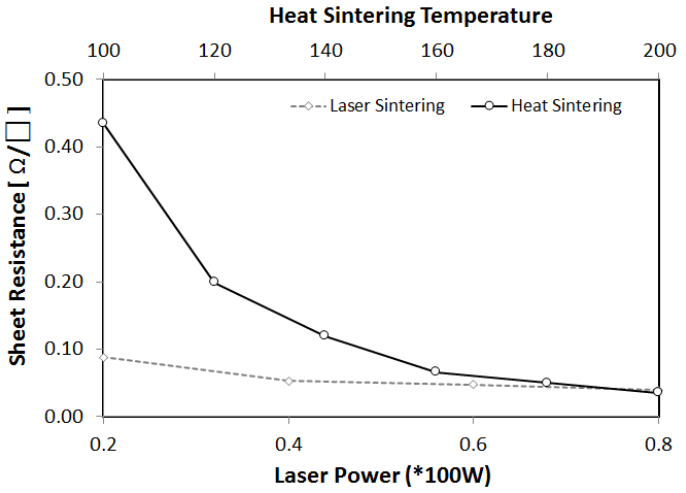

Figure 38. Sheet resistance of silver nanoparticle filmes under thermal versus laser curing

Utilizing the cross sectional thickness *t* of the printed test structures used for both laser

and heat sintering, and the sheet resistance R_s, the conductivity σ of the ink is extracted using Eq. 20. The results are shown in Table 5.

$$\sigma = \frac{1}{R_s t} \tag{20}$$

Table 5. Measured conductivity of the printed silver nanoparticle films

Layers	Temperature (C)	Conductivity (S/m)
1	100	4.5E+4
5	100	1.0E+6
1	200	2.8E+5
5	200	1.3E+7
5	Laser	1.3E+7

4.2.3 Copper Catalyst Ink

As discussed in Section 4.2.2, metals such as copper cannot be deposited using nanoparticles due to oxidation during sintering. However, copper is preferable in many applications as it is much cheaper than silver and has a higher bulk conductivity. This section presents a new method to deposit copper in which a palladium chloride copper catalyst is printed onto the substrate which is subsequently placed in a copper plating bath to deposit copper. This process allows for depositing films equivalent in conductivity to those deposited using silver nanoparticles at a 15x cost reduction. The solution-based patterning and electroless copper deposition process avoids nozzle-clogging problems and costs associated with noble metal particle-based inks. This process yields compact conductive copper layers without appreciable oxidation and without the need for an elevated temperature, post-deposition thermal treatment commonly required for noble metal particle-based ink processes [91]. The final ink specifications are shown in Table 6.

Table 6. Copper Catalyst Ink Specifications

Material Loading	0.125 w/w% Palladium Chloride
Solvent	Ethanol:Glycerine 50:50w/w%
Density	1.0 g/mL
Falling-Ball Viscosity	12.1 cP
Surface Tension	27.4 mN/m
Z (1/Oh)	1.37

4.2.3.1 Material

The homogeneous palladium(II) chloride catalyst solution is prepared as follows. A 10 mg batch of $PdCl_2$ (99.999% purity, Alfa Aesar, Ward Hill, MA) was added to 40 mL of anhydrous ethanol and stirred at 30 rpm for 2 h at room temperature. After removal of undissolved $PdCl_2$ by centrifugation (9000 rpm, 2 min), the supernatant was isolated and passed through a 0.2 m filter (Fujifilm Dimatix, Inc., Santa Clara, CA, USA).

The copper-bearing bath for electroless deposition was comprised of an aqueous solution of 0.19 M cupric sulfate (anhydrous $CuSO_4$, Mallinckrodt Baker, Phillipsburg, NJ,USA) with 0.67 M sodium potassium tartrate tetrahydrate ($C_4H_4KNaO_6¢4H_2O$, Alfa Aesar). After adjusting the pH of this solution to 12.5 using an aqueous NaOH solution, formaldehyde (37% in water, Alfa Aesar) was added at a concentration of 220 mM. This solution was then passed through a 0.2 μm filter to remove contaminant particles.

4.2.3.2 Solvent Selection

As the palladium(II) chloride catalyst is required to be prepared in ethanol (η = 1.6 cP, γ_L = 22mN/m, *B.P.* = 78.3°C), a co-solvent is required to bring the ink into a printable range as well as increase the boiling point of the ink. Glycerol (η = 934 cP, γ_L = 76.2mN/m, *B.P.* = 290°C) is a common viscosity and surface tension modifier which is readily miscible in ethanol. It is found that a 50:50 w/w% of ethanol to glycerol brings the ink into a printable range [88–90].

4.2.3.3 Viscosity and Surface Tension Measurements

The falling-ball measurements performed on the Gilmont-100 falling ball viscometer yield a static viscosity of 12.1 cP. The rheometric measurements shown in Fig. 39, which are compared to the model ink supplied by the Dimatix Corporation yield a viscosity of approximately 12 cP at lower shear speeds which decreases to 8 cP at higher speeds which is still within the printable viscosity range.

Surface tension measurements of the copper catalyst ink are performed on the Attension Theta Lite goniometer which yield a surface tension of 27.4 mN/m at 25°C.

4.2.3.4 Copper Catalyst Waveform and Nozzle Temperature

As the copper catalyst ink is well-matched with the specifications of the Dimatix piezo inkjet nozzle, the optimal waveform shown in Fig. 40 which is used for the model Dimatix ink jets the ink well at frequencies up to 10 kHz. The nozzle temperature is increased to 35°C to optimize the jet-ability of the ink.

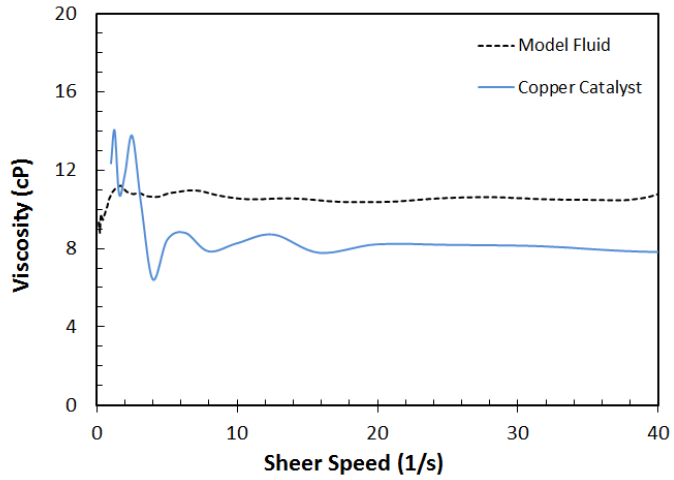

Figure 39. Copper catalyst ink rheometric measurement

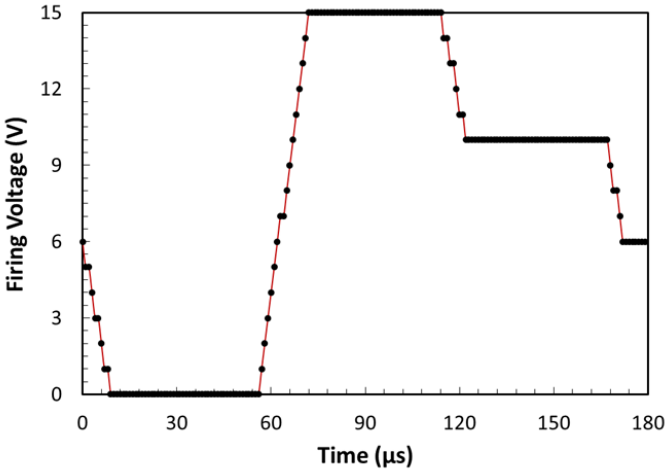

Figure 40. Waveform to jet copper catalyst ink

4.2.3.5 Printed Film Measurements and Optimization

As all inks formulated for the VIPRE process have the same surface tension and viscosity as the silver nanoparticle ink, the optimal jetting conditions and drop spacing will be the same. Therefore, to determine film quality of the copper catalyst, a single layer of test features is printed onto a porous Teslin substrate at 20 um spacing. The substrates are then placed in the electroless deposition bath for varying amounts of time from 10 to 50 minutes to determine the copper deposition rate and film morphology versus time.

As the catalyst ink is required to be deposited on surfaces which can bind to the catalyst (such as Teslin paper), surface profilometry is not able to determine the cross sectional profiles of the films due to the surface roughness of the deposition surface. Therefore, polished cross-sections of copper and silver films on Teslin paper were created by encapsulating the specimens within an epoxy resin, followed by grinding and polishing with a series of SiC-bearing polishing papers and then diamond pastes to a final surface finish of 0.25 um. Scanning electron microscopy was conducted with a field emission scanning electron microscope (Leo 1530 FEG SEM, Carl Zeiss SMT Ltd., Cambridge, UK) equipped with an energy dispersive x-ray spectrometer (INCA EDS, Oxford Instruments, Bucks, UK). X-ray diffraction analyses(X-Pert Pro Alpha 1 diffractometer, PANalytical, Almelo, The Netherlands) were conducted with Cu K radiation using an incident beam Johannsen monochromator and an Xcelerator linear detector.

Representative secondary electron (SE) images of topdown and cross-sectional views of copper catalyst and silver nanoparticle (for comparison) films are shown in Fig. 41. The topdown and cross sectional views of the copper catalyst-deposited films show that the grain size is much smaller than that of a silver nanoparticle-deposited film, and that the films are much more uniform than a nanoparticle-deposited film. This is due to the fact that the film is grown and not deposited as discrete nanoparticles. At 10 min, the Cu film is 0.61 um thick, and at 50 min, the Cu films are approximately 3.87 um thick. This yields an average growth rate of 60 - 75 nm/min of deposition.

X-ray diffraction (XRD) and energy-dispersive x-ray (EDX) analyses of such films are shown in Fig. 42. The films are comprised predominantly of metallic copper with no appreciable detectable oxide formation. Scherrer analyses of the XRD patterns yield average crystallite sizes of 33 nm for the Cu films.

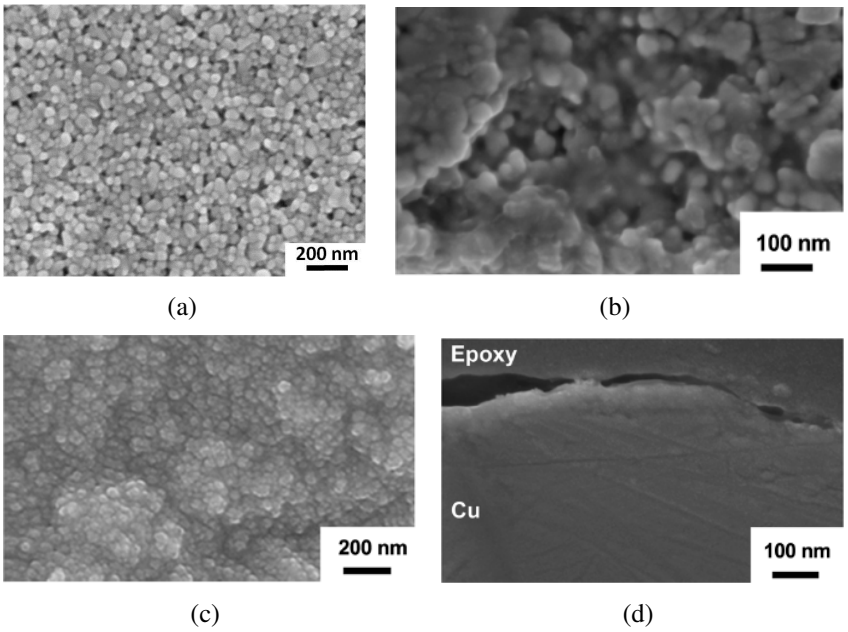

Figure 41. (a) Top view of silver nanoparticle film, (b) Cross sectional view of silver film, (c) Top view of copper film, and (d) Cross sectional view of copper film

4.2.3.6 Electrical Characteristics

Unlike nanoparticle based inks which require sintering to make the film conductive, the catalyst plated films require no treatment after plating. To determine the electrical characteristics of the films, printed copper catalyst test films are measured using the 4-point probe method to determine the sheet resistance. It can be seen in Fig. 43 that with increased deposition time in the copper plating bath, the sheet resistance of the copper film decreases from 7.3 Ω/□ at 10 minutes to 0.1 Ω/□ at 50 min, which is comparable to 4 layers of printed silver cured at 200°C. Maximum conductivities of 4E+6 S/m are obtained which is approximately half that of the silver nanoparticle ink, however, this is at much lower cost, and with no post-print heat or laser curing.

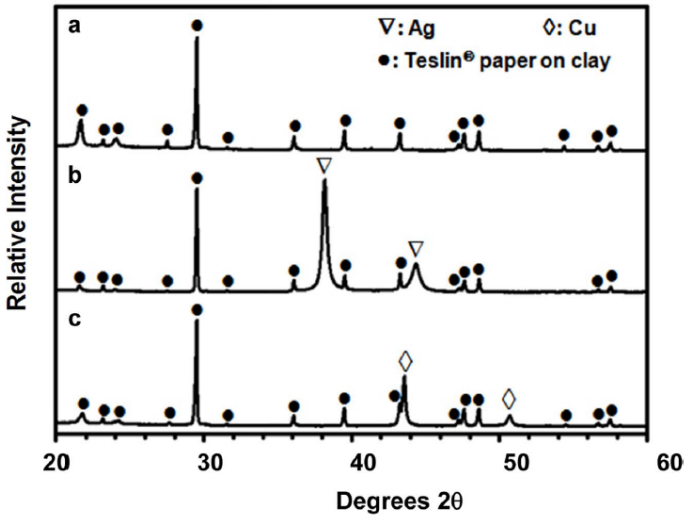

(a)

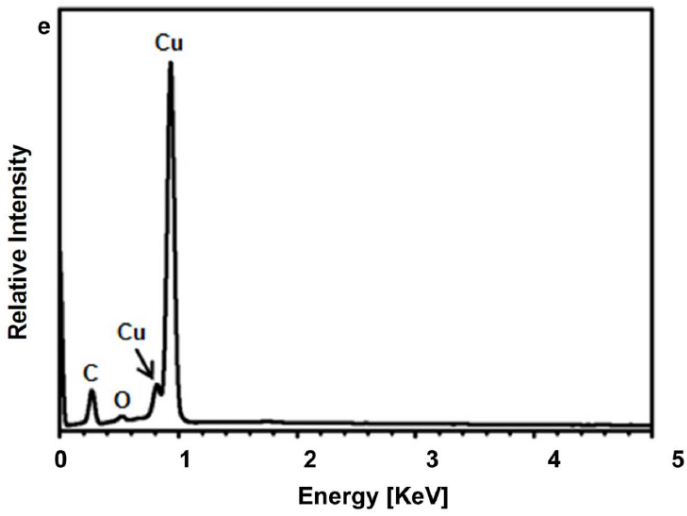

(b)

Figure 42. (a) XRD analysis of the copper films on Teslin paper, and (b) EDX analysis of copper films on Teslin paper

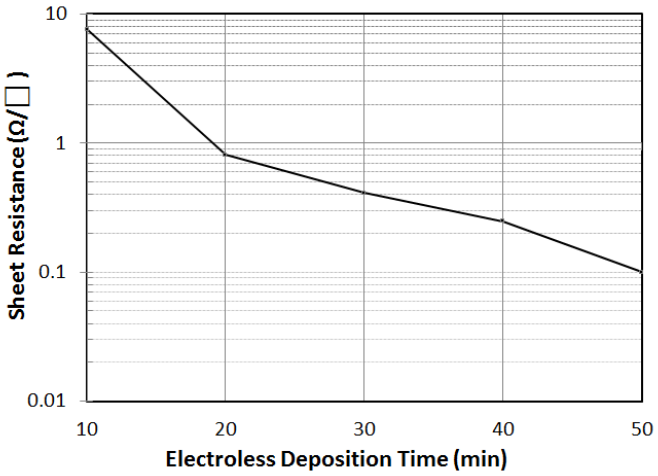

Figure 43. Copper catalyst sheet resistance versus plating time

4.2.4 Thick-Layer Dielectric Ink

To create multi-layer RF structures, dielectric inks are required to provide insulation between successive metal layers. When designing RF structures, the ability to design with thick dielectric layers is important for decreasing inter-layer interconnect capacitance and allowing for the design of wideband filters and antennas. Prior art has shown inkjet-printed dielectrics which can reach maximum thicknesses of approximately 4 um which is far too thin for typical mm-Wave and RF designs [75, 78, 92]. To address this issue, a thick-film dielectric, which can print dielectric layers with thicknesses in excess of 6 um per pass, is created. To produce thick layers, an SU-8 polymer which can be heavily loaded into a solvent while keeping the net viscosity low is chosen. This allows large amounts of material to be deposited at once.

Table 7. Thick Layer Dielectric Ink Specifications

Material Loading	35 w/w% SU-8 Polymer
Cross-Linker	5 w/w% Triaryl Salt (SbF_6)
Solvent	Cyclopentanone 60w/w%
Density	1.14 g/mL
Falling-Ball Viscosity	13 cP
Surface Tension	30.5 mN/m
Post-Curing Surface Energy	30 mN/m
Z (1/Oh)	1.43

4.2.4.1 Material

The SU-8 polymer, which is commonly used in photo-resist applications due to its ability to be cross-linked with near-UV (350-400nm) light when Triaryl salt (SbF_6) is added, is a very short-chain polymer with a low molecular weight (mW) (mW = 1397) [93]. Since SU-8 has such a low molecular weight, a high percentage by weight can be loaded into a solvent which can dissolve SU-8 while keeping the solution viscosity low.

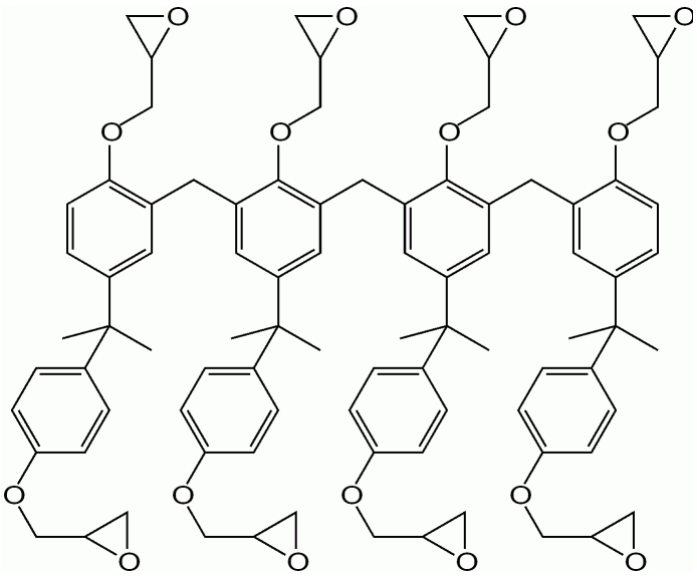

Figure 44. Polymer chain structure of SU-8

4.2.4.2 Solvent Selection

SU-8 is easily dissolved in Cyclopentanone (η = 1.29 cP, γ_L = 33.4mN/m, *B.P.* = 130.6°C), which does not require a co-solvent to bring the ink into a printable range once loaded with SU-8 polymer to increase the viscosity [88–90]. However, if nozzle drying becomes an issue, Etyl Lactate (η = 2.4 cP, γ_L = 29.2 mN/m, *B.P.* = 155°C) [94] can be used to increase the *B.P.* without changing the viscosity or surface tension [95]. In the following section, parametric analysis of SU-8 loading into the cyclopentanone solvent is performed.

4.2.4.3 Viscosity and Surface Tension Measurements

By loading more polymer into an ink by weight, thicker layers can be obtained as long of the viscosity of the ink can be kept withing the printable range. To determine the maximum polymer loading within the solvent which keeps the viscosity of the ink within the printable range, a parametric sweep of the polymer loading by weight is performed. Falling-ball measurements show the viscosity of the SU-8 ink to be below 13 cP, the high end of the printable range, at 25°C until 35 w/w% of the polymer is loaded into cyclopentanone as shown in Fig. 45. After 35 w/w% is reached, the solvent solution begins to saturate and the viscosity rapidly increases. To get the maximum thickness, 35 w/w% is chosen for the

thick layer dielectric ink. The rheometric analysis is displayed in Fig. 46.

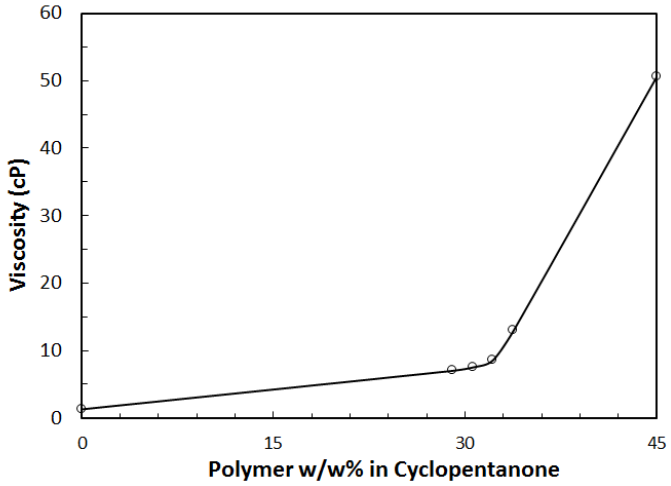

Figure 45. Falling ball viscosity of various w/w% SU8 in Cyclopentanone

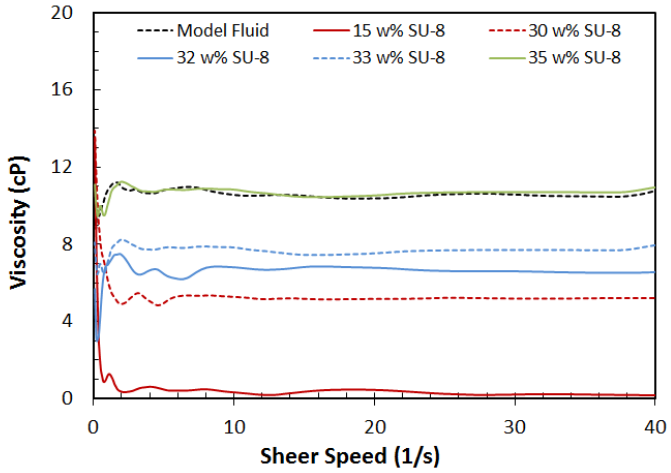

Figure 46. Rheometric analysis of various w/w% concentrations of SU8 in Cyclopentanone

Surface tension measurements of the thick layer dielectric ink are performed on the Attension Theta Lite goniometer which yield a surface tension of 30.5 mN/m at 25°C.

4.2.4.4 Thick Film Dielectric Waveform and Nozzle Temperature

As the thick film dielectric ink is well-matched with the specifications of the Dimatix piezo inkjet nozzle, the optimal waveform shown in Fig. 40 which is used for the model Dimatix ink jets the ink well at frequencies up to 10 kHz. The nozzle temperature is increased to 30°C to optimize the jet-ability of the ink.

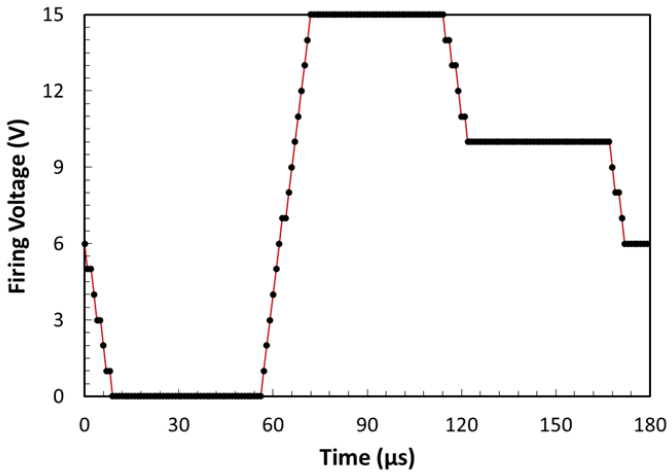

Figure 47. Waveform to jet thick-layer dielectric ink

4.2.4.5 Printed Film Measurements and Optimization

As the dielectric layers will act as insulating layers between conductors, the key physical film characteristics that are important are the film thickness, film surface roughness, and cured film surface energy which is important for the deposition of successive layers.

The first characterization performed on the thick film dielectric ink is an analysis on the printed film thickness versus drop spacing. Square films are printed on a glass substrate to allow for surface profilometetry measurements of films with drop spacing varying from 15 - 30 um. Fig. 48 shows the surface profile measurements for the deposited films.

For 30 um drop spacing, very uniform films are obtained which have an average thickness of 2 um and a negligible coffee ring effect due to the high material content loading in the solvent. 25 um and 20 um drop spacing produce high quality uniform films with thicknesses of 3 and 5.5 um respectively. At 15 um drop spacing, a film of approximately 11 um thickness is obtained, however, at the cost of a higher coffee ring which causes a +/- 1 um (9%) variation of the film thickness across the film profile, which is less than most typical microwave laminates.

Since 20 um spacing produces thick layers without a major coffee ring effect, 20 um is chosen as the optimal drop spacing. Following the determination of optimal drop spacing,

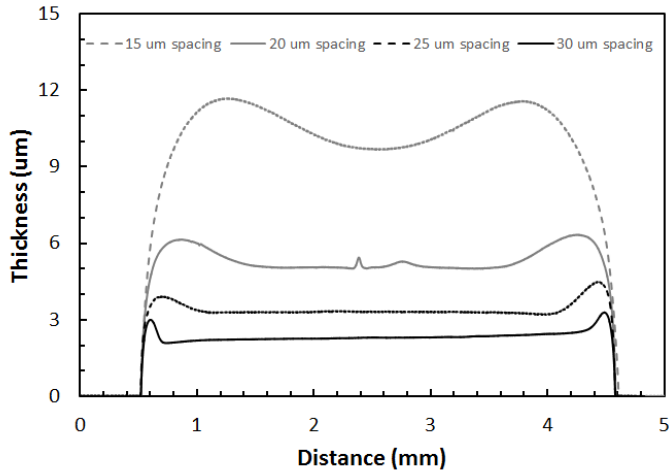

Figure 48. Thickness of printed thick film dielectric versus drop spacing

the layer thickness versus number of printed layers is analyzed. Fig. 49 shows printed films with one, two, five, and seven printed layers. For one and two printed layers, the films are relatively smooth with a linear addition of 6 um per layer. However, as the films get thicker, there is a noticeable coffee ring effect which decreases the uniformity of the printed film.

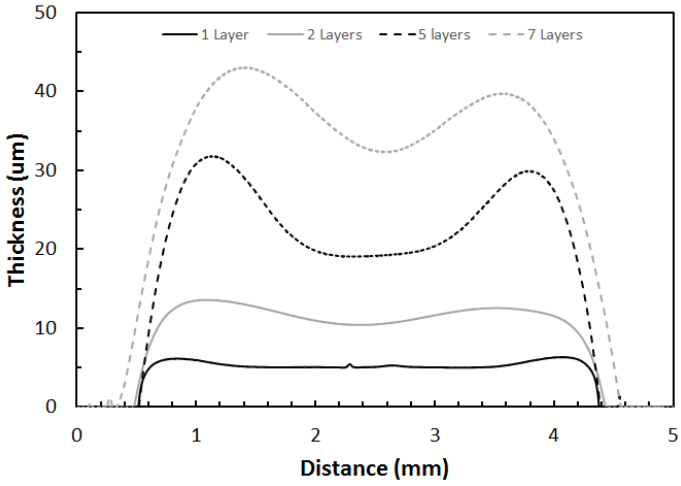

Figure 49. Thickness of printed thick film dielectric versus number of printed layers

To correct this, a reflow technique is used in which the printed layers are heated past the glass transition temperature of the SU-8, which causes the material to melt and restore its shape to a lower energy state, which would be a dome - similar to a droplet of liquid. However, if the reflow process is stopped before the material reaches the final dome shape,

a flat film can be obtained. Fig. 50 shows the result of reflowing for 1 minute at 150°C. The reflow process smooths the top of the film leaving it flat. This technique allows for the formation of extremely thick printed films.

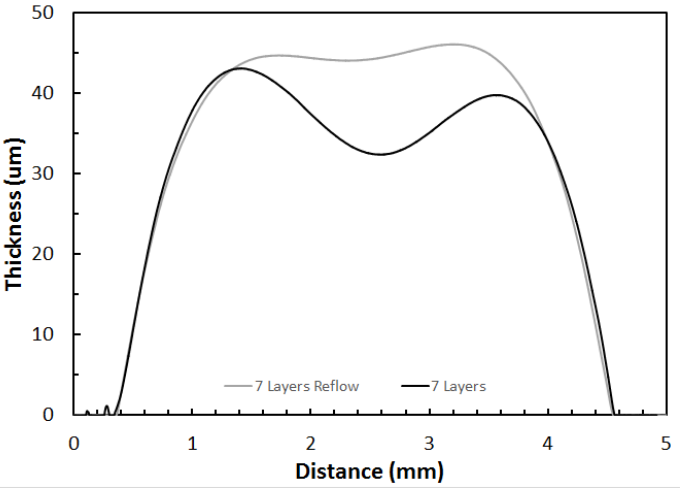

Figure 50. Reflow process to smooth thick film dielectrics with a coffee ring

Once the film is printed and reflowed with the proper morphology, the film needs to be cross-linked to polymerize and solidify the film. The cross linking procedure consists of a pre-exposure bake at 90°C for 5 minutes to drive off any remaining solvent, a 365 nm UV exposure at a dosage of 200 mJ/cm^2 to release the photoacid, and a post-exposure bake at 120°C for 5 minutes to enable complete cross-linking of the film [96].

Following the cross-linking of the film, the free surface energy is measured using the contact angle method. It is important to know the surface energy for the printing of successive material layers. Two solvents of known surface energy, water (H_2O), and dimethylsulfoxide (DMSO) are dropped onto the substrate and their contact angles are measured using an Attension Theta Lite goniometer. Fig. 51 shows the measured contact angles of both water and DMSO on the post-cross-linked film. Water demonstrates a contact angle of 85°, and DMOS demonstrates a contact angle of 58°. This yields a surface tension of 29.5 mN/m.

As discussed in Section 3.5.1, it is important to have a free surface energy of 10 - 20

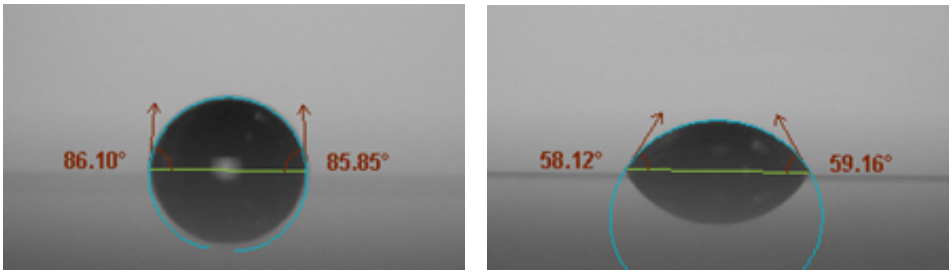

(a) (b)

Figure 51. Contact measurements on post-cross-linked SU-8 with (a) Water, and (b) DMSO

mN/m above that of the ink to allow for proper wetting. To increase the surface of the SU-8, a Jetlight 42 UV Ozone cleaner is utilized which etches the surface of the SU-8 and creates free bonds which increase the surface energy. Plots of the contact angle, and free surface energy of the SU-8 versus exposure time are shown in Fig. 52.

4.2.4.6 Electrical Characteristics

To characterize the electrical permittivity of the printed thick film dielectric, the microstrip T-resonator method is used [97–99]. The microstrip T-Resonator is a length of transmission line with an open circuit stub, as shown in Fig. 53. The resonator has a null in the insertion loss when the reflected wave from the stub is 180° out of phase or when the length of the open circuit stub is approximately $\frac{\lambda}{4}$. The equation for resonance is shown in (21) where n is the resonance mode i.e. (n = 1, 3, 5, ...), c is the speed of light in free space, L is the length of the open circuit stub, L_0 is the correction factor for the fringing capacitance at the end of the stub, and ϵ_{eff} is the effective permittivity of the microstrip line [98]. This effective permittivity can then be related to relative permittivity using equations in [100].

$$f_{r,n} = \frac{nc}{4(L + L_0)\sqrt{\epsilon_{eff}}} \tag{21}$$

The quality factor (Q) of each resonance can then be used to extract the loss tangent of the paper substrate. The loaded Q-factor which is the Q without removing the load due to connected measurement equipment is calculated in (22), and then is converted to the

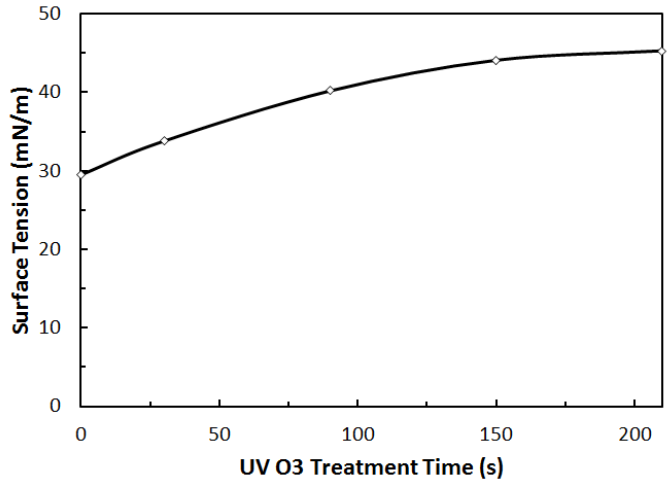

(a)

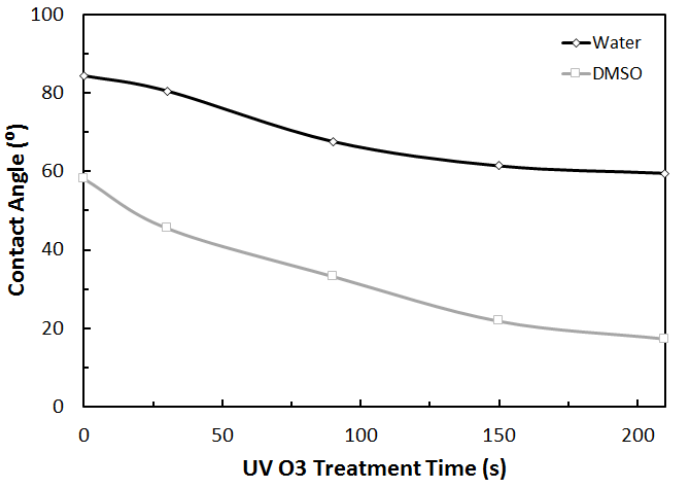

(b)

Figure 52. Surface characterization of SU-8 films versus UVO exposure: (a) Surface energy, and (b) Contact angle

unloaded Q-factor using equation (23) which de-embeds the loading caused by the measurement equipment [98]. L_a in Eq. 23 represents the insertion loss at the corresponding resonance n.

$$Q_{l,n} = \frac{f_{r,n}}{BW_{3dB,n}} \tag{22}$$

$$Q_{ul,n} = \frac{Q_{l,n}}{\sqrt{1 - 2\exp\frac{La}{10}}} \tag{23}$$

The unloaded Q-factor is then converted into loss in [dB/m] using (24). The total loss $\alpha_{tot,n}$ is composed of conductor loss $\alpha_{c,n}$, dielectric loss $\alpha_{d,n}$, and radiation loss $\alpha_{r,n}$ [97]. Conductor losses are subtracted through Agilent's Line-Calc software using the conductivity corresponding to two printed layers and heat sintering at 200°C; radiation losses are assumed negligible at these low frequencies relative to substrate thickness.

$$\alpha_{tot,n} = \alpha_{c,n} + \alpha_{d,n} + \alpha_{r,n} = \frac{8.686\pi f_{r,n}\sqrt{\epsilon_{eff}}}{cQ_{ul,n}} \tag{24}$$

The remaining dielectric loss can be related to loss tangent through (25) where λ_0 is the free space wavelength [97].

$$tan\delta = \frac{\alpha_{d,n}\lambda_0\sqrt{\epsilon_{eff,n}}(\epsilon_{r,n} - 1)}{8.686\pi\epsilon_{r,n}(\epsilon eff, n + 1)} \tag{25}$$

The T-resonator is fabricated by first printing and heat curing a ground plane using the silver nanoparticle ink on a glass slide. Subsequently, a 100 um thick SU-8 dielectric layer is printed and cured. The surface tension of the SU-8 dielectric is increased to 40 mN/m using a 90 second UVO exposure. The T-resonator is then printed on top using silver nanoparticle ink and utilizes a co-planar waveguide (CPW) to microstrip feed which allows for probing of the T-resonator with 500 um pitch GSG probes. The fabricated T-resonator is shown in Fig. 53.

The insertion loss of the T-resonator is then measured and the CPW-Microstrip transition is de-embedded using a printed TRL calibration kit. The measured insertion loss is shown in Fig. 54, and resonances can be seen at odd harmonics of 2.2 GHz.

By extracting the frequencies of each resonance, the relative permittivity (ϵ_r) is calculated and shown in Fig. 55. At low frequency, the permittivity of the SU-8 film is

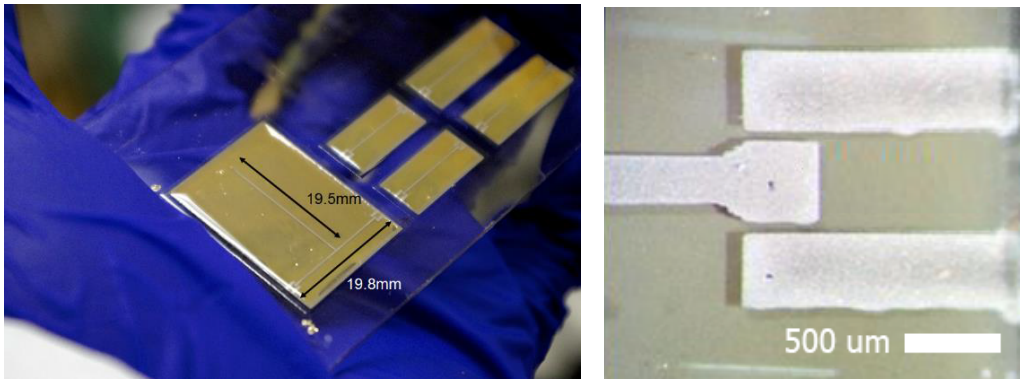

(a) (b)

Figure 53. Optical micrographs of: (a) Printed T-resonator, and (b) CPW to microstrip transition [101]

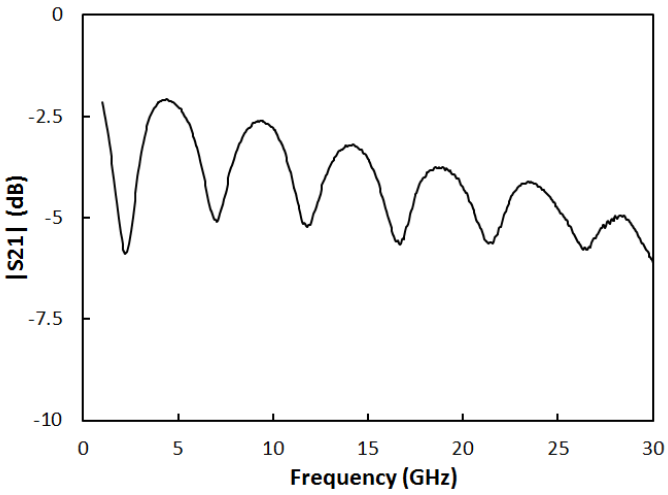

Figure 54. De-embedded insertion loss of the T-resonator

approximately 3.2. This agrees well with the manufacturer data sheet for the SU-8 polymer [96]. At higher frequency, the permittivity decreases to approximately 2.8. This is also confirmed in literature [102]. The average loss tangent over frequency is approximately 0.055, which also agrees well with published values in the literature of 0.04 [102].

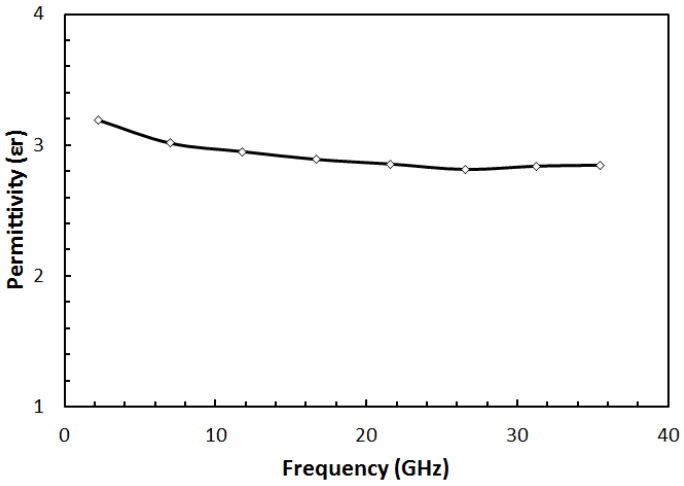

Figure 55. Extracted permittivity of the SU-8 thick film dielectric

4.2.5 Thin-Layer Dielectric Ink

While thick film dielectrics are essential for printed multi-layer RF components where large conductor spacing is required, thin-film dielectrics are also important for components such as high-valued metal-insulator-metal (MIM) capacitors. To produce thin layers, the poly(4-vinylphenol) or PVP, a polymer commonly used in printed transistor gates is adapted to the Dimatix printing platform. PVP is chosen as it is a long-chain, high molecular weight polymer which can be create high viscosity solution with very low w/w% content in a low-viscosity solvent. The PVP ink is targeted to produce layers of under 500 um per pass to allow for high capacitance structures. Table 8 shows the specifications of the thin-layer dielectric ink.

Table 8. Thick Layer Dielectric Ink Specifications

Material Loading	5 w/w% PVP Polymer
Cross-Linker	0.5 w/w% PMF or HMBG
Solvent	1-Hexanol 94.5w/w%
Density	0.85 g/mL
Falling-Ball Viscosity	12.1 cP
Surface Tension	29.3 mN/m
Post-Curing Surface Energy	38.2 mN/m
Z (1/Oh)	1.3

4.2.5.1 Material

The PVP polymer (Sigma Aldrich 436216), which is commonly used as a spin coated gate layer for organic transistors is a high molecular weight polymer (mW = 11,000) which can be cross-linked using methylated poly(melamine-co-fomaldehyde) (PMF) (Sigma Aldrich 418560) or (hydroxymethyl) benzoguanamine (HMBG) (Sigma Aldrich 441945)in a 20:1 w/w% ratio to form smooth, permanent films when the film is cured above 180°C for PMF and 120°C for HMBG [103–106]. An image of the polymer chain is shown in Fig. 56.

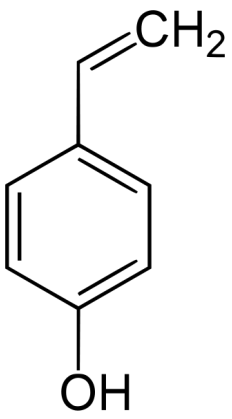

Figure 56. PVP polymer chain

4.2.5.2 Solvent Selection

PVP is readily dissolved in 1-hexanol (Sigma Aldrich 471402) which is a lower order alcohol (η = 4.5 cP, γ_L = 24.5 mN/m, *B.P.* = 159°C) [88–90, 107] and does not require a co-solvent as 1-hexanol satisfies the requirements for a printable ink. Other solvents such as n-propylene-glycol-methyl(PGMEA) are used which are better solvents for PVP, but they are toxic, and therefore not used in this work [105].

4.2.5.3 Viscosity and Surface Tension Measurements

To produce thin layers, it is important to decrease the polymer w/w%. To determine the lowest w/w% that yields an ink viscosity within the printable range, a parametric sweep of polymer w/w% loading in 1-hexanol is performed. Falling ball measurements in Fig. 57 show that at 5 w/w%, the viscosity is approximately 12.1 cP, which is well within the printable range. Increasing the solvent content to 10 w/w% brings the viscosity up to 29 cP which is an effect of the large molecular weight of the polymer. The rheometric analysis shown in Fig. 58 shows that the ink viscosity is very stable over sheer speed which is important for printability.

Surface tension measurements of the thin layer dielectric ink are performed on the Attension Theta Lite goniometer which yield a surface tension of 29.3 mN/m at 25°C.

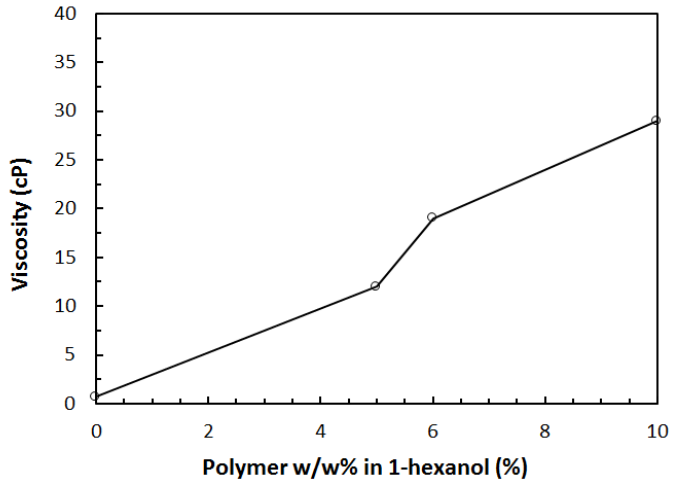

Figure 57. Falling ball viscosity of various w/w% PVP in 1-Hexanol

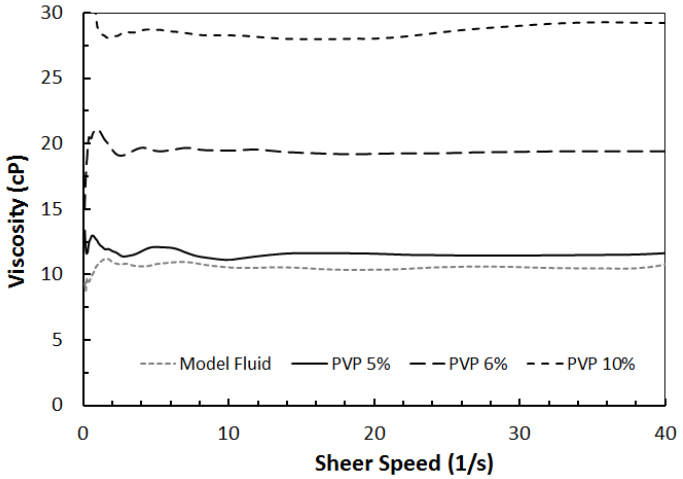

Figure 58. Rheometric analysis of various w/w% concentrations of PVP in 1-Hexanol

4.2.5.4 Thin Film Dielectric Waveform and Nozzle Temperature

The thin film dielectric ink is well-matched with the specifications of the Dimatix piezo inkjet nozzle, however, due to the lower density of the ink, the waveform must be modified to account for the change in wave propagation speed within the nozzle. Fig. 59 shows the modified waveform which is used for the thin-film dielectric ink which jets the ink well at frequencies up to 10 kHz. The nozzle temperature is increased to 40.5°C to optimize the jet-ability of the ink.

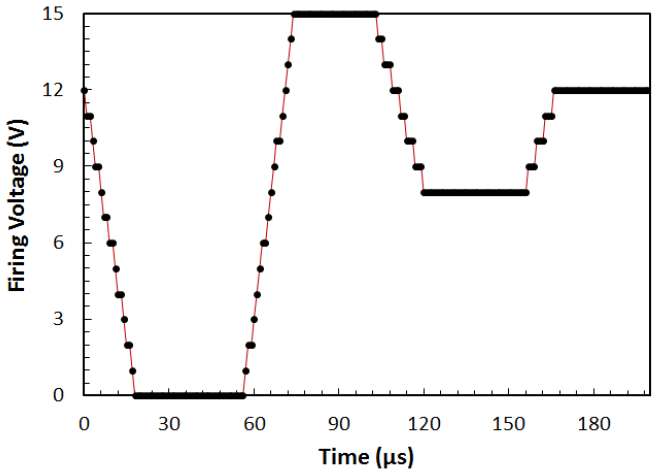

Figure 59. Waveform to jet thick-layer dielectric ink

4.2.5.5 Printed Film Measurements

The first characterization performed on the thick film dielectric ink is an analysis on the printed film thickness versus drop spacing. Square films are printed on a glass substrate to allow for surface profilometetry measurements of films with drop spacing varying from 20 - 25 um. Drop spacing above 25 um yield discontinuous films as the polymer w/w% is extremely low. Fig. 60 shows the surface profile measurements for the deposited films at room temperature. The films as jetted with the substrate at room temperature have an average thickness of 500 nm for 25 um spacing, and 750 nm for 20 um spacing. However, these films are rather rough and experience a large coffee ring effect. While the coffee ring effect cannot be avoided due to the low w/w% of PVP in the solvent system, the surface roughness which is caused by solvent evaporation patterns can be reduced by increasing the substrate temperature to cause localized drying upon drop impact with the substrate instead of bulk-film drying.

Fig. 61 shows the result of jetting PVP films on a substrate heated to 50°C. As expected, localized drying upon substrate impact greatly improves the formation of the films by reducing large-scale full film pulling effects caused by solvent evaporation, and localizing these forces to the area of drop impact. The film thicknesses remain at 500 nm and

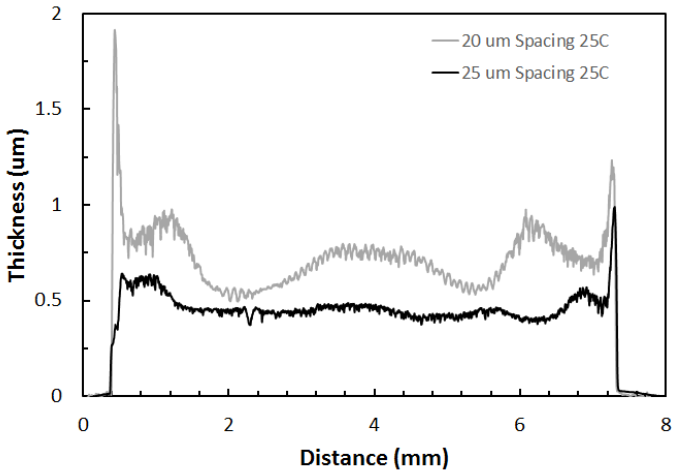

Figure 60. PVP film morphology versus drop spacing at room temperature

750 nm for 25 and 20 um drop spacing respectively, but with a large improvement in film uniformity and roughness.

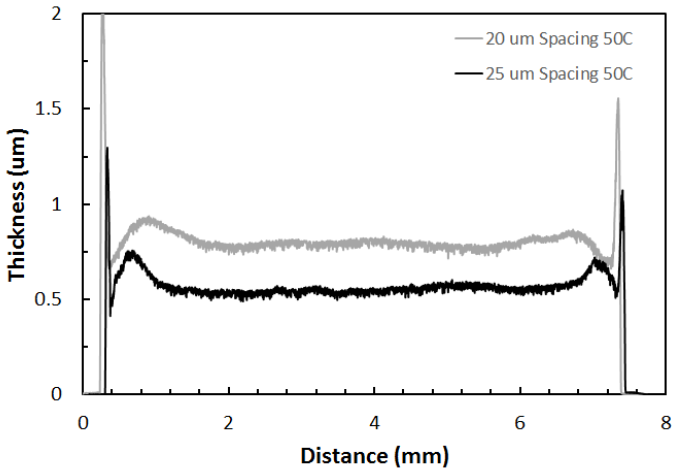

Figure 61. PVP film morphology versus drop spacing at 50°C

As the 25 um spaced films have a more uniform surface profile than the 20 um spaced films, the film thickness versus layer deposition test is performed for 25 um spacing only with the substrate heated to 50°C. The results, shown in Fig. 62, demonstrate a nearly linear increase of 500 nm per layer of the PVP thin-film dielectric ink.

To demonstrate the repeatability of the printed PVP films, a train of square films are printed and cured using 25 um spacing, and a substrate heated to 50°. Fig. 63 shows a

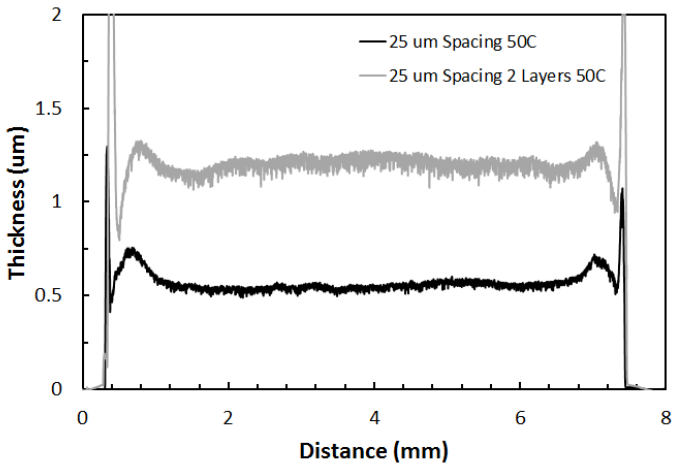

Figure 62. PVP film morphology versus number of layers at 50°C with 25 um drop spacing

surface profilometery measurement of the printed films. The thickness and surface morphology of the successively printed films are nearly identical meaning that batch fabricated devices should have similar characteristics when fabricated in the same run.

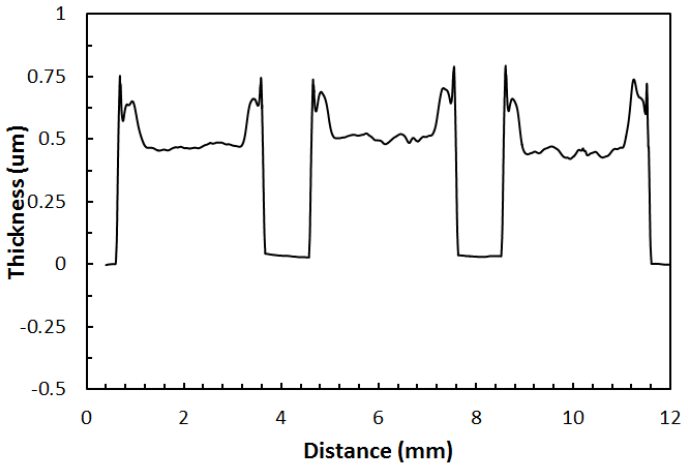

Figure 63. PVP single-layer film morphology repeatability

Following the cross-linking of the film, the free surface energy is measured using the contact angle method. It is important to know the surface energy for the printing of successive material layers. Two solvents of known surface energy, water (H_2O), and Glycerin are dropped onto the substrate and their contact angles are measured using an Attension Theta Lite goniometer. Fig. 64 shows the measured contact angles of both water and glycerin

on the post-cross-linked film. Water demonstrates a contact angle of 78.5°, and glycerin demonstrates a contact angle of 63.6°. This yields a surface tension of 38.5 mN/m which is high enough to allow for printing without surface energy modification through UVO exposure.

(a) (b)

Figure 64. Contact measurements on post-cross-linked SU-8 with (a) Water, and (b) DMSO

4.2.5.6 Electrical Characteristics

As the thin-film printed dielectric is extremely thin, it is difficult to characterize the ink using standard microstrip methods. To determine the permittivity of the ink, thin-film MIM capacitors, which will be demonstrated in the following section, are fabricated. Since the thickness of the dielectric is known, the permittivity can be extracted using the measured capacitance. Low frequency capacitance measurements yield a permittivity of 3.5 for the printed PVP. This is confirmed in the literature from measurements performed on spin-coated PVP used for transistor gates where the measured permittivity ranges from 3.46 - 4 based on the ratio of PVP to cross-linker in the solution [106, 108, 109]. The loss tangent, which is confirmed in simulation for the capacitors, is near 0.03 which is also confirmed in literature which cites the loss tangent of PVP to be 0.02 [110, 111].

4.3 Finalized Ink and Processing Parameters

After optimizing the printing conditions for each ink, and characterizing the printed films, a final set of processing rules are generated which will be discussed in this section, and which can be utilized by designers using the VIPRE process for accurate layout and modeling purposes. This is the first time a rule set for an inkjet-printing process has been generated, and will with hope, enable a much wider audience to generate complex and high-impact inkjet-printed structures not only for RF applications, but in any field which can benefit from additive, flexible, and low-cost fabrication.

Before going into the processing rules, an analysis of the final four inks is performed with respect to the ink formulation map specified in Section 3.3.1. Each of the four inks which are designed for the VIPRE process are plotted in Fig. 65. Notice that each of the inks falls within the 'printable ink' range. The inks are slightly to the right side of the jetable range, however, this was to keep the viscosity on the lower end which allows the print head to be kept at room temperature which mitigates nozzle drying.

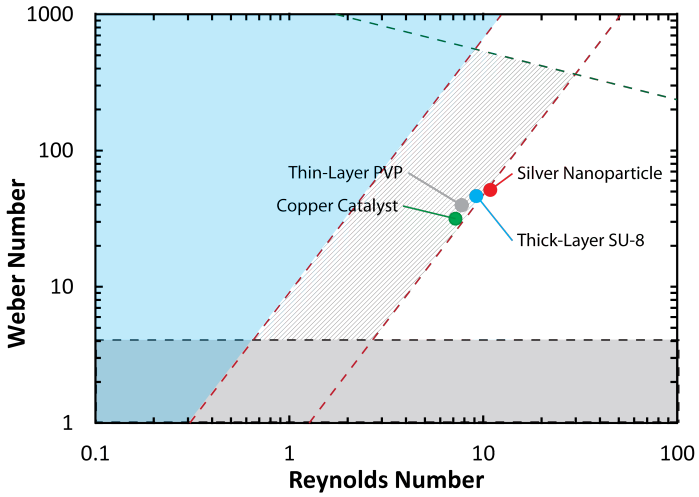

Figure 65. Analysis of jetability of VIPRE inks

The processing rules for VIPRE are as follows:

Passivation Layer:

Typically, Metal 1 can be deposited without the use of a passivation layer as long as the

host substrate is smooth and the surface energy of the substrate can be brought to 40 mN/m. However, if this is not the case, such as in the case of a silicon wafer, a passivation layer must be deposited. The passivation layer can be either the SU-8 or PVP ink. However, the SU-8 ink typically performs the best as it has excellent adhesion to nearly any host substrate. The processing conditions for an SU-8 passivation layer are shown in Table 9.

Table 9. SU-8 Passivation Layer Processing Conditions

Pre-Print Processing	30 Seconds UVO Clean
Sub-Layer Surface Energy	N/A
Platen Temperature	25°C
Curing Method	90°C Pre-Bake, 365nm UV Exposure, 120°C Post-Bake
Film Thickness: 20um Drop Spacing	6 um/layer
Surface Roughness	53 nm/layer (0.8%)
Cured Film Surface Energy	30 mN/m
Surface Energy Adjustment	60s UVO Exposure

Metal 1 (M1) -

Following the preparation of the substrate, which is either inherently printable, or treated with a passivation layer, the first metal layer (M1) is deposited. Typically the silver nanoparticle ink is used unless the substrate is porous. The processing conditions for M1 are as follows:

Table 10. Silver Nanoparticle Ink Processing Conditions

Sub-Layer Surface Energy	40 mN/m
Platen Temperature	25°C
Curing Method: Oven	180°C for 30 minutes
Curing Method: Laser	Raster, 75 W, 10 m/s
Film Thickness: 20um Drop Spacing	450 nm/layer
Surface Roughness	6 nm/layer (1.3%)
Cured Film Surface Energy	800 mN/m
Surface Energy Adjustment	N/A

Dielectric 1 (SU-8) -

If the inter-layer dielectric is specified to be a thick-layer dielectric, the thickness of the dielectric needs to be considered as after printing 3 to 4 layers, a re-flow needs to be performed to smooth the film. And, if a film above 50 um, or approximately 7 layers, is to be printed, a reflow and cure is required before increasing the film thickness above 50 um to maintain a flat film profile. The processing conditions for an SU-8 dielectric are as follows:

Table 11. SU-8 Dielectric Ink Processing Conditions

Sub-Layer Surface Energy	40 mN/m
Platen Temperature	25°C
Pre-Cure (>3 layers)	Hot Plate 1-2 min, 150°C
Curing Method	90°C Pre-Bake, 365nm UV Exposure, 120°C Post-Bake
Film Thickness: 20um Drop Spacing	6 um/layer
Surface Roughness: 20um Drop Spacing	53 nm/layer (0.8%)
Cured Film Surface Energy	30 mN/m
Surface Energy Adjustment	60s UVO Exposure

Dielectric 1 (PVP) -

Typically, the PVP dielectric is only used for capacitive structures such as MIM caps. Therefore, it is assumed that more than 5 layers of the ink will not be printed. The processing conditions for a PVP dielectric are as follows:

Tables 9 - 12 show the basic processing conditions for layer-by-layer deposition. To deposit further metal and dielectric layers, the same steps should be followed as those for the previous layers.

Table 12. PVP Dielectric Ink Processing Conditions

Sub-Layer Surface Energy	40 mN/m
Platen Temperature	40-50°C
Curing Method: PMF X-linker	Ramp 50-180°C, hold 5 min
Curing Method: HMBG X-linker	Ramp 50-120°C, hold 1 hour
Film Thickness: 20um Drop Spacing	750 nm/layer
Surface Roughness: 20um Drop Spacing	17 nm/layer (2.2%)
Film Thickness: 25um Drop Spacing	500 nm/layer
Surface Roughness: 25um Drop Spacing	13 nm/layer (1.8%)
Cured Film Surface Energy	39 mN/m
Surface Energy Adjustment	N/A

CHAPTER 5

VERTICALLY INTEGRATED INKJET RF PASSIVES

Historically, when it comes to printed lumped components (i.e. inductors, capacitors, and resistors), inkjet technology has been used to fabricate low-frequency, single-layer or planar implementations. This planar constraint greatly limits design and performance capabilities of lumped components which are an essential piece to the long-term goal of creating fully printed systems. However, by using the well-characterized VIPRE process, efficient multi-layer lumped components can be produced for high frequency applications which far outperform current printed components [112, 113]. This chapter demonstrates the first printed implementations of vertically integrated capacitors and inductors which operate into the GHz range with quality factors (Q) that far outperform current state-of-art printed components.

5.1 Vertically-Integrated Capacitors

To date, low-frequency vertically-integrated printed capacitors have been demonstrated in the literature which operate up to 10 MHz with no data on the Q [72–77]. However, multi-layer printed MIM structures have yet to be demonstrated and optimized for operation at microwave frequencies through several GHz. Printed microwave capacitors have a wide variety of applications, ranging from printed flexible and wearable wireless systems, to post-processing of large-value capacitors on-chip to reduce chip area requirements which greatly reduces cost.

This section includes the process flow for creating MIM capacitors utilizing the VIPRE process which can demonstrate multi-layer RF capacitors that have self-resonant frequencies (SRF) above 3 GHz and Q values above 8.

5.1.1 Capacitor Process Flow

The process flow for printing MIM capacitors using the VIPRE process is as follows. First, the host substrate is cleaned and the surface energy is adjusted to 40 mN/m with a UVO treatment. Following cleaning, silver nanoparticle ink is then printed onto the host substrate and cured at 150°C for 1 hour to form the bottom electrode. Either the thin or thick dielectric layer can be used as the dielectric layer for the capacitors. In the case of the thin-layer dielectric, the dielectric layer is printed and then cured for 5 minutes at 180°C. In the case of the thick-layer dielectric, the dielectric layer is printed, pre-exposure baked at 90°C for 5 minutes, given a thickness-dependent dose of 365 nm UV, post-exposure baked at 120°C, and then exposed to UVO for 90 seconds to raise the surface energy to 40 mN/m. After the printing of the dielectric layer, the top electrode is printed using the silver nanoparticle ink. The entire structure is then cured at 180°C for 1 hour to finish the process.

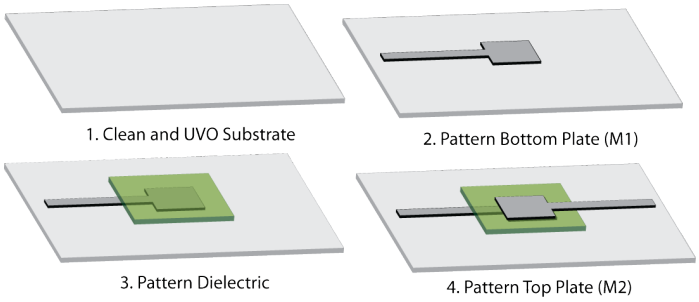

Figure 66. Process for fabricating MIM capacitors

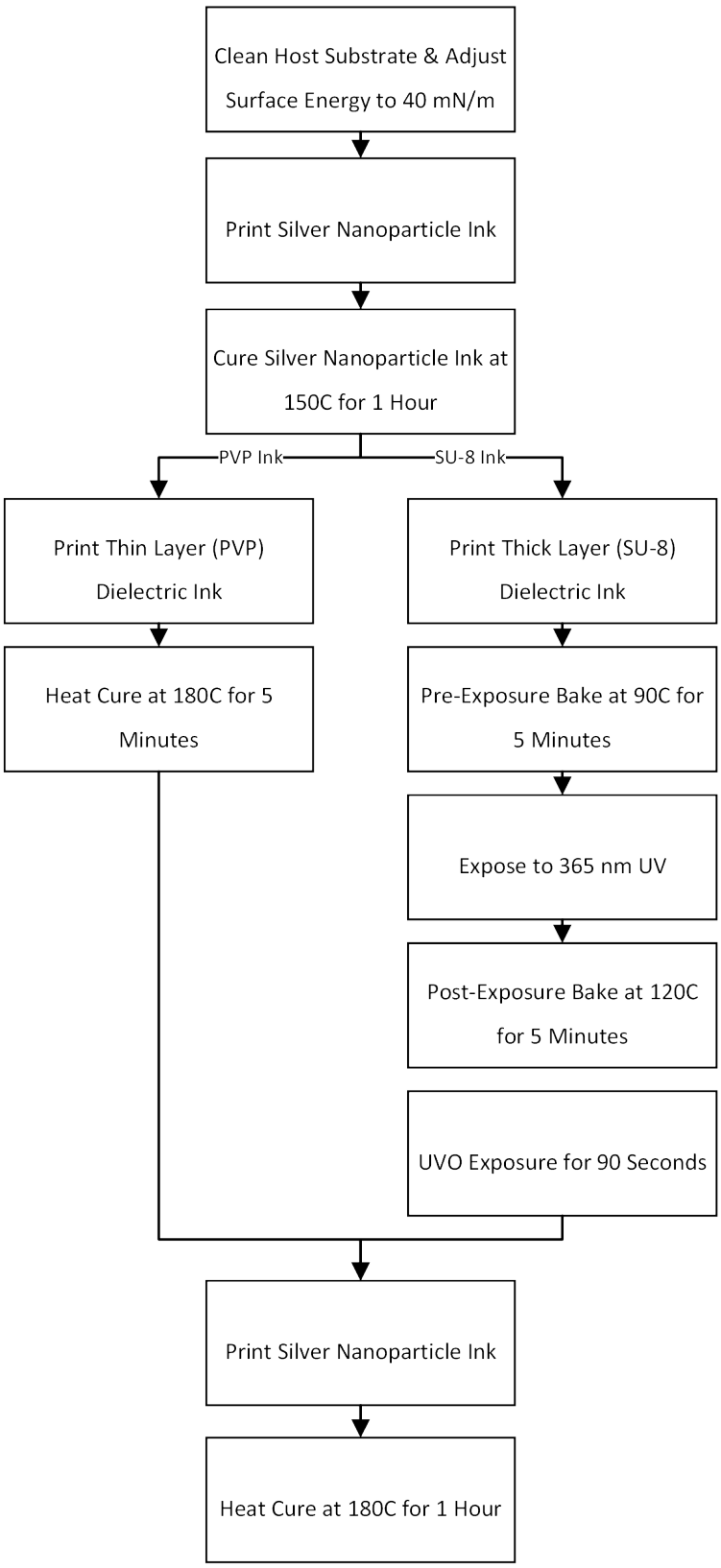

Figure 67. Process flow for fabricating MIM capacitors

5.1.2 Fabricated Capacitor Results

Microstrip-fed MIM capacitors with both the thin, and thick-layer dielectric inks are designed for a 250 um thick Kapton substrate to allow for a comparative analysis of capacitor performance versus dielectric material. The plate dimensions of the microstrip capacitors are varied from 0.5 x 0.5 mm^2, the width of the microstrip line, to 1.5 x 1.5 mm^2 in the parametric analysis. A batch of printed MIM capacitors is shown in Fig. 68. Fig. 69 shows an SEM cross section of the printed capacitors where the layers from bottom to top are Kapton (gray), silver nanoparticle (white), PVP (dark gray), and silver nanoparticle (white).

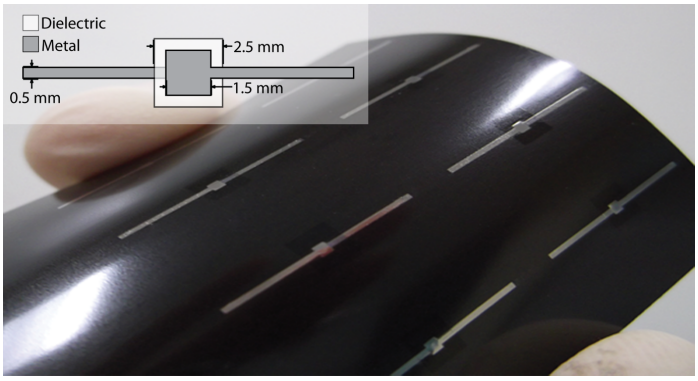

Figure 68. Batch of fabricated MIM capacitors on a flexible substrate

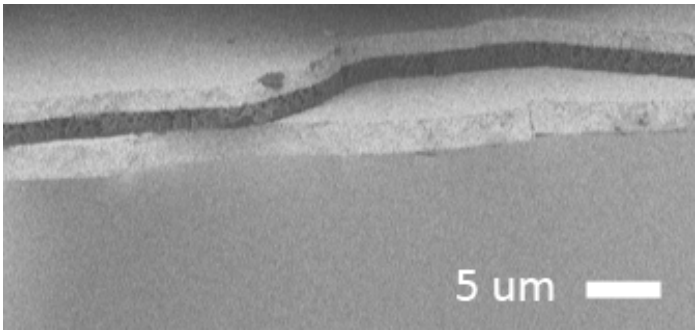

Figure 69. SEM cross section of the printed capacitor on a Kapton Substrate

To test the printed capacitors, SMA connectors are mounted using a silver epoxy and the S-parameters of the microstrip capacitors are extracted using a Rhode and Schwartz ZVA-8 VNA. A printed TRL calibration kit utilizing the same fabrication process as the

capacitors is used to remove the effects of the connectors and feed lines, and move the reference plane to the edge of the printed dielectric. The frequency dependent capacitance is then extracted directly from the de-embedded S-parameters.

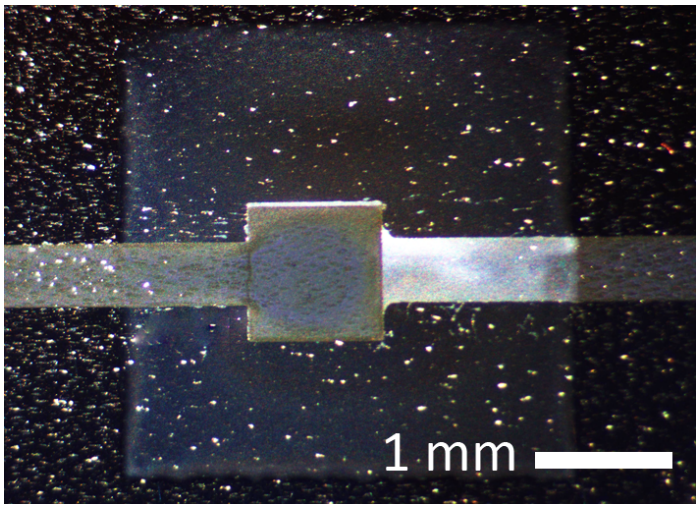

Figure 70. Optical micrograph of a printed capacitor on a Kapton Substrate

The first test is to compare printed capacitors with 1.5 x 1.5 mm^2 plates fabricated with both the PVP and SU-8 dielectric inks. To prevent shorting of the capacitor plates due to pin-holing with these large plate dimensions, which is caused by microscopic bubbles and dust particulates in the dielectric layer, two layers of the SU-8 ink are printed with drop spacing of 30 um, and three layers of the PVP ink are printed with drop spacing of 25 um. This yields dielectric layers with average thicknesses of 4 and 1.2 um respectively.

The simulation results from Computer Simulation Techology's (CST) full-wave frequency domain solver are plotted along with the de-embedded measurement results for the printed capacitors with 1.5 x 1.5 mm^2 pads in Fig. 71. The capacitance of the SU-8 dielectric-based capacitor is 20 pF with a self-resonance of approximately 3 GHz. The capacitor with the PVP-based dielectric shows a capacitance at 50 pF for the same plate dimensions with a self-resonance of 1.9 GHz. The lower self-resonance for the PVP dielectric-based capacitor is expected due to the higher capacitance value. The maximum Q for both capacitors seen in Fig. 71 is approximately 4. This Q value, which is lower than

that of conventional discrete components, is due to the thin metal layer (1.5 um for M1 and M2) and the higher loss tangent of the printed dielectrics.

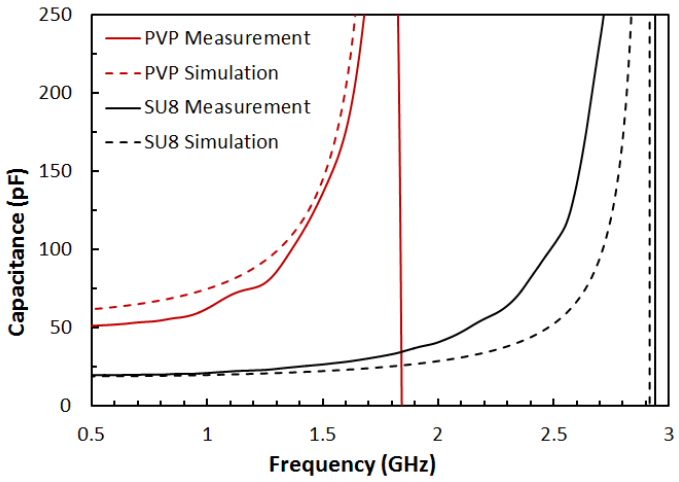

(a)

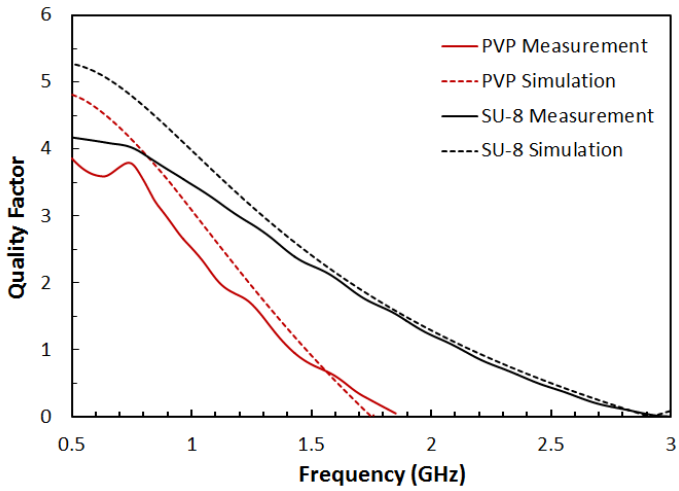

(b)

Figure 71. PVP and SU-8 dielectric capacitor measurements for (a) capacitance, and (b) quality factor

As the results from the capacitors with PVP dielectric provide higher capacitance for a smaller area, and a higher Q for a larger capacitance as expected, further parametric analysis is performed utilizing the PVP dielectric. In Fig. 72, capacitors with plate dimensions of 0.5 x 0.5 (0.8 um thick dielectric), 1 x 1 (1.2 um thick dielectric), and 1.5 x 1.5 mm^2 (1.2 um thick dielectric) are plotted against simulation. The 0.5 x 0.5mm^2 capacitor is designed with only two layers of PVP unlike the 1 x 1 and 1.5 x 1.5 mm^2 iterations as pin-holing is

not a big issue with smaller plate dimensions. The realized capacitance for the three plate dimension variations are 10, 28, and 50 pF, respectively. The measurements agree well with simulation and slight discrepancies are due to small variations in dielectric thickness and misalignment between printed layers. The measured Q for the capacitors ranges from 4 to 8 as shown in Fig. 72, which is the highest known Q for printed components reported in the literature.

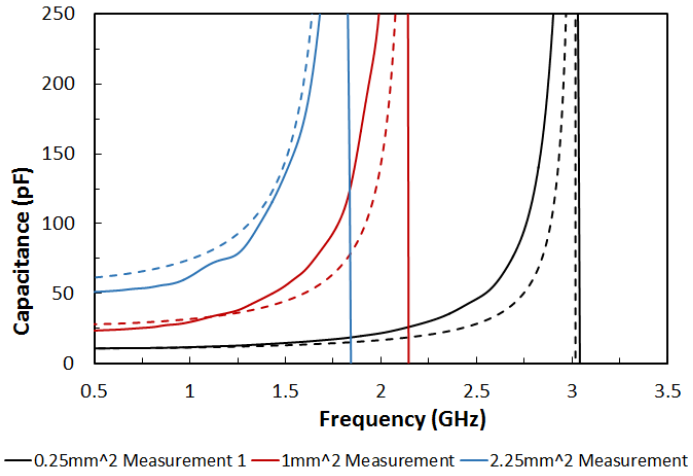

(a)

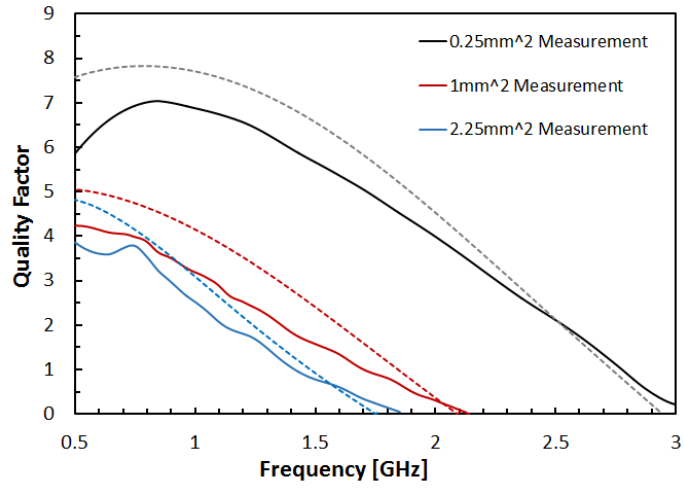

(b)

Figure 72. PVP dielectric capacitor measurements for (a) capacitance, and (b) quality factor

To demonstrate the repeatability of the process, three separate capacitors with plate dimensions of 0.5 x 0.5 mm^2 are shown, with the capacitor designated as Measurement 3

having an extra two printed layers of silver nanoparticle ink (2.5um thick metal layers) to test the effect of metallization thickness on capacitor Q. As shown, the capacitors designated as Measurement 1 and 2 are in close agreement having capacitances of 10.8 and 10.9 pF respectively. As the two extra printed layers of silver on the third capacitor cause slight ink-spreading making the plates wider, its capacitance is slightly larger at 12.5 pF. However, the Q which is shown in Fig. 73 is improved with the extra two silver layers by approximately 20%.

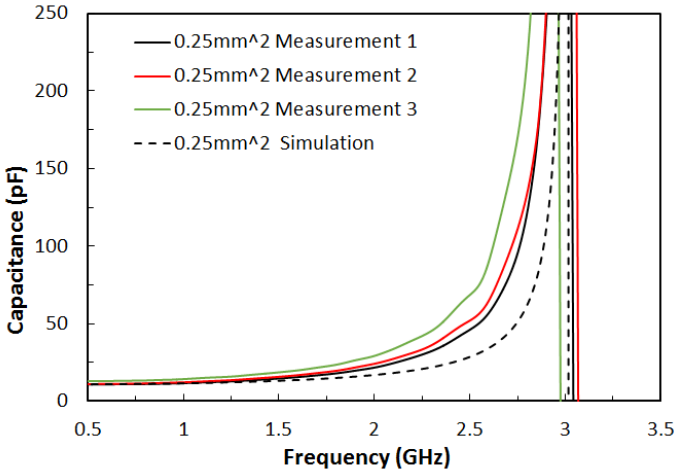

(a)

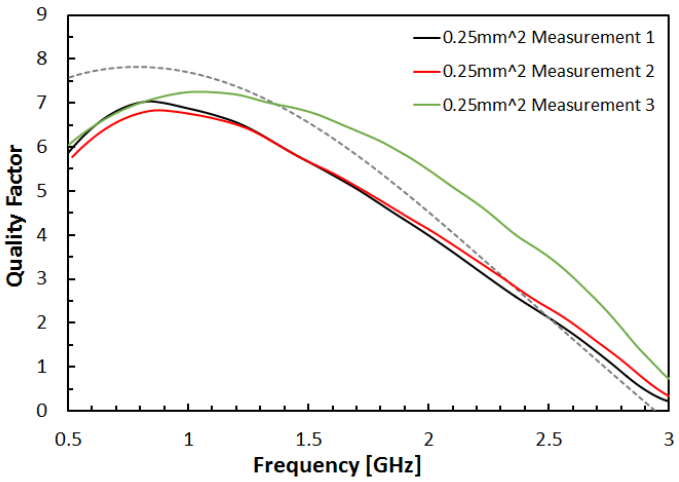

(b)

Figure 73. PVP dielectric capacitor measurements for (a) capacitance, and (b) quality factor

5.1.3 Vertically-Integrated Capacitor Conclusions

The microwave capacitors produced have values up to 50 pF and self-resonant frequencies of up to 3 GHz allowing for use in the 800 MHz RFID and 2.4 GHz bands. With a smaller capacitance, the SRF can be pushed well above 3 GHz. The repeatability of the process is demonstrated to be within 1-2% when the same processing conditions are used making it usable in practical mass manufacturing applications for system on package, communication, filtering, and sensing.

5.2 Vertically-Integrated Inductors

To date, there has been very little investigation into inkjet-printed lumped components, which are essential to building fully-printed modules. The best performing printed inductive component as of yet has been obtained by Menicanin et al. with a planar meander inductor printed on a flexible kapton substrate that has a maximum Q of 3 and an inductance of 2 nH [114]. More compact multi-layer designs have also been demonstrated by Kang et al. who have demonstrated a spiral inductor with an inductance of 200 nH for low frequency applications below 1 MHz [78], and Redinger et al. who have demonstrated a multi-layer spiral inductor with a Q of 0.5 and an inductance of 350 nH at 13.56 MHz [115].

However, to produce efficient fully-printed modules, printed inductors and transformers with high quality factors are required which can be repeatably fabricated utilizing multi-layer inkjet technology. In this section, high frequency multi-layer inductors with a high Q are demonstrated for the first time utilizing the VIPRE process. The results demonstrate the current ability to rapidly and reliably fabricate high-performance multi-layer inductors a low-cost inkjet printing platform.

5.2.1 Inductor Process Flow

The process flow for fabricating multi-layer spiral inductors using the VIPRE process is as follows: The first step in the process involves cleaning the liquid crystal polymer (LCP) substrate. A 6 um thick SU-8 adhesion layer is then printed onto the substrate to smooth the surface and tune the surface energy of the substrate to allow for the printing of successive layers with good adhesion and surface wetting. This step is extremely important to allow for a substrate-independent process. The SU-8 adhesion layer is then cured using the standard SU-8 curing procedure, and exposed to UVO for 90 seconds to increase the surface tension. Following the printing of the adhesion layer, the first metal layer is deposited using the silver nanoparticle ink and cured at 180°C for 1 hour. The SU-8 dielectric layer for the inductor bridge is then patterned, cured, and exposed to 90 seconds of UVO. To create vias, holes are left in the patterned dielectric layer when printed and the successive metal

layer is printed into the hole which allows for low resistance contacts of less than 0.1Ω between layers. The second metal layer is then deposited to connect both sides of the inductor, and cured at 180°C for 1 hour.

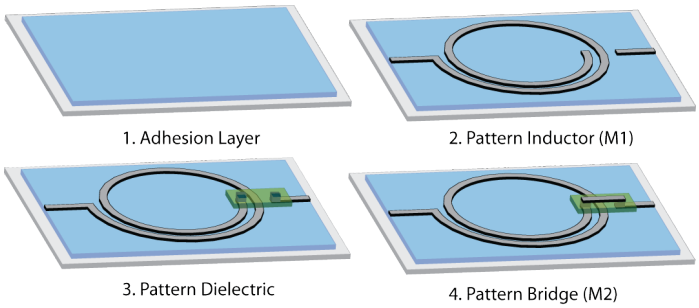

Figure 74. Process for fabricating multi-layer spiral inductors

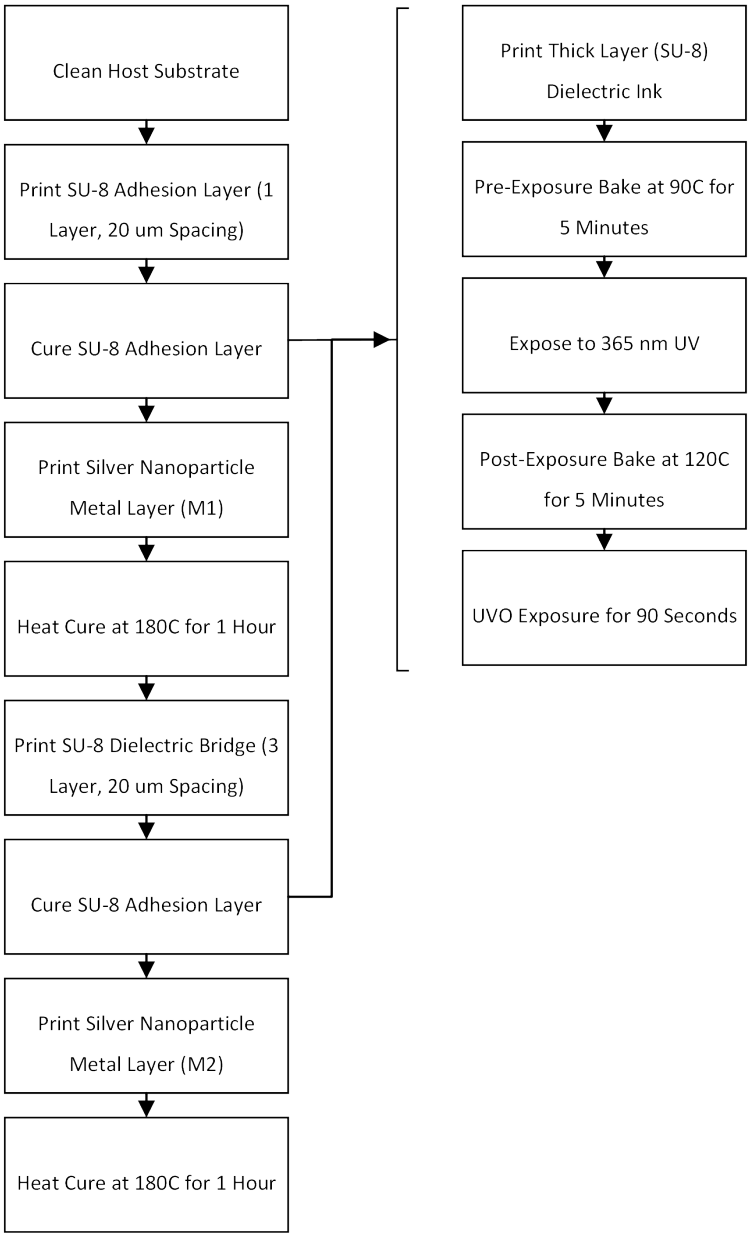

Figure 75. Process flow for fabricating multi-layer spiral inductors

5.2.2 Fabricated Inductor Results

The inductor design used in this work, which is shown in Fig. 76, is a CPW-fed inductor which is probe fed with 500 um pitch Cascade ACP40-GSG-500 GSG probes connected to an Anritzu 37369A 40 GHz VNA. The probes are calibrated up to the end of the probe tips utilizing a wide pitch GSG ISS. The inductors, which are on 100 um thick LCP are adhered to a 1.25 mm thick glass slide to separate the inductors from the metal chuck. The measurement setup is accounted for in simulation results.

The first test compares the inductance and Q values of 0.5 turn inductors with 3, 4, 5, and 10 layers of printed silver nanoparticle ink. Fig. 77 shows the measured inductance and Q-values which are extracted from the measured S-parameters. The inductance value of all of the measured inductance ranges between 8.91 and 9.68 nH (7.5% variation) with

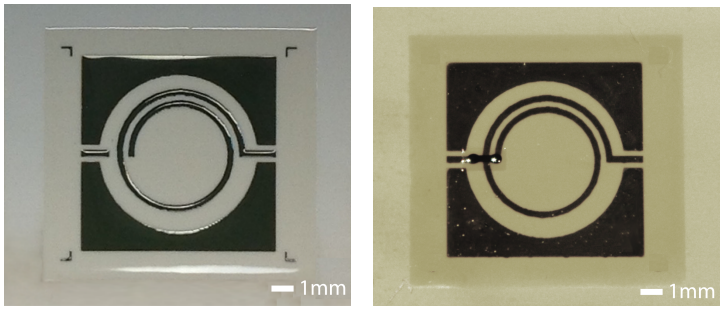

(a) (b)

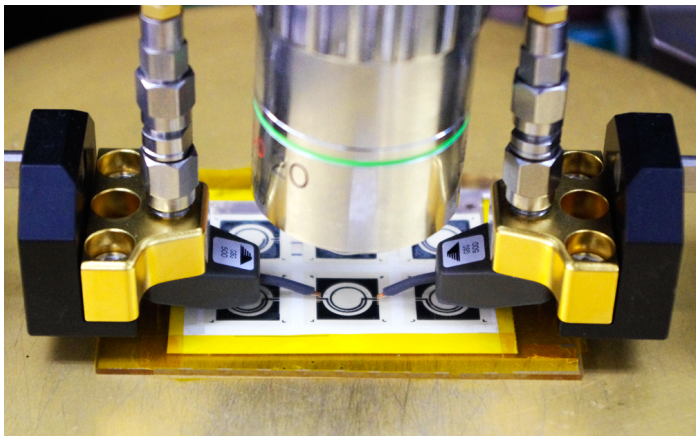

(c)

Figure 76. (a) 1.5 turn inductor after M1 deposition, (b) 1.5 turn inductor after M2 depositon, and (c) measurement setup

a SRF of 6.7 GHz. The Q steadily increases from 8.3 with 3 metal layers, to 20.7 with 10 metal layers. The results of the printed 0.5 turn inductor yield a 7x improvement in Q for a 5x larger inductor than the state-of-the-art printed planar inductors in the literature [56].

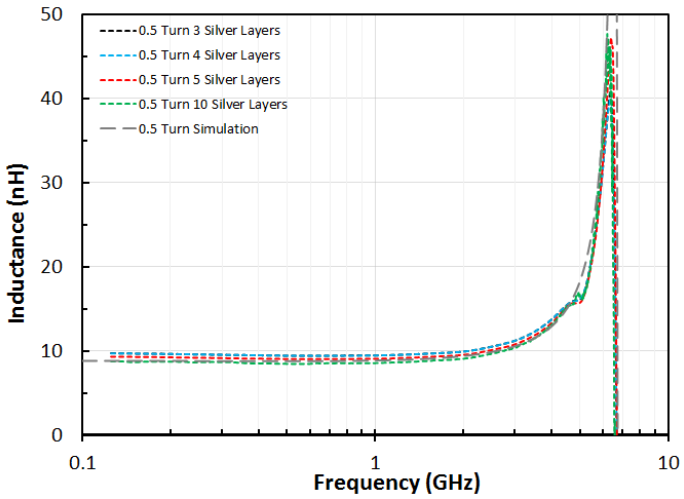

(a)

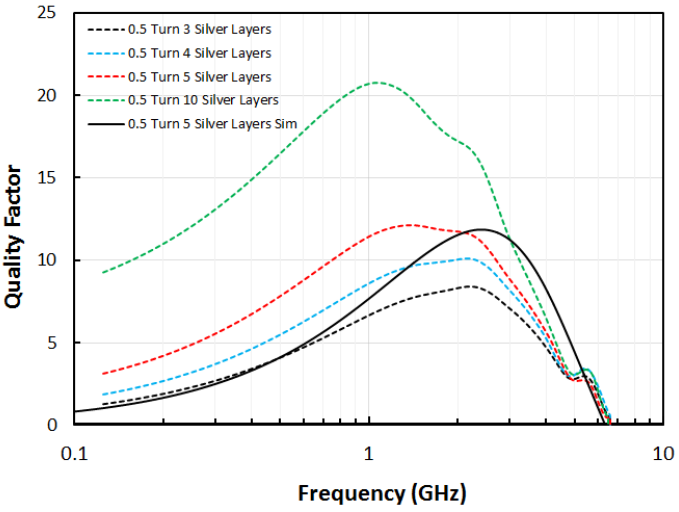

(b)

Figure 77. 0.5 Turn inductor measurements with (a) inductance value, and (b) quality factor

Following testing of the 0.5 turn inductors, the 1.5 turn inductors are measured for inductance and Q. Fig 78 shows the measurement results of the 1.5 turn inductor which has an inductance varying between 25.4 and 25.7 nH (1% variation) over the three fabrication runs. The measured Q increases from 6.6 with 3 metal layers to 8.6 with 5 metal layers.

All results align well with the simulated results from CST.

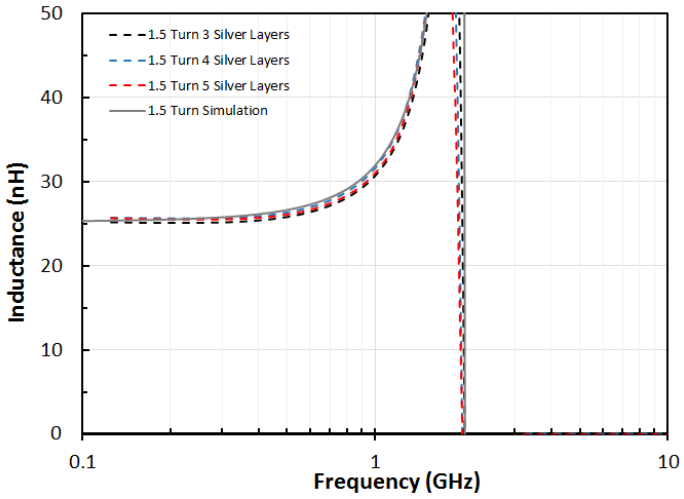

(a)

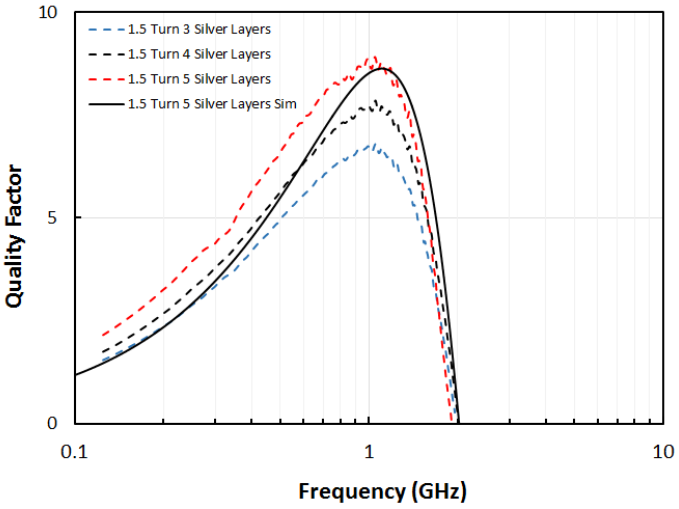

(b)

Figure 78. 1.5 Turn inductor measurements with (a) inductance value, and (b) quality factor

5.2.3 Vertically-Integrated Inductor Conclusions

The inkjet-printed inductors not only outperformed current state-of-the-art printed inductors by an order of magnitude in Q and inductance, but were also extremely reliable between fabrication runs having deviations in inductance values of less than 8% for the 0.5 turn inductors, and less than 2% for the 1.5 turn inductors. This high level of performance

and repeatability, as well as the excellent measurement simulation agreement shows the promising potential of multi-layer inkjet processing for commercial fabrication of passive components.

CHAPTER 6

VERTICALLY INTEGRATED INKJET MM-WAVE ANTENNAS

Historically, inkjet-printing has been used in the RF field to fabricate low-frequency, single-layer antennas on organic substrates for wearable and RFID applications [24, 67, 68, 116, 117]. The state-of-the-art printed antennas in the literature reach maximum frequencies of 12 GHz, and typically have relatively low gains due to the lack of a well-characterized printing process. However, by utilizing the VIPRE process, inkjet technology can be utilized to fabricate high gain multi-layer mm-Wave components and antennas directly onto conformal substrates, wafers, and integrated circuit (IC) packaging to increase the level of integration available to the growing millimeter-wave (mm-Wave) wireless industry, whether it is for single die, or large area array applications. By enabling the direct and rapid printing of mm-Wave antenna onto ICs and packages, a new level of flexible design capabilities that are not available with traditional RF fabrication techniques become available.

In this chapter, the VIPRE process is utilized to demonstrate multi-layer proximity-coupled patch antennas and antenna arrays for the 24 GHz ISM band [118]. The return loss and radiation pattern of the antennas are characterized, and a comparison of the repeatability between fabrication runs is presented. The results demonstrate the current ability to rapidly and reliably fabricate multi-layer mm-Wave antennas utilizing a low-cost inkjet printing platform.

6.1 Single Element Proximity-Fed Patch Antennas

To demonstrate the advantages of the multi-layer inkjet process for package-integrated mm-wave antennas, a proximity-coupled patch antenna is designed for the 24.5 GHz ISM band. Proximity-coupled patch antennas have the advantage of featuring a wider bandwidth and are easier to tune than standard microstrip or probe-fed patch antennas; however, this comes at the cost of requiring multi-layer boards [119, 120]. Before the creation of the VIPRE

process, these types of designs were not realizable with fully-additive inkjet-printing technology. The proposed proximity coupled patch is shown in Fig. 79.

The proximity-fed patch antenna is designed to be fabricated on a 100 um thick single-clad LCP substrate. Utilizing the physical and electrical parameters of the characterized printing process, the CST frequency domain solver is used to optimize the patch dimensions, printed dielectric thickness, and inset-feed length to have an input impedance of 50Ω at 24.5 GHz while maximizing realized gain in the broadside direction. The optimal dimensions shown in Fig. 79 are for a printed SU-8 dielectric thickness of 40 um, or approximately 6 printed layers of SU-8. To determine the required thickness of the silver layers, the skin depth is calculated to be approximately 1 um at the center frequency of operation. Two batches of the antennas have been printed with 3 layers of silver (1.5 um thickness), and 5 layers of silver (2.5 um thickness), to verify that the skin depth requirements are met with 3 or more layers of silver.

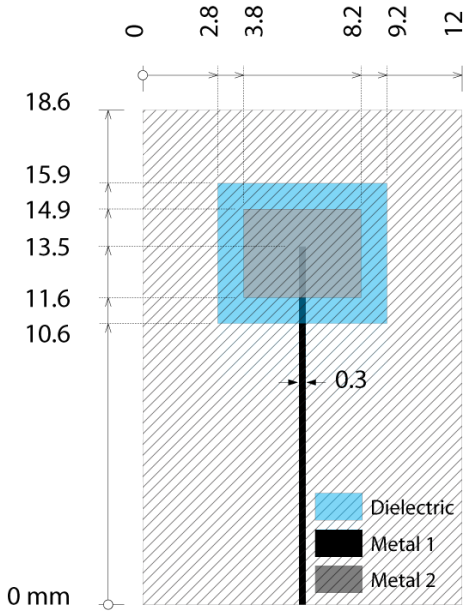

Figure 79. Design of proximity-fed patch antennas

6.1.1 Proximity-Fed Patch Antenna Process Flow

The process flow for printing the mm-Wave proximity-fed patch antennas using the VIPRE process is as follows. First, the LCP substrate is cleaned and the surface energy is adjusted to 40 mN/m with a UVO treatment. Following cleaning, silver nanoparticle ink is then printed onto the host substrate and cured at 180°C for 1 hour to form the microstrip feed line. The thick-layer SU-8 dielectric layer is then printed, pre-exposure baked at 90°C for 5 minutes, given a thickness-dependent dose of 365 nm UV, post-exposure baked at 120°C, and then exposed to UVO for 90 seconds to raise the surface energy to 40 mN/m. After the printing of the dielectric layer, the patch is printed using the silver nanoparticle ink. The entire structure is then cured at 180°C for 1 hour to finish the process.

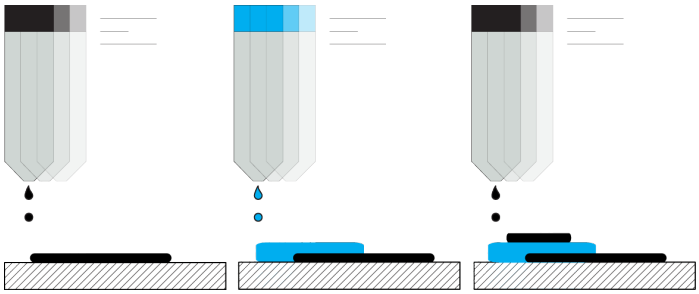

Figure 80. Process for fabricating proximity-fed patch antennas

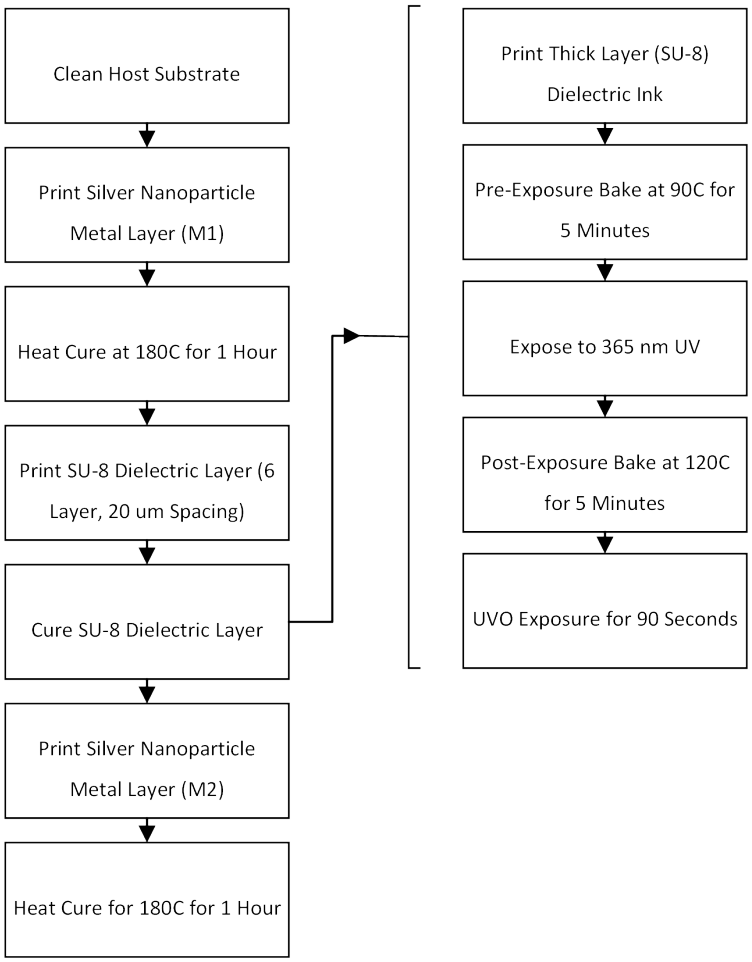

Figure 81. Process flow for fabricating proximity-fed patch antennas

6.1.2 Proximity-Fed Patch Antenna Results

An optical micrograph of the fabricated patch antenna prototype is shown in Fig. 82. Post fabrication measurements show the dielectric thickness to be 35 um, which is expected for 6 printed layers of SU-8, and the patch length and width to be 3.38 mm and 4.52 mm respectively. The slightly longer length and width dimensions of the patch from the layout are caused by drop spreading as the printing software specifies drops centered on the borders of the layout. The slight changes in dimensions are accounted for in the final simulations. Following fabrication, the LCP carrier substrate is diced and clamp-mount Southwest Microwave end launch connectors are affixed to the antenna to allow for measurement of the input impedance and radiation characteristics.

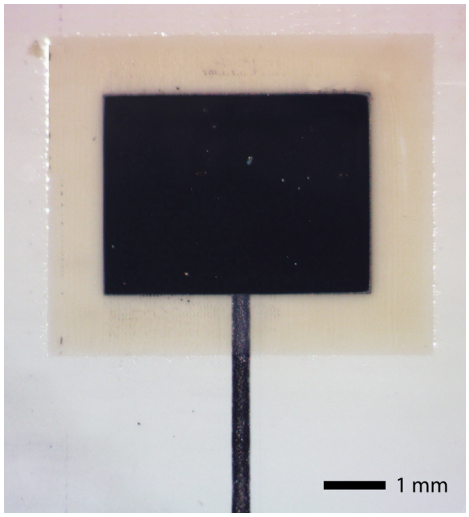

Figure 82. Optical micrograph of the proximity-fed patch antennas

The return loss for both the three and five silver layer patch antennas is measured on an Anritzu 37369A VNA and displayed in Fig. 83 and compared with the simulation of the 3 silver nanoparticle-layer patch. It can be seen that the 3-layer patch is matched well with the simulation and is well-matched to 50 ohms at 24.4 GHz. The 5-layer patch is well-matched at a lower frequency of 24.2 GHz which is caused by increased ink spreading due to the higher volume of dispensed ink. The return loss results show that even between fabrication batches with different processing parameters, the inkjet process produces very

repeatable results within 1%.

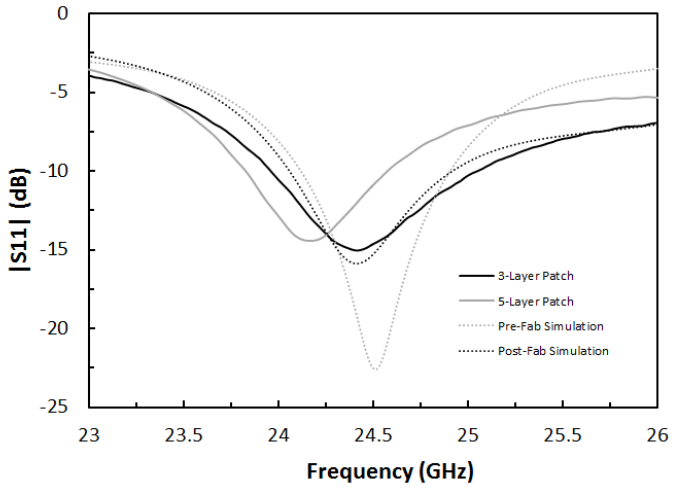

Figure 83. Return loss measurement of the proximity-fed patch antennas

To measure the radiation pattern and gain, a far-field chamber located at GTRI, shown in Fig. 106, which is calibrated using SA12A-18 standard gain horn antennas is utilized. The broadside realized gain values versus frequency of the 3 and 5-layer patch antennas are measured and compared with simulation in Fig. 85. The peak realized gain is approximately 4 dBi for both patch antennas. The results confirm that a conductor realized with 3-layers of silver is thick enough to account for skin depth above 24.5 GHz. The measured and simulated radiation patterns displayed in Figs. 86(b) and 86(a) are in good agreement. The slight discrepancies between measurement and simulation in the E-plane radiation pattern cut are due to the connector and feeding cables, which are positioned -90°, not being included in the simulation to minimize computational time.

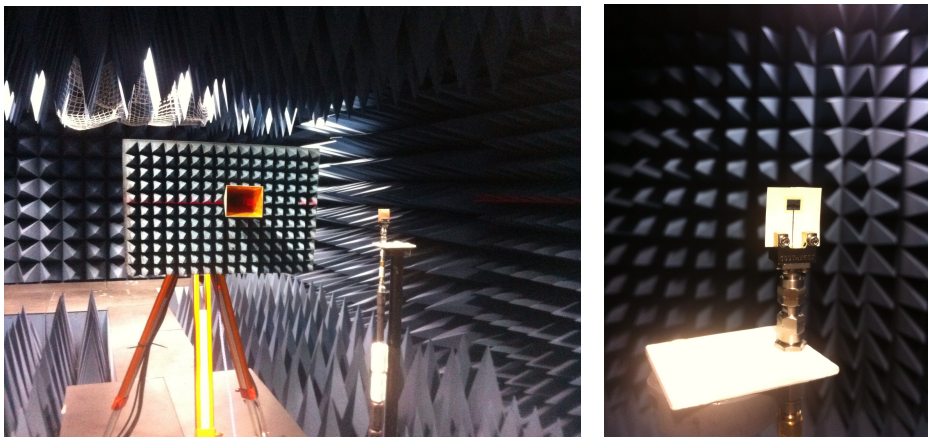

(a) (b)

Figure 84. (a) Antenna measurement setup, and (c) Zoomed in view of antenna mounting configuration

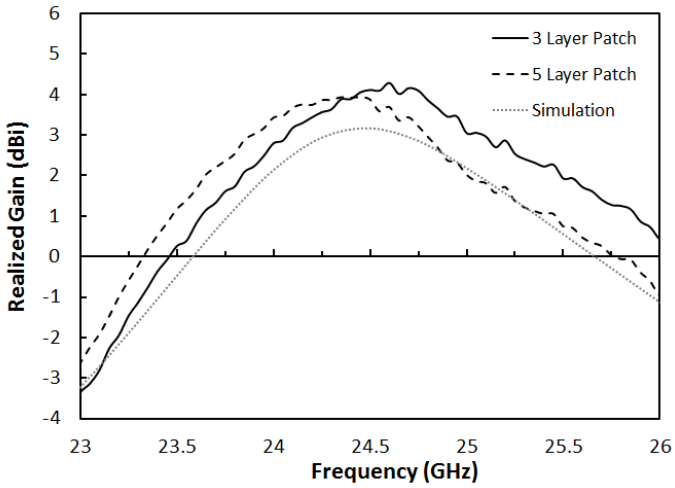

Figure 85. Simulated and measured broadside realized gain versus frequency of the proximity-fed patch antennas

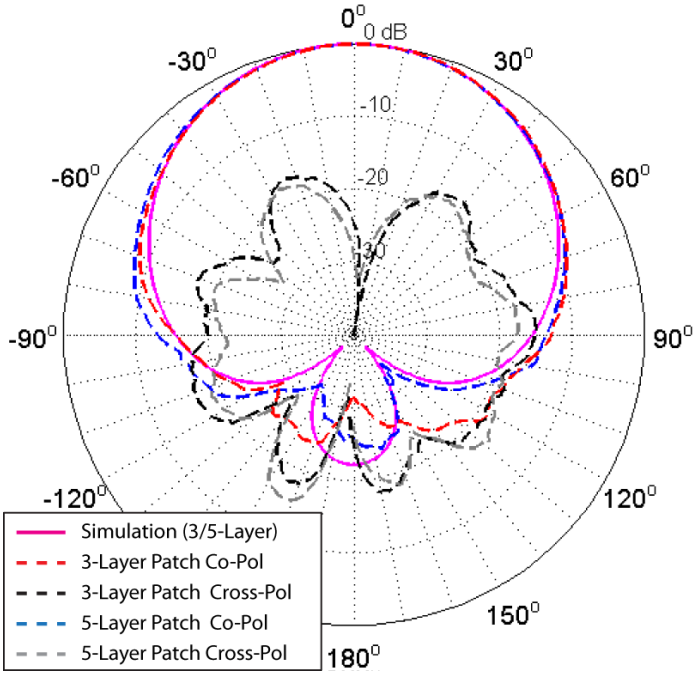

(a)

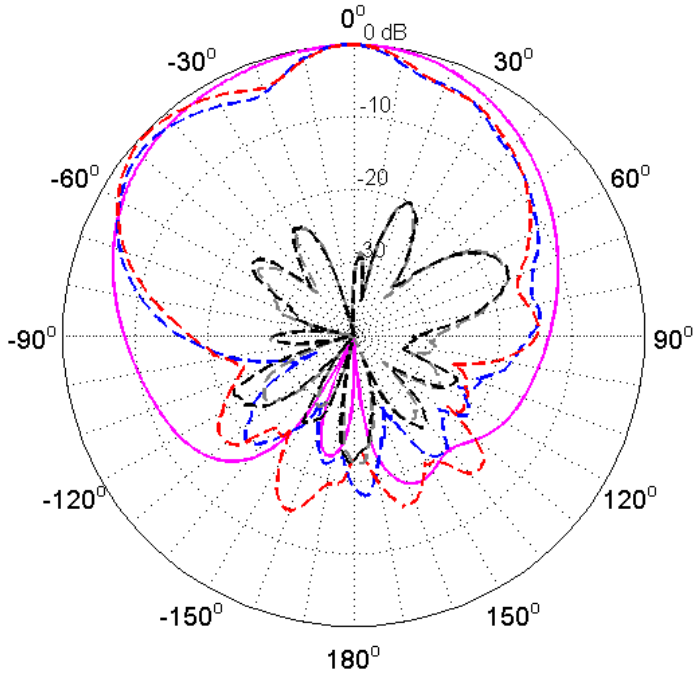

(b)

Figure 86. (a) Simulated and measured normalized H-plane radiation pattern, and (c) simulated and measured normalized E-plane radiation pattern at 24.5 GHz

6.2 Four Element Proximity-Fed Patch Antennas

To demonstrate the reliability of the VIPRE printing process, a much more fabrication-complex four-element proximity-fed patch array is designed for the 24.5 GHz band. The proximity coupled array shown in Fig. 87 is an arrayed version of the proximity-fed patch in the previous section. The patch array dimensions are optimized in the CST frequency domain solver for a 50 ohm input impedance and maximum broadside gain at 24.5 GHz. A thicker 60 um SU-8 layer is used for the arrays to demonstrate the ease and versatility of changing layer thicknesses on-the-fly with inkjet printing, which in this case only requires four extra passes of the printer. The optimized simulation results yield a center-to-center element spacing of 0.51λ in the horizontal direction and 0.6λ in the vertical direction, and a patch size of 3.5 mm by 4.4 mm. The patch size is slightly larger than that of the single element patch due to the thicker printed dielectric, and mutual coupling between the elements.

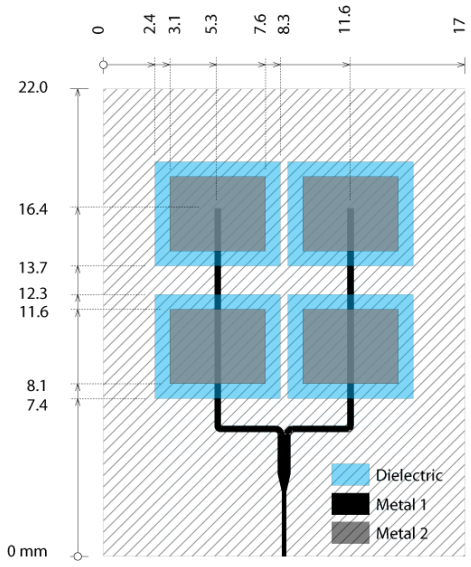

Figure 87. Design of proximity-fed patch antenna arrays

6.2.1 Proximity-Fed Patch Antenna Array Process Flow

The process flow for printing the mm-Wave proximity-fed patch antenna arrays using the VIPRE process is the same as that used for the single element patch antennas except for

the addition of four extra layers of SU-8 dielectric.

6.2.2 Proximity-Fed Patch Antenna Array Results

An optical micrograph of the fabricated patch antenna array prototype is shown in Fig. 88.

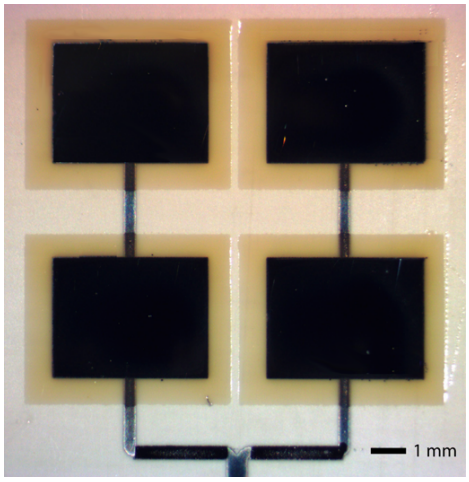

Figure 88. Optical micrograph of the proximity-fed patch antenna arrays

The post fabrication measurements show the printed dielectric spacer to be 64 um thick, which is 4 um thicker than the initial specification, and the patch size to be 3.52 mm by 4.5 mm which is very close to the specified dimensions in the layout. Return loss measurements are performed on two arrays from the batch and compared to the post-fabrication simulation in Fig. 89. While the array is a much more complex structure to fabricate, it can be seen that the return loss between fabricated arrays is nearly identical and well-matched to 50 ohms at 24.75 GHz. The frequency at which the antenna is well-matched is higher than the initial simulation due to small fabrication variations, but matches well with post-fabrication simulations.

Following the return loss measurements, the realized gain versus frequency and radiation patterns of the two arrays are measured and compared with simulation. In Fig. 90, it is shown that both arrays have a very similar broadside gain versus frequency with peak gains of 6 dBi. The measured E and H-plane radiation pattern cuts shown in Figs. 91(b) and 91(a) respectively show a strong agreement between both fabricated arrays, and the

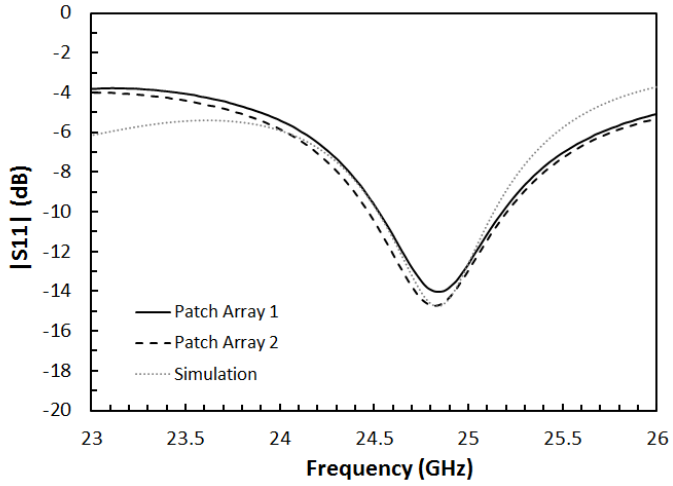

Figure 89. Return loss measurement of the proximity-fed patch antenna arrays

simulation. Again, there is a slight disagreement between measurement and simulation in the E-plane cut due to the lack of connector and cable radiation in the simulation.

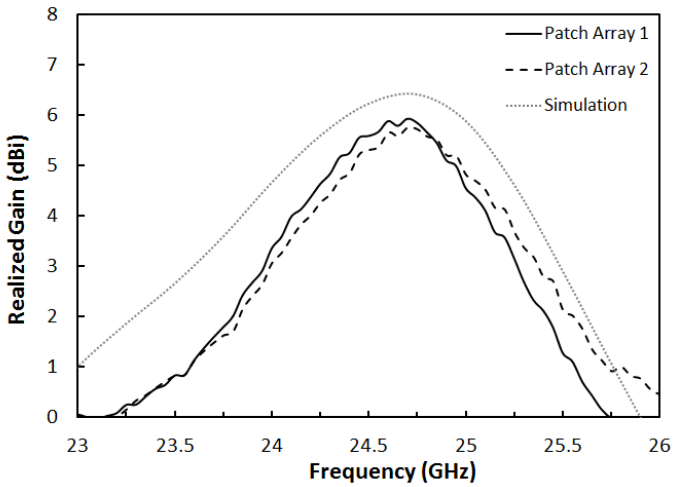

Figure 90. Simulated and measured broadside realized gain versus frequency of the proximity-fed patch antenna arrays

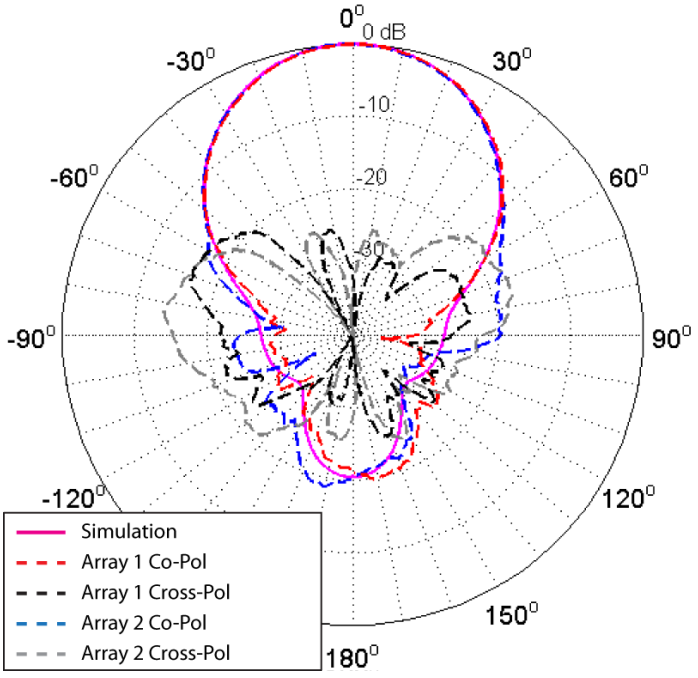

(a)

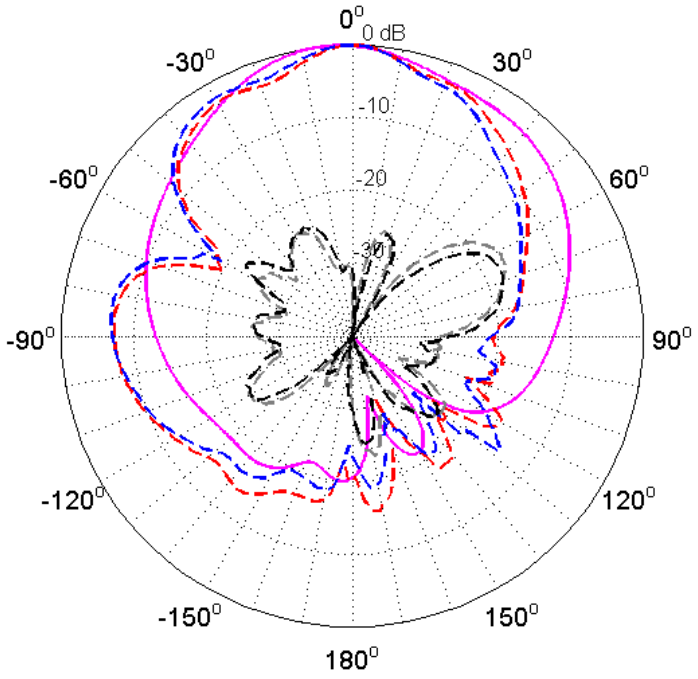

(b)

Figure 91. (a) Simulated and measured normalized H-plane radiation pattern, and (c) simulated and measured normalized E-plane radiation pattern at 24.5 GHz for the patch antenna arrays

6.3 Conclusions

The results of the proximity coupled patch confirm that inkjet printing is a viable and repeatable technology for processing mm-Wave passive structures on-wafer and on-package that can potentially simplify the packaging process in a drastic way.

Utilizing the VIPRE process, high gain mm-Wave antennas and antenna arrays which conventionally required complex fabrication methods and multi-layer boards are rapidly and cheaply fabricated onto virtually any substrate with gains as high as 7 dBi. The resulting repeatability within 1% of the printing process shows a great promise in paving the road to on-package and on-chip printed antennas for inter/intra-chip communications to greatly simplify the currently complex antenna-on-package and chip-scale package based design and fabrication techniques. While operation frequencies of 24.5 GHz are demonstrated in this work for the first time for multi-layer antennas topologies of enhanced complexity, the results show the potential of inkjet-printing for printing structures at even higher frequencies. Future work in adding layers to the process stack-up, and optimizing printed materials for higher frequencies will greatly enhance design and manufacturing capabilities and allow for smaller, cheaper, and conformally integrated mm-Wave and sub-THz wireless systems.

CHAPTER 7

VERTICALLY-INTEGRATED INKJET RF MICROFLUIDICS

Microfluidics have become a valuable tool over the past decade to manipulate, analyze, and interact with tiny amounts of liquid in applications ranging from blood analysis, bio-assays, and manufacturing quality control. Before microfluidics, processes such as bio-assays and water quality analysis required large amounts of liquid ranging from milliliters to several liters, the majority of which is wasted in dead volume required to fill tubing and valves, and never utilized for analysis or measurement purposes. However, with the introduction of microfluidic systems, fluid analysis can be performed on samples on the order of microliters due to the monolithic integration of sensing and interface electronics, fluidic manipulation structures, and micron sized fluid channels on a single packaged chip. Microfluidic devices are typically fabricated utilizing cleanroom processing as standard lithographic processes lend well to producing micron sized encapsulated fluid channels as well as the required interface electronics. These processes, however, are time consuming, costly, and require the use of harsh chemicals. Because of these issues, extensive research has gone into alternate fabrication methods that allow for simple, low-cost, and rapid production of microfluidic devices. Several methods, such as laser etched fluidics, craft cut fluidics, and wax impregnated capillary action fluidics on paper, have emerged that can be produced outside of a cleanroom environment in a simple manner [121–123]. However, one of the obstacles with current low-cost microfluidics is integrating electronics while keeping the devices low cost, as patterning interface and sensing microelectronics onto the chip still requires the use of standard cleanroom processes. In this chapter, a novel approach is proposed that allows for the fabrication and monolithic integration of low-cost microfluidic channels with RF interface microelectronics by utilizing the VIPRE process. With the VIPRE process, interface electronics and printed adhesive layers are deposited onto a base substrate that can be bonded with laser etched fluid channels to produce fully integrated RF microfluidic sensing

systems [124]. The components demonstrated in this chapter include tunable microfluidic RF capacitors, resonators, and the first ever wireless passive lab on chip. The proposed "zero power" inkjet-printed microfluidic sensing platform can be targeted towards large-scale distributed water quality measurement, process monitoring, and biomedical analysis due to its low-cost nature.

7.1 RF Microfluidics Theory of Operation

At microwave frequencies, fluids exhibit large differences in their electrical parameters, such as permittivity (ϵ_r), conductivity (σ), and loss ($tan\delta$), some of which are displayed in Table 13. Due to the large variability in the constitutive parameters of different fluids at high frequency, the introduction of different fluids into a microwave system can cause drastic changes in the system properties based on field interactions with the fluid.

Table 13. Electrical parameters at 900 MHz and 300 K [125, 126]

Fluid	**Re(Permittivity)** $\epsilon^{'}$	**Im(Permittivity)** $\epsilon^{''}$
Water	73	5
Ethanol	15	11
Hexanol	3	2.5

This idea has recently led to the introduction of fluid-tunable microwave systems, and the similar reciprocal, fluid sensing utilizing microwave systems. The majority of the current fluid integrated microwave systems in the literature utilize the fluid as a replaceable dielectric for transmission lines, microwave resonators, or antennas [127–136]. By introducing fluids with different constitutive parameters as the dielectric, the propagation constant on transmission lines, or the resonance of a resonator or antenna can be changed. However, the majority of these systems utilize complex fabrication techniques, or utilize large-scale fluidics.

In this paper, we demonstrate tunable microfluidic resonators and antennas that operate based on a microfluidic loaded capacitive gap that acts as the tuning mechanism. The

capacitive gap is an area of high electric field concentration. As the field concentration is high in this region, introducing very small amounts of fluid allows for large changes in the impedance of the gap. These changes are dependent on the constitutive parameters of the fluid, or mixture of fluids that flow through the gap, which makes the gap a fluid dependent varactor. This fluid-dependent varactor can then be used to load microwave resonators and antennas to tune their frequency of operation.

7.2 RF Microfluidics Process Flow

The materials used are 1/16 inch thick cast acrylic sheets (Poly(methyl-methacrylate)) (PMMA) (Mcmaster-Carr, Atlanta, GA) into which the microfluidic cavities and channels are etched; 220 μm thick Kodak Premium Photo Paper, which is used as the bonding substrate (Office Depot); and Circuit Works 60 Minute Cure Conductive Epoxy (Chemtronix, Kennesaw, GA) for attaching RF connectors and RFID chips. The process for constructing the varactors, and all structures that utilize the varactor, is as follows. The PMMA sheets are etched with channels and cavities for storing and moving the fluid-under-test, using an Epilog Mini 40 W infrared laser. The patterned metallization is then printed onto the photo paper cured at 120°C for one hour. Three layers of the SU-8 ink are then printed on top of the metallization to form the bonding layer for which bonds the paper substrate and the etched PMMA substrate. The photo paper and PMMA sheets are then bonded together on a hot plate at 80°C and with 10 N/cm^2 of pressure. A diagram of this process can be seen in Fig. 92.

7.2.1 Etching of Cavities and Channels

The fluid inlet/outlets, which allow a fluid-under-test to pass into and out of the system, the microfluidic cavities, which hold the fluid-under-test atop the varactors, and the microfluidic channels, which transport the fluid-under-test between the cavities and the fluid inlets/outlets, are etched in a 1.5mm thick PMMA sheet via laser etching. The etching is performed using an Epilog Mini 24 etching system utilizing a 650 nm wavelength 40 W

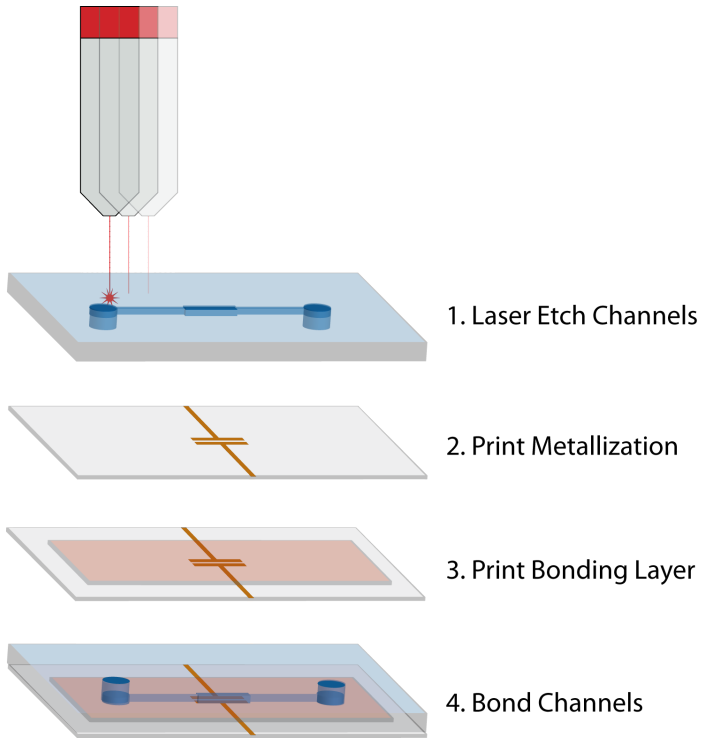

Figure 92. Inkjet microfluidics process overview

Laser. The laser runs under two modes, raster and vector. Raster mode is used to create the cavities, as it allows for large area engraving, and vector mode is used to etch the channels and to cut-out the fluid inlets/outlets as it allows for finer features. Etching is performed with the PMMA at the focal point of the laser when fine features and sharp edges are desired, and run with the PMMA 5 mm below the focal point of the laser when smooth features and rounded edges are desired.

Parametric sweeps are run in order to create an etching profile for the cavities and channels. First, a sweep is done in the raster mode for the cavities, where the power is swept from 15% to 45%, in increments of 5%, while the laser is in focus and again while out of focus. The speed is kept constant at 10% maximum speed for the laser, and the laser pulsing frequency is kept constant at 5 kHz. The extracted depths of the cavity etches for different power levels, in focus and out of focus, can be seen in Fig. 93(a) and 93(b) respectively. Cross sectional profiles of the cavity etches created by the parametric sweep, for both in focus and out of focus, can be seen in Fig. 94. The width of the cavity etches

remains nearly constant under the different power levels, at 1.04 mm for in focus etching, and 1.12 mm for out of focus etching. In order to make the cavities such that they contain less than 25 μL, or about 1/2 a drop of water, a power level setting of 14 W, while the laser is out of focus, was chosen.

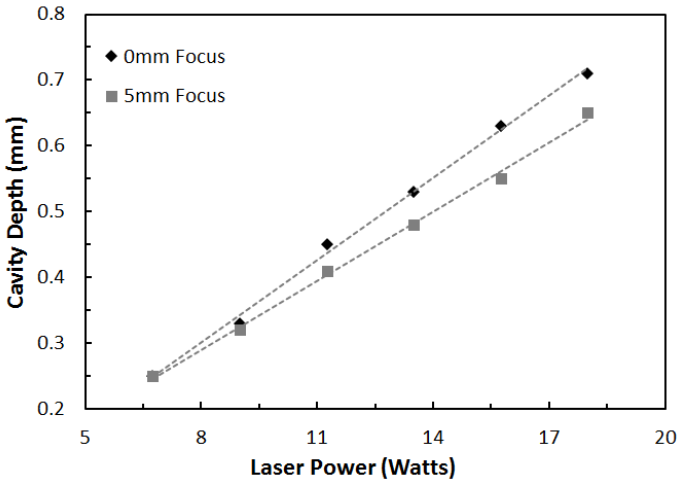

(a)

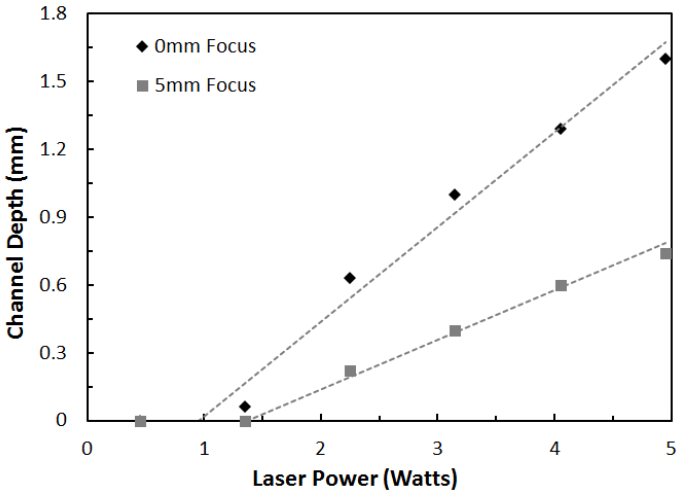

(b)

Figure 93. (a) Channel depth versus laser power for in and out of focus settings and (b) cavity depth versus laser power for in and out of focus settings

Following cavity etching, a sweep is done in the vector mode to determine the etching profile for the channels, where power is swept from 3% to 11% in increments of 2%, while in focus and out of focus. The speed is kept constant at 7% of maximum speed for the

laser, and the laser pulsing frequency is kept constant at 5kHz. The extracted depths of the channel etches at different power levels, in focus and out of focus, can be seen in Fig. 93. Cross sectional profiles of the channel etches under the sweep, for both in focus and out of focus, can be seen in Fig. 94. The width of the channels under the in-focus sweep remains constant under variation in power, at 100 μm. The widths of the channels when the PMMA is 5 mm below the focal point vary depending on the power level from 250 to 375 μm. The sharp edges of the in-focus channel etchings can exacerbate micro fracturing which occurs during heating of the PMMA. Also, the narrow profile of the in-focus etching can make the channels more susceptible to clogging by the SU8 applied in the bonding phase. Therefore, an out-of-focus etching profile is used for the rest of this work. A power level of 2.25 W was chosen for the etching of the channels on the varactor in order to guarantee easy flow of the fluid-under-test as well as minimizing the total fluid volume in the channels to sub-microliter volumes.

The laser etcher is also used to cut out the final microfluidic chip. This includes the fluid inlets/outlets for connecting feed tubing, and any cutout which might be necessary for placing RF connectors or surface mount devices. This was done using 8 W at a 7% speed while the laser is in-focus.

7.2.2 Bonding and Curing

For bonding the PMMA to the paper substrate, after printing the SU8, the paper substrate is placed in a low energy UV oven in order to activate the SU-8 crosslinker. A total exposure of 100 mJ/mm^2 at 365 nm is used. Once the crosslinker is activated, the PMMA and paper substrate are bonded at a constant pressure of 10.5 N/cm^2 while the structure is slowly raised to 100°C to complete the bonding. The continued pressure serves to keep the two surfaces in contact, to prevent the PMMA from warping, and to remove any air bubbles that may degrade the integrity of the bond. A cross-sectional view of a channel after the bonding process can be seen in Fig. 95, along with a top down view of the channel filled with liquid. From the image, it can be seen that very little of the SU8 is sucked into the

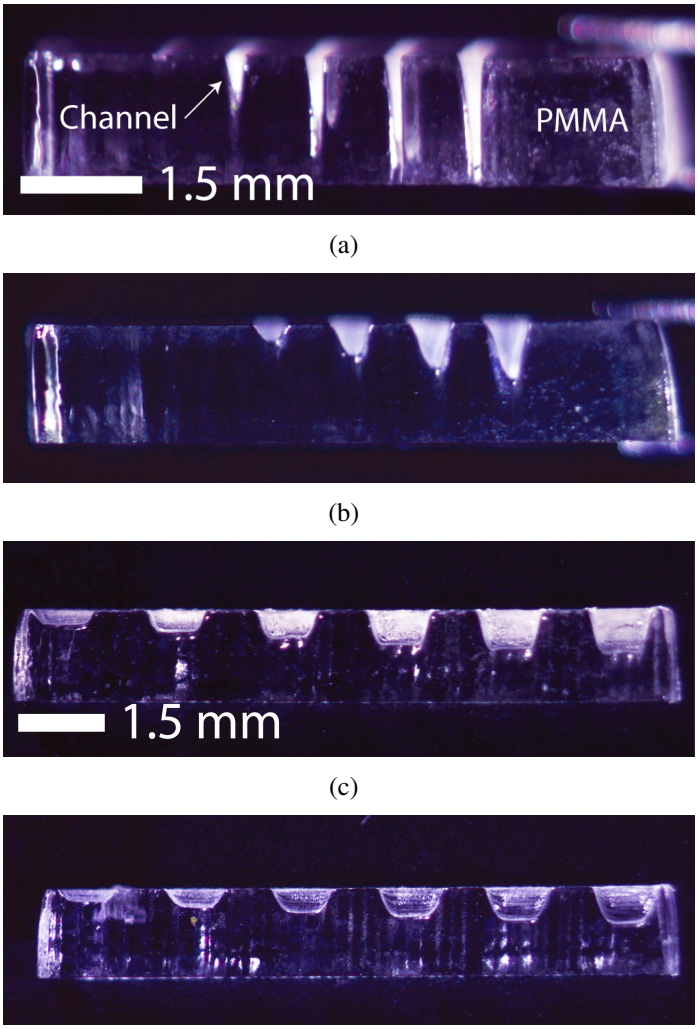

Figure 94. (a) In focus vector cut channels, (b) 5 mm out of focus vector cut channels, (c) in focus raster cut cavities, and (d) 5 mm out of focus raster cut channels

channels, thereby not altering the volume and cross-sectional areas.

7.2.3 Post Bonding Processing

After bonding, a tubing is connected to the fluid inlets/outlets in order to move fluid into and out of the measurement system. The tubing is secured to the fluid inlets/outlets using a super glue, which partially melts the PMMA and forms a solid seal. Any RF connectors or surface mount components are attached to the metallization using conductive epoxy. The epoxy is cured in an oven at 80°C for 20 min in order to avoid warping of the PMMA.

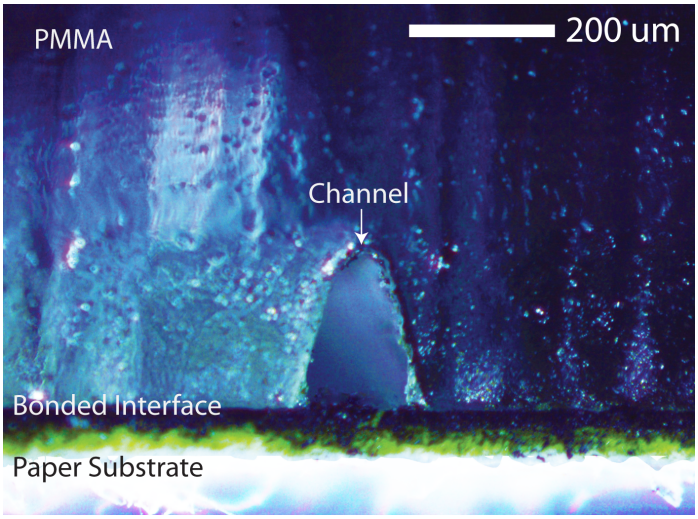

(a)

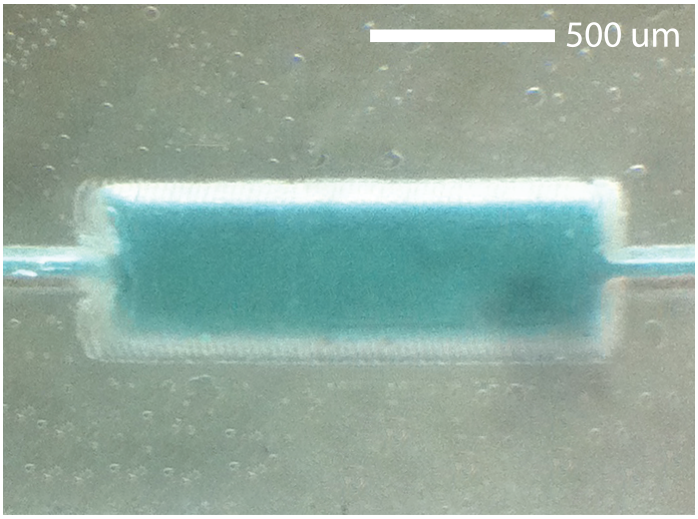

(b)

Figure 95. (a) Laser-cut cross section of PMMA with etched channel bonded to paper substrate, and (b) top-down view of a PMMA-etched microfluidic cavity bonded onto paper filled with fluid

7.2.4 Stability and Fluid Compatibility

The fluid compatibility of the bonded microfluidic channels is dependent on the two materials that construct the channel - etched PMMA, and an SU-8 seal. After curing, SU-8 has a very high chemical resistance. PMMA is resistant to most polar solvents, but is not compatible with most non-polar solvents. Other materials can be used in the future such as PDMS.

The temperature stability of the microfluidic devices is limited by the glass transition

temperature of the PMMA which is 105°C.

7.3 Microfluidic Varactor

The fundamental building block of the tunable microwave resonators and antennas in this work is the microfluidic varactor shown in Fig. 96. The varactor consists of a planar capacitive structure with a 500 μm gap that is fed using microstrip feed lines. A 500 μm deep fluid cavity etched in PMMA is bonded directly over the gap to allow for delivery of the fluid. The entire device is fabricated using the process outlined in Section III.

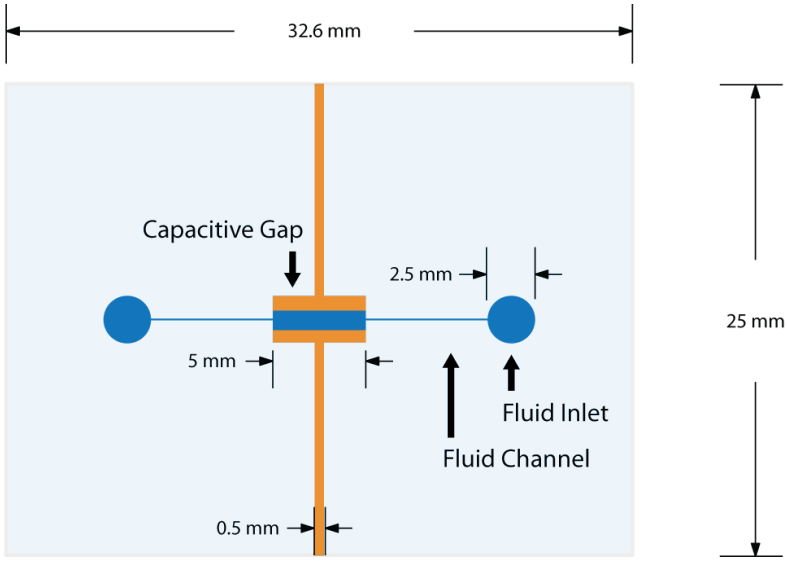

(a)

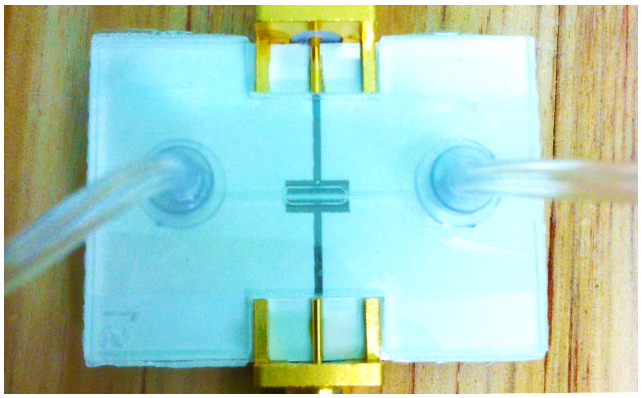

(b)

Figure 96. (a) Scale-drawn schematic of fabricated microfluidic varactor, and (b) fabricated microfluidic varactor with mounted SMA connectors for performing microwave capacitance measurements

To simplify the simulation of tunable devices in the following sections that utilize the microfluidic varactor as a fundamental building block, the ability to model the varactor as a lumped element in the system would be ideal and greatly decrease simulation time. The electrical properties of the materials are $\epsilon_{r(paper)}$ = 3.1, and $tan_{\delta(paper)}$ = 0.06 [24], $\epsilon_{r(SU8)}$ = 3.0, and $tan_{\delta(SU8)}$ = 0.04 [96], and $\epsilon_{r(PMMA)}$ = 3.5, and $tan_{\delta(PMMA)}$ = 0.04 [137]. In order to create the lumped model, TRL calibration structures are fabricated to de-embed the microstrip feeds, and the S-parameters of the gap are measured from 0 - 8 GHz using a Rhode and Schwartz ZVA-8 VNA. The varactor is loaded with ethanol, hexanol, water, and various combinations of the three to produce a fluid and frequency-dependent model. The net permittivity of the mixtures is determined by the Looyenga formula, which assumes linear mixing and no chemical reactions [138].

De-embedding of the connectors and feed lines is performed using WinCal to move the reference plane up to the outer edge of the capacitive pads. The series capacitance of the gap is then extracted directly from the de-embedded S-Parameters. Fig. 97 displays the frequency dependent capacitance and quality factor of the varactor for various fluids in the cavity. When fluid is introduced, it is noticed that the capacitance decreases over frequency. This is due to the high dispersion present in the fluids used in this study, which exhibit a large decrease in permittivity near 1 GHz [125, 126]. The capacitance when the fluid cavity is empty is approximately 0.05 pF and is stable until the self-resonant frequency (SRF) is reached near 7 GHz. Introducing 1-hexanol, ethanol, and water, which each have increasingly higher permittivities, incrementally increase the capacitance of the gap from 0.05 pF to 1.25 pF at 900 MHz, which is approximately a 2500% increase. The large changes in capacitance will allow for wide tuning ranges in microwave components and sensors, which are demonstrated in the following sections. The SRF, however, decreases from 7 GHz to approximately 4 GHz as the capacitance increases, meaning tunable components must be operated under 4 GHz to avoid the unwanted effects of utilizing the gap above its SRF.

To test the sensitivity of the gap, a study is performed in which varying amounts of water

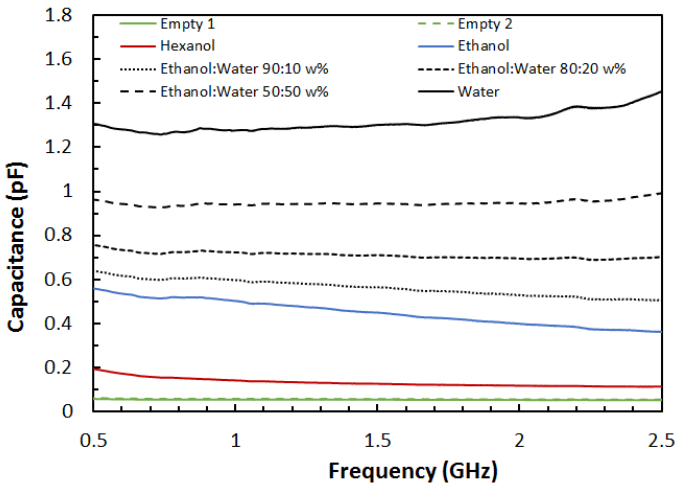

Figure 97. De-embedded frequency dependent capacitance of the microfluidic varactor for different fluids

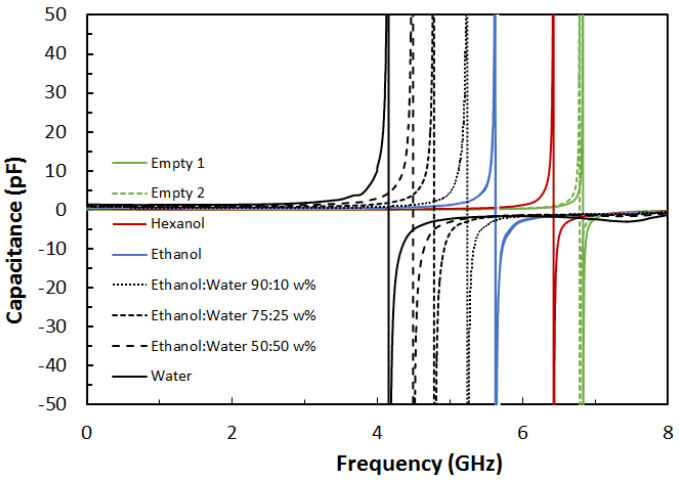

Figure 98. De-embedded self-resonant frequency of the microfluidic varactor for different fluids

are added to a 100% ethanol solution in 1, 3, 10, and 25 w% concentrations. Very distinct capacitance increases can be seen with even 1% by weight additions of water in ethanol, which can be attributed to the net increase in permittivity of the solution. For 1 w% water in ethanol, the impedance changes nearly 4%, and for 3 w% water in ethanol, the impedance changes 8.2% at 900 MHz. While these changes may seem small for standard R-C rise time measurements, they are not trivial when used for tuning of microwave components, as small impedance changes can translate into large resonant frequency shifts.

The capacitance at 900 MHz versus the net permittivity of the solution is compared

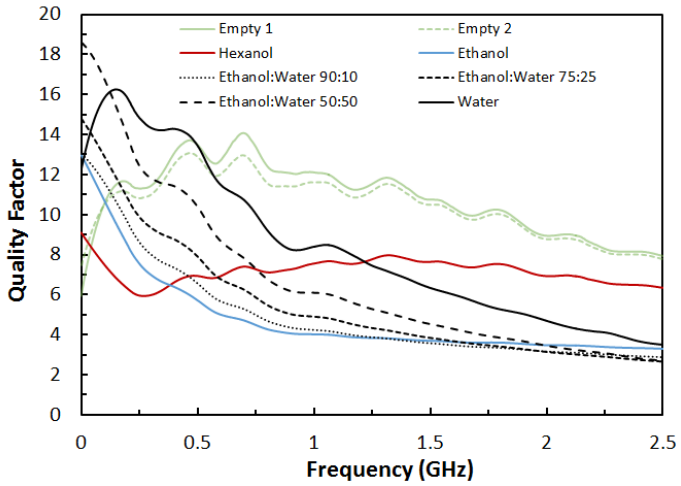

Figure 99. De-embedded varactor quality factor

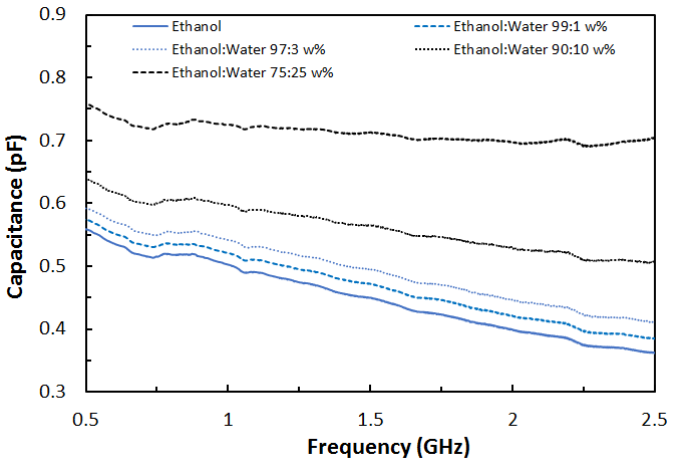

Figure 100. De-embedded capacitance of the microfluidic varactor for various concentrations of water in ethanol

with simulation in Fig. 101. A very good agreement is obtained in both the capacitance value and trend as the fluid permittivity increases, and as fluids are mixed.

7.3.1 Microfluidic Varactor Conclusions

The high sensitivity in capacitance of 17.5 pF/ϵ_r and linearity versus permittivity demonstrated by the varactor lends itself well to tuning and sensing applications. State of the art works show capacitance sensitivities of approximately 12 pF/ϵ_r [139, 140].

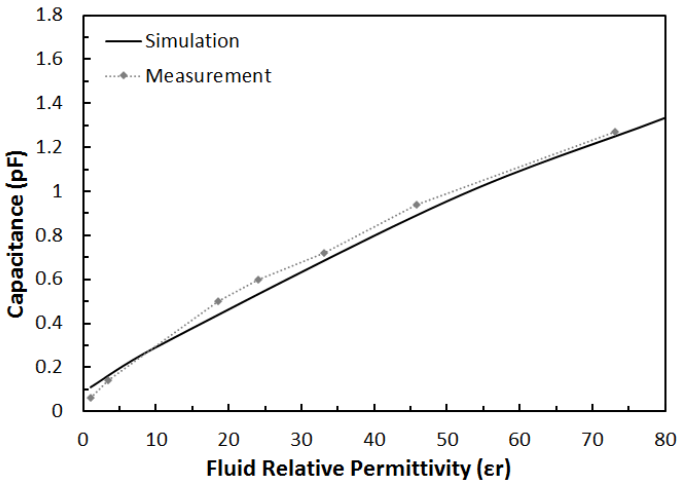

Figure 101. Measured and simulated linearity of the varactor

7.4 Microfluidic Resonator

Varactors are a common component used in the tuning of microwave devices, such as resonant tanks, filters, and voltage controlled oscillators. In this section, the varactor demonstrated previously is used to tune the resonant frequency of a microstrip T-resonator by changing its electrical length.

The microstrip T-resonator used in this work is shown in Fig. 102. The resonator is designed for a 2.4 GHz center frequency of operation to keep the size small, and to demonstrate that the varactor model created in the previous section is valid through the 2.4 GHz band.

The microstrip T-Resonator is a length of transmission line with an open circuit stub. The resonator has a null in the insertion loss when the reflected wave from the stub is 180° out of phase, or when the length of the open circuit stub is approximately $\frac{\lambda}{4}$. The equation for resonance is shown in (21) where n is the resonance mode i.e. (n = 1, 3, 5, ...), c is the speed of light in free space, L is the length of the open circuit stub, L_0 is the correction factor for the fringing capacitance at the end of the stub, and ϵ_{eff} is the effective permittivity of the microstrip line [141].

By inserting the varactor in series with the open circuit stub, the effective length of

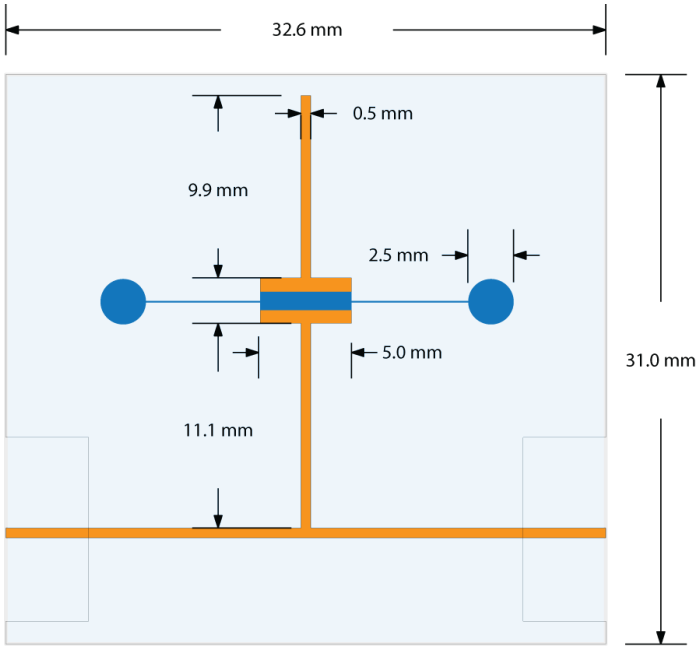

(a)

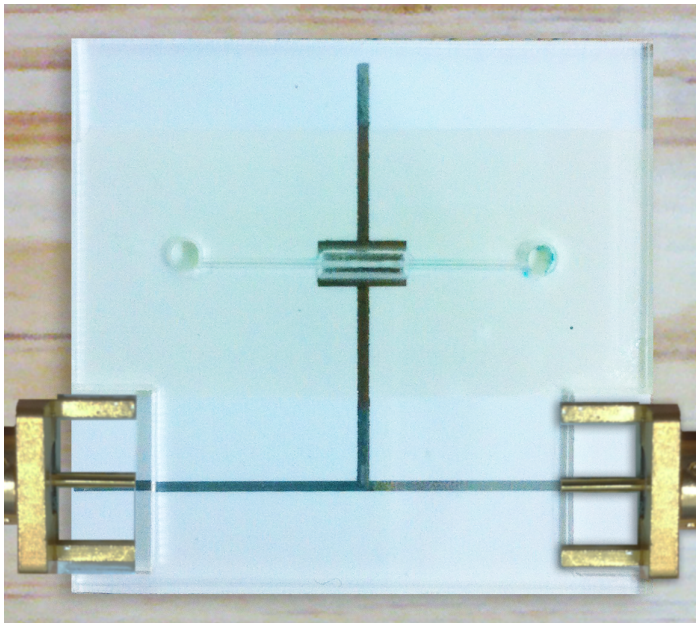

(b)

Figure 102. (a) Scale-drawn schematic of the fabricated microstrip T-resonator with embedded varactor, and (b) fabricated microfluidic tunable microstrip T-resonator

the stub is changed upon introduction of different fluids. With no fluid in the gap, the capacitance is 0.05 pF, or $-j8 \times 10^3$ ohms, which is essentially an open circuit at 2.4 GHz. However, when water flows through the gap, the capacitance increases to 1.5 pF, or

$-j2.5 \times 10^2$ ohms, at 2.4 GHz; the impedance decreases making the varactor appear closer to an RF short than an RF open. As the reactance of the gap decreases, the effective length of the open circuit stub increases, which effectively decreases the resonant frequency of the resonator.

The T-resonator is constructed as in Fig. 102. For simulation, a discrete impedance model is used to replace the gap which helps reduce the simulation time. The series gap impedance for each fluid is extracted from the de-embedded capacitive gap in the previous section for use in the simulation.

Fig. 103(a) displays the measured insertion loss of the resonator for various fluids. With an empty cavity, there is a resonance at 2.4 GHz. By introducing the various fluids used previously for the varactor, the resonator is tuned down to 1.8 GHz. The sensitivity in resonant frequency is approximately 0.35 $\%/\epsilon_r$. This is comparable to the tunability of state-of-the art fluid-based resonators and frequency selective surfaces which achieve sensitivities of 0.25 $\%/\epsilon_r$ [132]and 0.05 $\%/\epsilon_r$ [136] respectively. The quality factor is lower with fluids such as ethanol as the dielectric loss is high, however, this can be easily improved by utilizing different fluids, as can be seen with deionized water.

7.5 Passive Wireless Lab-on-Chip

Moving away from wired microwave components, an area of potential high impact that can be enabled by the fluid varactor is wireless microfluidic-based lab-on-chip (LOC). Wireless LOC systems allow for the remote analysis of fluids in biomedical, production, and potentially hazardous environments where wired measurements are not feasible or cost effective. Currently, however, wireless LOC systems require a power source that increases cost and decreases life span.

By utilizing the microfluidic varactor to tune an RFID antenna utilizing a similar method to the T-Resonator, a completely passive RFID-based lab on chip platform is demonstrated for the first time. The design for the microfluidic RFID antenna is shown in Fig. 104, which

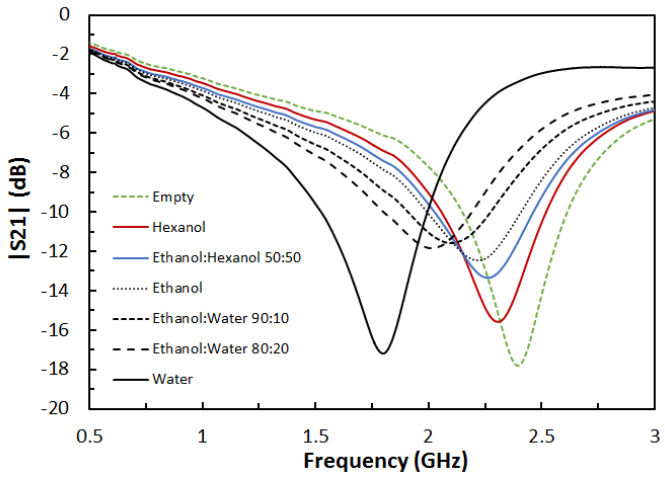

(a)

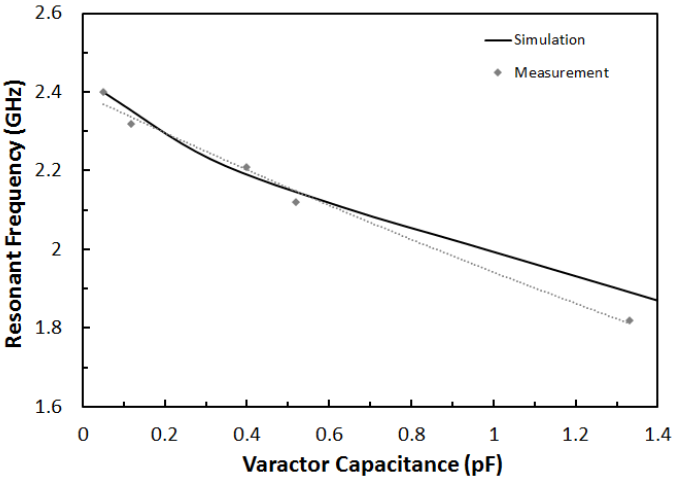

(b)

Figure 103. (a) Insertion loss of the microfluidic T-resonator with different fluids, and (b) simulated and measured response of the T-resonator using the discrete capacitance model of the microfluidic varactor

consists of a meandered dipole antenna, fluid varactors to change the electrical length of the antenna, and a T-matching network for the RFID chip which will be used for communication. The microfluidic RFID antenna is designed to match the impedance of the Alien Technologies Higgs 3 EPC Gen-2 RFID chip, which is approximately 16+j200 ohms. As the readable range of the Voyantic Tagformance reader is 800-1000 MHz, the antenna is designed to resonate near 1000 MHz when empty so that the downward shifts caused by the introduction of fluid can be captured. The design is optimized for these parameters

using the CST frequency domain solver. The same gap model extracted from the varactor is utilized to simulate the expected resonant shifts in the antenna.

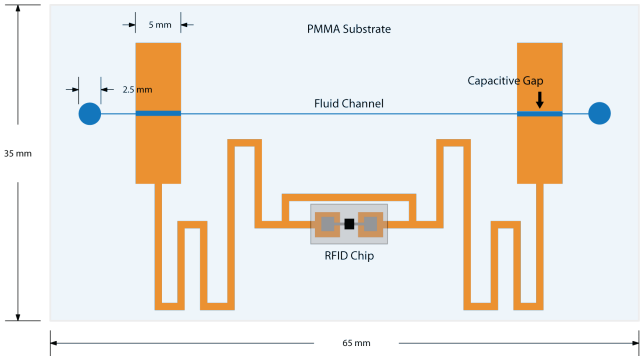

(a)

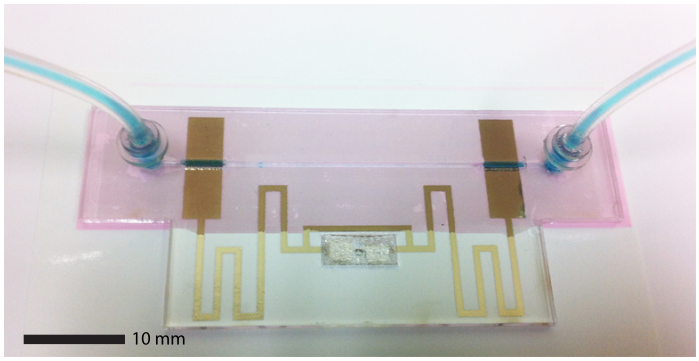

(b)

Figure 104. (a) Scale-drawn RFID-based microfluidic sensor, and (b) fabricated RFID-based microfluidic sensor demonstrating fluid flow

To confirm the agreement of the fabricated tag with the simulation before wireless backscatter measurements are performed, a cabled measurement of the return loss of the antenna is performed using a Rhode and Schwartz ZVA-8 VNA. The measured S-parameters are then re-normalized to the RFID chip impedance as displayed in Fig 105. The return loss shows matching at 1 GHz when the channel is empty, which is confirmed in simulation. The various fluids utilized in the previous sections are then pumped through the fluidic channels while the return loss is measured. Distinct downward shifts in the resonance confirm that the fluidic channel is loading the capacitive gap on the antenna and increasing the electrical length. Large shifts of nearly 100 MHz are achieved in the cabled measurement.

The shifts experienced in the cabled measurement are compared with simulation utilizing the gap model in Fig. 109 and the best fit curves show a difference below 6%.

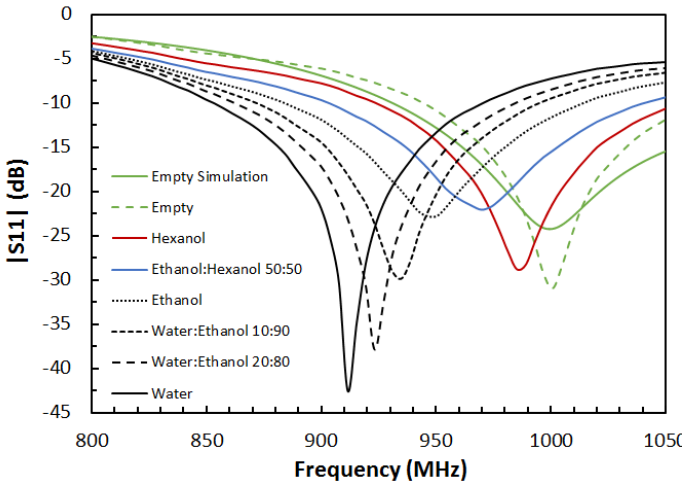

Figure 105. Measured S-parameters of the microfluidic RFID tag

Following cabled verification of the passive microfluidic tag, the Alien RFID chip is mounted on the tag and a wireless measurement setup is constructed as displayed in Fig. 106. The tag is placed 0.5 m away from the reader antenna of the Tagformance, which interrogates the tag across the 800 to 1000 MHz band. The interrogation distance was fixed by the setup available in the anechoic chamber. The Tagformance returns data on power required to activate the tag, and the reflected power and phase versus frequency. A single frequency sweep takes approximately 10 seconds. This can be decreased by lowering the frequency resolution.

Again, the tag is measured with an empty channel, and all of the fluids used in the cabled measurement. The data returned from the Tagformance which is shown in Fig. 107 displays the transmit power required to activate the tag versus frequency along with the second order curve fit in Matlab which is used to extract the resonant frequency. A clear downward shift in the resonant frequency is experienced as higher permittivity fluids are sent through the channel as is expected, and the resonant shift versus fluid permittivity is plotted in Fig. 109, against simulation and cabled measurement. After all of the liquid measurements are

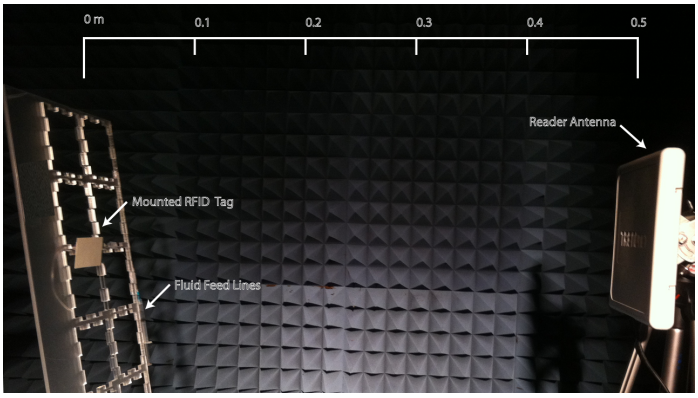

Figure 106. Measurement setup of the wireless lab-on-chip RFID tag

performed, the tag is emptied and again measured. The extracted resonant frequency of the empty tag is within a fraction of a percent of the empty measurement before being filled with an array of fluids. This demonstrates a high degree of repeatability which is important in long-term monitoring situations. It is noticed that the activation power slightly decreases with the higher permittivity fluids which is due to the improving matching between the antenna and chip impedance. The T-match is designed so that optimal matching occurs when the antenna resonant frequency is 900 MHz. It is seen from Fig. 109 that the wireless tag exhibits lower shifts than the cabled measurement, and this is due to the variation in chip impedance over frequency which is not taken into account in the simulation or cabled measurement. The variation in chip impedance along with the T-match cause a decreased sensitivity.

To test the effects of the chip impedance versus frequency on the sensitivity of the wireless lab-on-chip, a second version of the tag is fabricated in which the center frequency of tag antenna is tuned to 900 MHz by slightly increasing the length of the antenna. The Higgs 3 RFID chip typically has its own internal resonance around 900 MHz as well which will overshadow some of the effects of the change in the electrical length of the antenna. By repeating the same procedure for wireless measurements with the previous tag, the curve-fit data of backscatter versus fluid flow is shown in Fig. 108. The resulting sensitivity is even lower than previous tag as the chip resonance begins to overshadow the electrical length

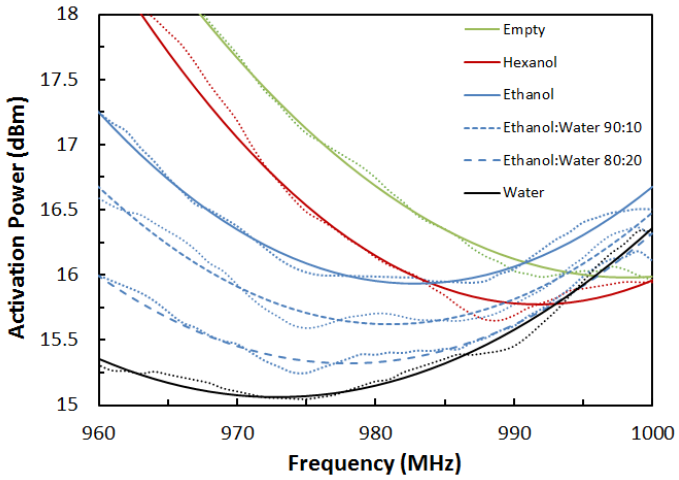

Figure 107. Curve fit backscatter data of a microfluidic tag with resonant frequency of 1 GHz

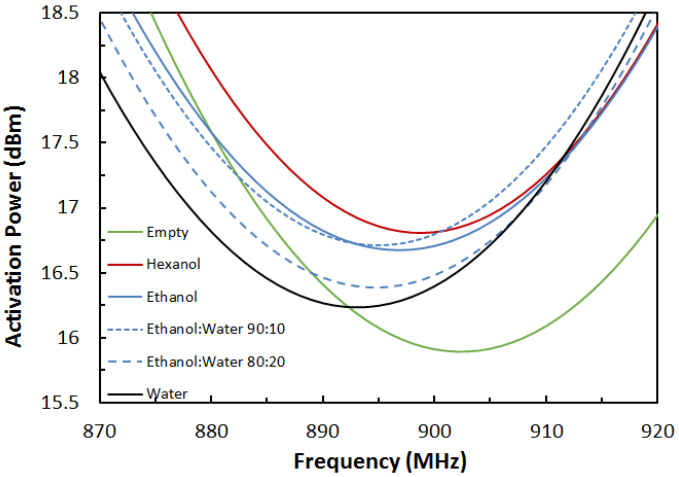

Figure 108. Curve fit backscatter data of a microfluidic tag with resonant frequency of 900 MHz

change of the antenna.

7.6 Vertically-Integrated Inkjet RF Microfluidics Conclusions

Utilizing the VIPRE process, varactors, tunable resonators, and completely passive wireless lab on chip systems have been demonstrated. The microfluidic sensing platform shows highly repeatable results with sensitivities high enough to detect as little as 1% water in ethanol while using under 3 μL of fluid. The low-cost platform out-performs current

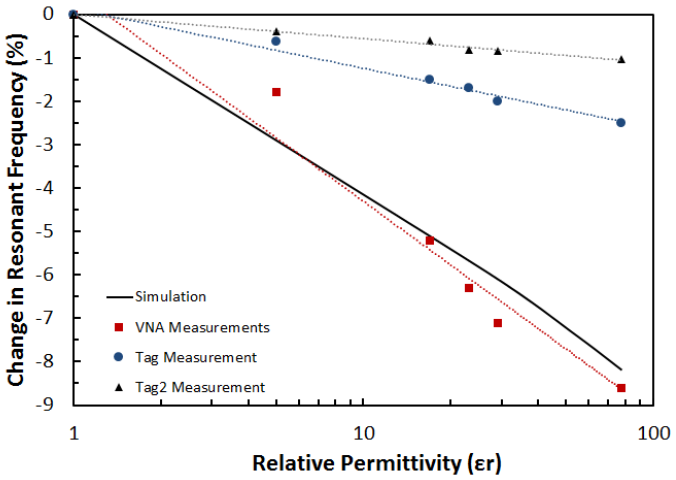

Figure 109. Comparison of simulated and measured return loss of the microfluidic RFID antenna, along with wireless chip measurements

state-of the art RF-integrated microfluidic devices and has applications in lab-on-chip, bio-monitoring, and real time water and chemical analysis and monitoring. .

CHAPTER 8

CONCLUSIONS

The work presented in this dissertation encompasses the creation and characterization of the first vertically-integrated inkjet-printing process for RF electronics (VIPRE). The VIPRE process demonstrated in this work has the ability to deposit high conductivity metals, and thin and thick-layer dielectric inks in a layer-by-layer stack-up that allows for an infinite amount of flexibility for RF designers. Following the creation of the process, its potential in fabricating high frequency 2D/3D structures operating up the mm-Wave frequencies is demonstrated through the fabrication of a wide variety of vertically-integrated RF components which were previously un-realizable with state-of-the art inkjet-printing processes.

The paradigm shift created by the introduction of the VIPRE process of moving from low-cost single-layer devices operating at low frequency to complex vertically-integrated structures operating into the mm-Wave regime opens an entire new realm of possibilities, not only for researchers, but for industrial electronics manufacturers as well. The VIPRE process can be used in high impact applications such as the post-processing/interfacing of interconnects, large area components (e.g. inductors, capacitors, antennas), and sensors on top of ICs which will greatly enhance the flexibility in IC design and compliment current wafer-level packaging techniques. The process can also be used for the creation of more complex, miniaturized, and completely printed modules for low-cost and disposable applications.

8.1 Contributions

The specific contributions of this dissertation are as follows:

1. VIPRE Process Contributions

    (a) Ink Creation and Characterization

i. Silver Nanoparticle Ink: For the first time, a full analysis of printed metallic nanoparticle inks is performed which includes not only physical printing and film characteristics, but also a full material and electrical characteristic analysis for heat and laser sintering of the nanoparticle films.

ii. Copper Catalyst Ink: The first demonstration of a catalyst-based ink for depositing non-noble metals is presented which mitigates issues such as nozzle clogging, and sintering which causes oxidation for non-noble metallic nanoparticle inks. The copper catalyst, while only used for porous substrates at this point, can deposit metallic layers equivalent to those utilizing noble metallic nanoparticles, but at a 15x reduction in cost.

iii. Thick-Layer Dielectric Ink: An inkjet-printed dielectric ink, which can produce layers thicker than 5 um, a thickness which had yet to be achieved, is demonstrated. Utilizing a short-chain SU-8 polymer, layers above 100 um can be easily realized at a deposition rate of 6 - 12 um per pass dependent on drop spacing. A full physical and electrical characterization is performed on the thick-film dielectric.

iv. Thin-Layer Dielectric Ink: An inkjet-printed dielectric ink which can produce layers with thicknesses below 500 nm is demonstrated utilizing a long-chain poly(4-vinylphenol) polymer. For the first time, a PVP ink which can be cured at 130° is demonstrated which is 60° lower than previously demonstrated thin-film dielectrics. A full printed film analysis is performed which shows techniques to better improve the surface roughness of very thin printed layers.

(b) Multi-Layer Deposition Techniques: Previously, ventures into vertically-integrated components using inkjet-printing were hindered by the lack of dielectric inks, and the processing techniques which are required to create MIM stackups including surface energy characterization, surface energy modification rules, and

roughness control techniques. This dissertation not only creates the ink library for conductive and dielectric inks which are required to make vertically-integrated RF structures, but it also characterizes the processing conditions which allow for the efficient fabrication of MIM stack-ups.

(c) Multi-Layer Processing Rule Set: For the first time, a processing rule set has been developed to help designers and manufacturers seamlessly run the VIPRE process to create vertically-integrated fully-printed electronics. The processing rules encompass the entire process from ink creation, to film curing procedures. A fundamental, and turnkey process is crucial to engaging a much larger audience into inkjet-printing.

2. Inkjet-Printed Passives

(a) Inkjet-Printed MIM Capacitors: The first demonstration of fully-printed MIM capacitors which operate into the GHz range is presented in this dissertation. Capacitors which have self-resonances of up to 3 GHz with Q values of up to 8 are presented. The capacitance per unit area of the printed capacitors utilizing the thin-layer dielectric ink is much higher than previously presented works at 52 pF/mm^2. The printed capacitors show a high level of repeatability between fabrication runs with below 5% tolerance on capacitance value and Q.

(b) Inkjet-Printed Spiral Inductors: Spiral inductors, which are a crucial component to typical RF systems, have been demonstrated with Q values up to 22, which is an order of magnitude above previous inkjet-printed planar inductors, and with inductance values of 25 nH which is also an order of magnitude above previous works. The printed inductors show a very high rate of repeatability over multiple fabrication runs speaking to the repeatability of the VIPRE process.

3. Inkjet-Printed mm-Wave Antennas: Proximity fed-patch antennas and antenna arrays which operate in the 24.5 GHz ISM band have been demonstrated which have realized gains of up to 7 dBi. The demonstrated multi-layer antennas are the first demonstration of using a thick-film printed dielectric to replace typical microwave laminates. The printed antennas show excellent repeatability and good simulation/measurement agreement. These antennas can be extended to large-area and conformal applications for radar which cannot be targeted by typical fabrication techniques.

4. Inkjet-Printed Microfluidics Platform: The first low-cost microfluidics platform has been demonstrated which incorporates both microfluidic channels and electronics which does not require cleanroom processing techniques. The RF structures demonstrated with the microfluidics platform, which include varactors, tunable resonators, and a wireless LOC, outperform current state-of-the art RF-integrated microfluidics. The wireless LOC is the first passive, wireless fluid sensing platform to date.

5. Fully-Printed Modules: The VIPRE process is an enabler for the creation of fully-printed modules which were previously not feasible to fabricate using inkjet printing. Components such as multi-layer interconnects, capacitors, inductors, vias, antennas, and sensors can all be integrated utilizing a single printing process. This is an exciting evolution to printing as it introduces the next step towards fully-printed integration of systems which will drastically reduce the cost and increase the functionality of packaging and module fabrication.

8.2 Future Evolution

While the VIPRE 1.0 process is an extremely feature-rich vertically-integrated fabrication process, it is only the beginning of a long chain of process evolution in inkjet printing. Short term revisions to the process will introduce higher conductivity conductive inks, and lower-loss self-organizing dielectric inks which allow for the realization of higher efficiency

RF structures. As printing technology advances, long term evolutions will integrate semiconductive inks which allow for the integration of vertically-integrated passive and active components, and decrease feature sizes to below 1 um - the true fully printed system, and the pinnacle of printing technology.

The VIPRE process is an enabling technology which has allowed for many first-of-a-kind demonstrations in the RF field. However, this technology is only the beginning, and huge strides are in store for the additive manufacturing field in the near future. With hope, the advances made in this work can be utilized by a large audience in the RF, and other fields, to not only create new and novel devices which have a high impact, but to teach and inspire others to advance the field of additive manufacturing.

AUTHOR'S PUBLICATIONS

Book Chapters

1. S. Kim, B. S. Cook, T. Le, A. Traille, and M. M. Tentzeris, *Materials for Substrates, Green RFID Systems*. Cambridge Press, In Press
2. B. S. Cook, B. Tehrani, J. R. Cooper, S. Kim, and M. M. Tentzeris, *Inkjet Printing Technology for 2D/3D Flexible Electronic Systems, Handbook of flexible organic electronics, Materials, Manufacturing and Applications*. Woodhead Publishing, In Press
3. S. Kim, B. S. Cook, J. R. Cooper, and M. M. Tentzeris, *Inkjet-printed Artificial Magnetic Conductor (AMC) Plane for Wearable Antennas, Advancement in Wearable and Flexible Antennas*. WIT Press, In Press

Journals

1. B. S. Cook, "The future of inkjet printed electronics," *Circuit Cellar Magazine*, 2014
2. B. Cook, T. Le, S. Palacios, A. Traille, and M. Tentzeris, "Only skin deep: Inkjet-printed zero-power sensors for large-scale rfid-integrated smart skins," *Microwave Magazine, IEEE*, vol. 14, no. 3, pp. 103–114, 2013
3. B. Cook, J. Cooper, and M. Tentzeris, "An inkjet-printed microfluidic rfid-enabled platform for wireless lab-on-chip applications," *Microwave Theory and Techniques, IEEE Transactions on*, vol. 61, pp. 4714–4723, Dec 2013
4. B. S. Cook, Y. Fang, S. Kim, T. Le, B. Goodwin, K. H. Sandhage, and M. M. Tentzeris, "Inkjet catalyst printing and electroless copper deposition for low-cost patterned microwave passive devices on paper," *Electronic Materials Letters*, vol. In Press, 2013
5. B. S. Cook, B. Tehrani, J. Cooper, and E. Tentzeris, "Multi-layer inkjet printing of

millimeter-wave proximity-fed patch arrays on flexible substrates," *IEEE Antennas and Wireless Propagation Letters*, 2013

6. S. Kim, B. Cook, T. Le, J. Cooper, H. Lee, V. Lakafosis, R. Vyas, R. Moro, M. Bozzi, A. Georgiadis, *et al.*, "Inkjet-printed antennas, sensors and circuits on paper substrate," *IET Microwaves, Antennas & Propagation*, vol. 7, no. 10, pp. 858–868, 2013
7. B. Cook, J. Cooper, and M. Tentzeris, "Multi-layer rf capacitors on flexible substrates utilizing inkjet printed dielectric polymers," *Microwave and Wireless Components Letters, IEEE*, vol. 23, no. 7, pp. 353–355, 2013
8. R. Vyas, B. Cook, Y. Kawahara, and M. Tentzeris, "E-wehp: A batteryless embedded sensor-platform wirelessly powered from ambient digital-tv signals," *Microwave Theory and Techniques, IEEE Transactions on*, vol. 61, pp. 2491–2505, June 2013
9. B. Cook and A. Shamim, "Utilizing wideband amc structures for high-gain inkjet-printed antennas on lossy paper substrate," *Antennas and Wireless Propagation Letters, IEEE*, vol. 12, pp. 76–79, 2013
10. B. Cook, A. Shamim, and M. Tentzeris, "Passive low-cost inkjet-printed smart skin sensor for structural health monitoring," *Microwaves, Antennas Propagation, IET*, vol. 6, pp. 1536–1541, November 2012
11. A. Maza, B. Cook, G. Jabbour, and A. Shamim, "Paper-based inkjet-printed ultra-wideband fractal antennas," *IET Microwaves, Antennas & Propagation*, vol. 6, no. 12, pp. 1366–1373, 2012
12. B. Cook and A. Shamim, "Inkjet printing of novel wideband and high gain antennas on low-cost paper substrate," *Antennas and Propagation, IEEE Transactions on*, vol. 60, no. 9, pp. 4148–4156, 2012

Conferences

1. B. Tehrani, B. S. Cook, J. R. Cooper, and M. M. Tentzeris, "Inkjet printing of a wideband, high gain mm-wave vivaldi antenna on a flexible organic substrate," in *APS/URSI 2014*, 2014

2. B. Tehrani, J. Bito, B. S. Cook, and M. M. Tentzeris, “Fully inkjet-printed multilayer microstrip patch antenna for ku-band applications,” in *APS/URSI 2014*, 2014
3. W. Su, C. Marioti, B. S. Cook, and M. M. Tentzeris, “A novel inkjet-printed microfluidic tunable coplanar patch antenna,” in *APS/URSI 2014*, 2014
4. X. Yi, B. S. Cook, Y. Wang, and M. M. Tentzeris, “Crack propagation measurement using a battery-free slotted patch antenna sensor,” *7th European Workshop on Structural Health Monitoring*, 2014
5. S. Yao, S. V. Georgakopoulos, M. M. Tentzeris, and B. S. Cook, “A novel reconfigurable origami accordion antenna,” *International Microwave Symposium*, pp. 1–3, 2014
6. G. McKerricher, D. Conchouso, B. S. Cook, I. Foulds, and A. Shamim, “Crude oil water-cut sensing with disposable laser ablated and inkjet printed rf microfluidics,” *International Microwave Symposium*, pp. 1–3, 2014
7. J. R. Cooper, B. S. Cook, and M. M. Tentzeris, “The first hardware-based, anti-collision methodology for frequency doubling transceivers for rfid and wireless sensing applications,” *International Microwave Symposium*, pp. 1–3, 2014
8. B. Tehrani, J. Bito, B. S. Cook, and M. M. Tentzeris, “Fully inkjet-printed multilayer microstrip and t-resonator structures for the rf characterization of printable materials and interconnects,” *International Microwave Symposium*, pp. 1–3, 2014
9. G. McKerricher, D. Conchouso, B. S. Cook, I. Foulds, and A. Shamim, “A low-cost inkjet printed microwave microfluidic device for crude oil/waver cut sensing,” *microTAS*, pp. 1–3, 2013
10. B. S. Cook, C. Mariotti, D. Revier, J. R. Cooper, L. Aluigi, and M. M. Tentzeris, “Inkjet-printed, vertically-integrated, high-performance inductors and transformers on flexible lcp substrate,” *International Microwave Symposium*, pp. 1–3, 2014
11. Y. Kawahara, S. Hodges, B. S. Cook, C. Zhang, and G. D. Abowd, “Instant inkjet circuits: lab-based inkjet printing to support rapid prototyping of ubicomp devices,” in *Proceedings of the 2013 ACM international joint conference on Pervasive and*

ubiquitous computing, pp. 363–372, ACM, 2013

12. B. S. Cook and M. M. Tentzeris, "A miniaturized wearable high gain and wideband inkjet-printed amc antenna," *Proceedings of the 2013 APS/URSI Symposium*, pp. 1–2, 2013
13. *Design and simulation of a slotted patch antenna sensor for wireless strain sensing*, vol. 8694, 2013
14. S. Kim, B. Cook, J. Cooper, A. Traille, A. Georgiadis, H. Aubert, and M. M. Tentzeris, "A novel dual-band retro-directive reflector array on paper utilizing substrate integrated waveguide (siw) and inkjet printing technologies for chipless rfid tag and sensor applications," in *Microwave Symposium Digest (IMS), 2013 IEEE MTT-S International*, pp. 1–4, June 2013
15. R. Vyas, B. Cook, Y. Kawahara, and M. Tentzeris, "A self-sustaining, autonomous, wireless-sensor beacon powered from long-range, ambient, rf energy," in *Microwave Symposium Digest (IMS), 2013 IEEE MTT-S International*, pp. 1–3, June 2013
16. B. S. Cook, J. R. Cooper, S. Kim, and M. M. Tentzeris, "A novel inkjet-printed passive microfluidic rfid-based sensing platform," in *Microwave Symposium Digest (IMS), 2013 IEEE MTT-S International*, pp. 1–3, June 2013
17. X. Yi, C. Cho, Y. Wang, B. S. Cook, J. Cooper, R. Vyas, M. M. Tentzeris, and R. T. Leon, "Passive frequency doubling antenna sensor for wireless strain sensing," in *ASME 2012 Conference on Smart Materials, Adaptive Structures and Intelligent Systems*, 2013
18. T. Le, V. Lakafosis, S. Kim, B. Cook, M. M. Tentzeris, Z. Lin, and C.-p. Wong, "A novel graphene-based inkjet-printed wisp-enabled wireless gas sensor," in *Microwave Conference (EuMC), 2012 42nd European*, pp. 412–415, IEEE, 2012
19. B. S. Cook and A. Shamim, "An inkjet-printed uwb antenna on paper substrate utilizing a novel fractal matching network," in *Antennas and Propagation Society International Symposium (APSURSI), 2012 IEEE*, pp. 1–2, 2012

Patent and Provisional Filings

1. B. S. Cook and M. Tentzeris, "Inkjet printed multi-layer mm-wave antennas and passive components," 2013. Provisional Patent Filing
2. B. S. Cook, S. Georgakopoulos, and M. Tentzeris, "Origami helical antenna with accordion-style fold & origami conical spiral antenna with twisting fold," 2013. Provisional Patent Filing
3. B. S. Cook, X. Yi, C. Cho, Y. Wang, M. Tentzeris, and R. Leon, "Frequency doubling antenna sensor for wireless strain and crack sensing," 2013. Provisional Patent Filing
4. B. S. Cook and J. Herbsommer, "Direct-write printing of metallic waveguides for sub-thz signals," 2013. Patent Filing
5. B. S. Cook and J. Herbsommer, "Method and manufacturing technique to match the impedance of a dielectric waveguide with signal launching mechanism for optimum power transfer," 2013. Patent Filing
6. B. S. Cook and J. Herbsommer, "Direct-write printing of dielectric waveguides with an antenna interface for sub-thz communication," 2013. Patent Filing
7. B. S. Cook and J. Herbsommer, "Method to integrate periodical structures with dielectric waveguides to control the dispersion and frequencies response of interconnects using direct-write printing manufacturing process," 2013. Patent Filing

REFERENCES

[1] F. W. Hamilton, *History of Printing (Part 1)*. MacCalla & Co., 1918.

[2] S. for Promoting Christian Knowledge, *The History of Printing*. W. Clowes and Sons, 1855.

[3] G. Wiederrecht, *Handbook of Nanofabrication*. Elsevier, 2009.

[4] L. Yang, A. Rida, R. Vyas, , and M. M. Tentzeris, "Rfid tag and rf structures on a paper substrate using inkjet-printing technology," *Ieee Transactions on Microwave Theory and Techniques*, vol. 55, 2007.

[5] G. Orecchini, F. Alimenti, V. Palazzari, A. Rida, and M. M. Tentzeris, "Design and fabrication of ultra-low cost radio frequency identification antennas and tags exploiting paper substrates and inkjet printing technology," *IET Microwaves Antennas & Propagation*, vol. 5, pp. 993–1001, 2011.

[6] Inkjet-Flex. http://www.inkjetflex.com/, 2013. Applications - RFID Antennas.

[7] D. Angmo, J. Sweelssen, R. Andriessen, Y. Galagan, and F. C. Krebs, "Inkjet printing of back electrodes for inverted polymer solar cells," *Advanced Energy Materials*, 2013.

[8] D. Angmo, T. T. Larsen-Olsen, M. Jrgensen, R. R. Sndergaard, and F. C. Krebs, "Roll-to-roll inkjet printing and photonic sintering of electrodes for ito free polymer solar cell modules and facile product integration," *Advanced Energy Materials*, vol. 3, no. 2, pp. 172–175, 2013.

[9] J. Kim, S.-I. Na, and H.-K. Kim, "Inkjet printing of transparent inznsno conducting electrodes from nano-particle ink for printable organic photovoltaics," *Solar Energy Materials and Solar Cells*, vol. 98, no. 0, pp. 424 – 432, 2012.

[10] Optomec. http://www.optomec.com, 2013. Optomec - Solar Cell Platform.

[11] L. Yang, R. Zhang, D. Staiculescu, C. P. Wong, and M. M. Tentzeris, "A novel conformal rfid-enabled module utilizing inkjet-printed antennas and carbon nanotubes for gas-detection applications," *IEEE Antennas and Wireless Propagation Letters*, vol. 8, pp. 653–656, 2009.

[12] Y. Kawahara, S. Hodges, B. S. Cook, C. Zhang, and G. D. Abowd, "Instant inkjet circuits: lab-based inkjet printing to support rapid prototyping of ubicomp devices," in *Proceedings of the 2013 ACM international joint conference on Pervasive and ubiquitous computing*, pp. 363–372, ACM, 2013.

[13] T-Ink. http://www.t-ink.com/, 2013. T-Ink's conductive and sensing inks for consumer and wearable electronics.

[14] A. N. Saxena, *Invention of Integrated Circuits: Untold Important Facts*. World Scientific, 2009.

[15] W. Bosshart, *Printed Circuit Boards: Design and Technology*. McGraw-Hill, 1983.

[16] LPKF. http://lpkfusa.com/, 2013. LPKF Laser Etching Prototyping Tools.

[17] G. Schammler, V. Glaw, and G. Chmiel, "Comparison of the metallization of chemically and laser-etched structures in bpda-pda polyimide," *Components, Hybrids, and Manufacturing Technology, IEEE Transactions on*, vol. 16, no. 7, pp. 720–723, 1993.

[18] M. Mrksich and G. M. Whitesides, "Patterning self-assembled monolayers using microcontact printing: a new technology for biosensors?," *TIBTECH*, vol. 13, pp. 228–235, 1995.

[19] A. D. la Fuente Vornbrock, "Roll printed electronics: Development and scaling of gravure printing techniques," tech. rep., Electrical Engineering and Computer Sciences University of California at Berkeley, 2009.

[20] VTT, "Final vision document in r2r printed electronics manufacturing equiptment, production lines and systems," tech. rep., VTT, Finland, 2009.

[21] W. Yin, D.-H. Lee, J. Choi, C. Park, and S. M. Cho, "Screen printing of silver nanoparticle suspension for metal interconnects," *Korean Journal of Chemical Engineering*, vol. 25, pp. 1358–1361, 2008.

[22] J. Atkinson, A. Cranny, and C. S. de Cloke, "A low-cost oxygen sensor fabricated as a screen-printed semiconductor device suitable for unheated operation at ambient temperatures," *Sensors and Actuators B: Chemical*, vol. 47, pp. 171–180, 1998.

[23] X.-F. Zhang, Q. Xu, D. Zhan, H.-X. Liu, W. Chen, and D.-P. Huang, "Dielectric evaluation of electrically tunable ba0.6sr0.4tio3 thick films prepared by screen printing," *Ceramics International*, vol. 38, no. 4, pp. 3465 – 3472, 2012.

[24] B. Cook and A. Shamim, "Inkjet printing of novel wideband and high gain antennas on low-cost paper substrate," *Antennas and Propagation, IEEE Transactions on*, vol. 60, no. 9, pp. 4148–4156, 2012.

[25] K.-H. Choi, K. Rahman, N. M. Muhammad, A. Khan, K.-R. Kwon, Y.-H. Doh, and H.-C. Kim, *Recent Advances in Nanofabrication Techniques and Applications*. InTech, 2011.

[26] T. Hamazaki and N. Morita, "Ejection charamteristics and drop modulation of acoustic inkjet printing using fresnel lens," *Journal of Fluid Science and Technology*, vol. 2, pp. 25–36, 2009.

[27] Y. ZhouPing, H. YongAn, B. NingBin, W. XiaoMei, and X. YouLun, "Inkjet printing for flexible electronics: Materials, processes and equipments," *Chinese Science Bulletin*, vol. 55, pp. 3383–3407, 2010.

[28] S. Magdassi, *The Chemistry of Inkjet Inks*. World Scientific Publishing Company, Incorporated, 2010.

[29] B. Derby, "Inkjet printing of functional and structural materials: Fluid property requirements, feature stability, and resolution," *Annual Review of Materials Research*, vol. 40, pp. 395–414, 2010.

[30] N. Reis and B. Derby, "Ink jet deposition of ceramic suspensions: modelling and experiments of droplet formation," *MRS Symp. Proc.*, vol. 624, pp. 65–70, 2000.

[31] P. C. Duineveld, M. M. de Kok, M. Buechel, A. Sempel, K. A. H. Mutsaers, P. van de Weijer, I. G. J. Camps, T. van de Biggelaar, J.-E. J. M. Rubingh, and E. I. Haskal, "Ink-jet printing of polymer light-emitting devices," *Proc. SPIE*, vol. 4464, pp. 59–67, 2002.

[32] R. Bhola and S. Chandra, "Parameters controlling solidification of molten wax droplets falling on a solid surface," *Journal of Materials Science*, vol. 34, p. 48834894, 1999.

[33] E. Tekin, B.-J. de Gans, and U. S. Schubert, "Ink-jet printing of polymers - from single dots to thin film libraries," *J. Mater. Chem.*, vol. 14, pp. 2627–2632, 2004.

[34] L. Korson, W. Drost-Hansen, and F. J. Millero, "Viscosity of water at various temperatures," *The Journal of Physical Chemistry*, vol. 78, pp. 34–39, 1968.

[35] G. Gittens, "Variation of surface tension of water with temperature," *Journal of Colloid and Interface Science*, vol. 30, p. 406412, 1969.

[36] H. Wijshoff, *Structure and fluid-dynamics in piezo inkjet printheads*. PhD thesis, Universiteit Twente, 2008.

[37] D. Bogy and F. Talke, "Experimental and theoretical study of wave propagation phenomena in drop-on-demand inkjet devices," *Journal of Research and Development*, vol. 28, pp. 314–321, 1984.

[38] B. Antohe and D. Wallace, "Acoustic phenomena in a demand mode piezoelectric inkjet printer," *Image Science Technology*, vol. 46, pp. 409–414, 2002.

[39] M. Ezzeldin, P. van den Bosch, and S. Weiland, "Improving the performance of an inkjet printhead using model predictive control," *Preprints of the 18th IFAC World Congress*, pp. 11544 – 11549, 2011.

[40] Attension, "Surface free energy - background, calculation and examples by using contact angle measurements," tech. rep., Attension, 2014.

[41] A. Yarin, "Drop impact dynamics: Splashing, spreading, receding, bouncing," *Annual Review of Fluid Mechanics*, vol. 38, no. 1, pp. 159–192, 2006.

[42] J. Stringer and B. Derby, "Formation and stability of lines produced by inkjet printing," *Langmuir*, vol. 26, no. 12, pp. 10365–10372, 2010. PMID: 20481461.

[43] F. Egitto and L. Matienzo, "Plasma modification of polymer surfaces for adhesion improvement," *IBM Journal of Research and Development*, vol. 38, no. 4, pp. 423–439, 1994.

[44] S. Lee, K. Shin, J. Hwang, K. Kang, and H. Kang, "Silver inkjet printing with control of surface energy and substrate temperature," *Journal of micromechanics and microengineering*, vol. 18, no. 7, p. 075014, 2008.

[45] D. Janssen, R. D. Palma, S. Verlaak, P. Heremans, and W. Dehaen, "Static solvent contact angle measurements, surface free energy and wettability determination of various self-assembled monolayers on silicon dioxide," *Thin Solid Films*, vol. 515, no. 4, pp. 1433 – 1438, 2006.

[46] Y. Yuan and T. R. Lee, *Contact Angle and Wetting Properties*. Springer, 2013.

[47] J. Fukai, Y. Shiiba, T. Yamamoto, O. Miyatake, D. Poulikakos, C. Megaridis, and Z. Zhao, "Wetting effects on the spreading of a liquid droplet colliding with a flat surface: experiment and modeling," *Physics of Fluids*, vol. 7, p. 236, 1995.

[48] J. Fukai, Z. Zhao, D. Poulikakos, C. M. Megaridis, and O. Miyatake, "Modeling of the deformation of a liquid droplet impinging upon a flat surface," *Physics of Fluids A: Fluid Dynamics*, vol. 5, p. 2588, 1993.

[49] R. Craster, O. Matar, and K. Sefiane, "Pinning, retraction, and terracing of evaporating droplets containing nanoparticles," *Langmuir*, vol. 25, no. 6, pp. 3601–3609, 2009.

[50] G. Shaker, S. Safavi-Naeini, N. Sangary, and M. Tentzeris, "Inkjet printing of ultrawideband (uwb) antennas on paper-based substrates," *Antennas and Wireless Propagation Letters, IEEE*, vol. 10, pp. 111–114, 2011.

[51] G. Orecchini, F. Alimenti, V. Palazzari, A. Rida, M. Tentzeris, and L. Roselli, "Design and fabrication of ultra-low cost radio frequency identification antennas and tags exploiting paper substrates and inkjet printing technology," *Microwaves, Antennas Propagation, IET*, vol. 5, no. 8, pp. 993–1001, 2011.

[52] L. Yang and M. Tentzeris, "Design and characterization of novel paper-based inkjet-printed rfid and microwave structures for telecommunication and sensing applications," in *Microwave Symposium, 2007. IEEE/MTT-S International*, pp. 1633–1636, 2007.

[53] H. ling Kao, C.-L. Cho, L.-C. Chang, C.-S. Yeh, B.-W. Wang, and H.-C. Chiu, "Inkjet printing rf bandpass filters on liquid crystal polymer substrates," *Thin Solid Films*, no. 0, 2013.

[54] A. Sridhar, J. Reiding, H. Adelaar, F. Achterhoek, D. J. van Dijk, and R. Akkerman, "Inkjet-printing- and electroless-plating- based fabrication of rf circuit structures on high-frequency substrates," *Journal of Micromechanics and Microengineering*, vol. 19, pp. 1–11, 2009.

[55] S. Molesa, D. R. Redinger, D. C. Huang, and V. Subramanian, "High-quality inkjet-printed multilevel interconnects and inductive components on plastic for ultra-low-cost rfid applications," *Proceedings of the Materials Research Society Symposium*, vol. 769, 2003.

[56] A. Menicanin, L. Zivanov, M. Damnjanovic, A. Maric, and N. Samardzic, "Ink-jet printed cpw inductors in flexible technology," in *MIPRO, 2012 Proceedings of the 35th International Convention*, pp. 233–236, 2012.

[57] S. M. Bidoki, J. Nouri, and A. A. Heidari, "Inkjet deposited circuit components," *Journal of Micromechanics and Microengineering*, vol. 20, pp. 1–7, 2010.

[58] Y. Gao, H. Li, and J. Liu, "Directly writing resistor, inductor and capacitor to composite functional circuits: A super-simple way for alternative electronics," *PLOS*, 2013.

[59] J. Newman and A. Turner, "Ink-jet printing for the fabrication of amperometric glucose biosensors," *Analytrca Chumca Acta*, vol. 262, pp. 13–17, 1992.

[60] T. Kawase, H. Sirringhaus, R. H. Friend, and T. Shimoda, "Inkjet printed via-hole interconnections and resistors for all-polymer transistor circuits," *Advanced Materials*, vol. 21, pp. 1601–1605, 2001.

[61] C. tse Chu, "Inkjet printing of flexible circuits on polymer substrates," tech. rep., Materials Research Institute, 1999.

[62] J. Szczecha, C. Megaridisa, and D. G. J. Zhanga, "Manufacture of microelectronic circuitry by drop-on-demand dispensing of nano-particle liquid suspensions," *MRS Proceedings*, vol. 624, pp. 23–28, 2000.

[63] D. Soltman and V. Subramanian, "Inkjet-printed line morphologies and temperature control of the coffee ring effect," *American Chemical Society*, pp. 1–8, 2007.

[64] M. Nikfalazar, M. Sazegar, A. Friederich, C. Kohler, Y. Zheng, A. W. J. Binder, and R. Jakoby, "Inkjet printed bst thick-films for x-band phase shifter and phased array applications," *2013 International Workshop on Antenna Technology (iWAT)*, pp. 1–4, 2013.

[65] T. Kaydanova, A. Miedaner, J. Perkins, C. Curtis, J. Alleman, and D. Ginley, "Direct-write inkjet printing for fabrication of barium strontium titanate-based tunable circuits," *Thin Solid Films*, vol. 515, no. 78, pp. 3820 – 3824, 2007.

[66] K. Kirschenmann, K. Whites, and S. Woessner, "Inkjet printed microwave frequency multilayer antennas," in *Antennas and Propagation Society International Symposium, 2007 IEEE*, pp. 924–927, 2007.

[67] B. S. Cook and A. Shamim, "An inkjet-printed uwb antenna on paper substrate utilizing a novel fractal matching network," in *Antennas and Propagation Society International Symposium (APSURSI), 2012 IEEE*, pp. 1–2, 2012.

[68] B. Cook and A. Shamim, "Utilizing wideband amc structures for high-gain inkjet-printed antennas on lossy paper substrate," *Antennas and Wireless Propagation Letters, IEEE*, vol. 12, pp. 76–79, 2013.

[69] D. Mager, A. Peter, L. Del Tin, E. Fischer, P. Smith, J. Hennig, and J. Korvink, "An mri receiver coil produced by inkjet printing directly on to a flexible substrate," *Medical Imaging, IEEE Transactions on*, vol. 29, no. 2, pp. 482–487, 2010.

[70] H. Lee, M. Tentzeris, Y. Kawahara, and A. Georgiadis, "Novel inkjet-printed ferromagnetic-based solutions for miniaturized wireless power transfer (wpt) inductors and antennas," in *Antennas and Propagation (ISAP), 2012 International Symposium on*, pp. 14–17, 2012.

[71] R. Moro, M. Bozzi, S. Kim, and M. Tentzeris, "Novel inkjet-printed substrate integrated waveguide (siw) structures on low-cost materials for wearable applications," in *Microwave Conference (EuMC), 2012 42nd European*, pp. 72–75, 2012.

[72] Y. Liu, T. Cui, and K. Varahramyan, "All-polymer capacitor fabricated with inkjet printing technique," *Solid-State Electronics*, vol. 47, no. 9, pp. 1543 – 1548, 2003.

[73] C. Sriprachuabwong, C. Srichan, T. Lomas, and A. Tuantranont, "Simple rc low pass filter circuit fabricated by unmodified desktop inkjet printer," in *Electrical Engineering/Electronics Computer Telecommunications and Information Technology (ECTI-CON), 2010 International Conference on*, pp. 929–932, 2010.

[74] J. Lim, J. Kim, Y. J. Yoon, H. Kim, H. G. Yoon, S.-N. Lee, and J. Kim, "All-inkjet-printed metal-insulator-metal (mim) capacitor," *Current Applied Physics*, vol. 12, Supplement 1, pp. 14 – 17, 2012.

[75] S. H. Ko, J. Chung, H. Pan, C. P. Grigoropoulos, and D. Poulikakos, "Fabrication of multilayer passive and active electric components on polymer using inkjet printing and low temperature laser processing," *Sensors and Actuators A: Physical*, vol. 134, no. 1, pp. 161 – 168, 2007.

[76] Y. Li, R. Torah, S. Beeby, and J. Tudor, "An all-inkjet printed flexible capacitor for wearable applications," in *Design, Test, Integration and Packaging of MEMS/-MOEMS (DTIP), 2012 Symposium on*, pp. 192–195, 2012.

[77] Y. Li, R. Torah, S. Beeby, and J. Tudor, "An all-inkjet printed flexible capacitor on a textile using a new poly(4-vinylphenol) dielectric ink for wearable applications," in *Sensors, 2012 IEEE*, pp. 1–4, 2012.

[78] B. J. Kang, C. K. Lee, and J. H. Oh, "All-inkjet-printed electrical components and circuit fabrication on a plastic substrate," *Microelectronic Engineering*, vol. 97, pp. 251 – 254, 2012.

[79] F. Dimatix, "Dimatix industrial inkjet printheads." *http* : *//www.fujifilmusa.com/products/industrial_inkjet_printheads/*.

[80] J. Andreas, E. Hauser, and W. Tucker, "Boundary tension by pendant drops1," *The Journal of Physical Chemistry*, vol. 42, no. 8, pp. 1001–1019, 1938.

[81] C. E. Stauffer, "The measurement of surface tension by the pendant drop technique," *The Journal of Physical Chemistry*, vol. 69, no. 6, pp. 1933–1938, 1965.

[82] J. Drelich, C. Fang, and C. White, "Measurement of interfacial tension in fluid-fluid systems," *Encyclopedia of Surface and Colloid Science*, pp. 3152–3166, 2002.

[83] J. Cheon, J. Lee, and J. Kim, "Inkjet printing using copper nanoparticles synthesized by electrolysis," *Thin Solid Films*, vol. 520, no. 7, pp. 2639–2643, 2012.

[84] S. Magdassi, M. Grouchko, and A. Kamyshny, "Copper nanoparticles for printed electronics: routes towards achieving oxidation stability," *Materials*, vol. 3, no. 9, pp. 4626–4638, 2010.

[85] I. Kim and J. Kim, "The effect of reduction atmospheres on the sintering behaviors of inkjet-printed cu interconnectors," *Journal of applied physics*, vol. 108, no. 10, pp. 102807–102807, 2010.

[86] D. Yiamsawas, V. Lauruengtana, U. Ruktanonchai, and W. Kangwansupamongkon, "Synthesis of poly(vinyl pyrrolidone)-stabilized silver nanoparticles," in *Nano/Micro Engineered and Molecular Systems, 2007. NEMS '07. 2nd IEEE International Conference on*, pp. 1089–1092, 2007.

[87] T. M. D. Dang, T. T. T. Le, E. Fribourg-Blanc, and M. C. Dang, "Influence of surfactant on the preparation of silver nanoparticles by polyol method," *Advances in Natural Sciences: Nanoscience and Nanotechnology*, vol. 3, no. 3, p. 035004, 2012.

[88] C. Reichardt and T. Welton, *Solvents and Solvent Effects in Organic Chemistry, Fourth Edition*. Wiley, 2010.

[89] DYNESONLINE, "Viscosity, surface tension, specific density and molecular weight of selected liquids." *http* : *//www.dynesonline.com/visc_table.html*.

[90] D. S. Viswanath, *Viscosity of Liquids: Theory, Estimation, Experiment, and Data*. Springer, 2007.

[91] B. S. Cook, Y. Fang, S. Kim, T. Le, B. Goodwin, K. H. Sandhage, and M. M. Tentzeris, "Inkjet catalyst printing and electroless copper deposition for low-cost patterned microwave passive devices on paper," *Electronic Materials Letters*, vol. In Press, 2013.

[92] I. M. Hutchings and G. D. Martin, eds., *Inkjet Technology for Digital Fabrication*. Wiley, 2013.

[93] C. Antonio, *Charcterization and Optimisation of the Variable Frequency Micrwave Technique and its Application to Microfabrication*. PhD thesis, Swiburne University of Technology, 2006.

[94] J.-T. Chen and H.-P. Chu, "Densities and viscosities for binary mixtures of ethyl lactate with methacrylic acid, benzyl methacrylate, and 2-hydroxyethyl methacrylate at (298.15, 308.15, and 318.15) k," *Journal of Chemical & Engineering Data*, vol. 52, no. 2, pp. 650–654, 2007.

[95] V. Sanchez-Romaguera, M.-B. Madec, and S. G. Yeates, "Inkjet printing of 3d metal–insulator–metal crossovers," *Reactive and Functional Polymers*, vol. 68, no. 6, pp. 1052–1058, 2008.

[96] MicroChem, "Su-8 2000 permanent epoxy negative photoresist, processing guidelines," tech. rep., www.microchem.com, 2014.

[97] D. Markovic, B. Jokanovic, M. Marjanovic, and M. Djordjevic, "Improved method for measurement of the dielectric properties of microwave substrates using microstrip t-resonator," *Instrumentation and Measurement*, 2007.

[98] K. P. Latti, M. Kettunen, J. P. Stoem, and P. Silventoinen, "A review of microstrip t-resonator method in determining the dielectric properties of printed circuit board materials," *IEEE Transactions on Instrumentation and Measurement*, vol. 56, pp. 1845–50, 2007.

[99] A. R. Fulford and S. M. Wentworth, "Conductor and dielectric-property extraction using microstrip tee resonators," *Microwave and Optical Technology Letters*, vol. 47, pp. 14–16, 2005.

[100] R. K. Hoffmann, *Handbook of Microwave Integrated Circuits*. Artech House, 1987.

[101] B. Tehrani, J. Bito, B. S. Cook, and M. M. Tentzeris, "Fully inkjet-printed multilayer microstrip and t-resonator structures for the rf characterization of printable materials and interconnects," *International Microwave Symposium*, pp. 1–3, 2014.

[102] A. Ghannam, C. Viallon, D. Bourrier, and T. parra, "Dielectric microwave characterization of the su-8 thick resin used in an above ic process," *Proceedings of the 39th European Microwave Conference*, pp. 1041–1044, 2009.

[103] I.-y. Lee, H.-Y. Park, J.-h. Park, G. Yoo, M.-H. Lim, J. Park, R. Servin, W.-S. Jung, J. Kim, S.-W. Kim, Y. Roh, G.-H. Kim, and J.-H. Park, "Poly-4-vinylphenol and poly(melamine-co-formaldehyde)-based graphene passivation method for flexible, wearable and transparent electronics," *Nanoscale*, 2014.

[104] F.-C. Chen, C.-W. Chu, J. He, Y. Yang, and J.-L. Lin, "Organic thin-film transistors with nanocomposite dielectric gate insulator," *Applied Physics Letters*, vol. 85, no. 15, pp. 3295–3297, 2004.

[105] M. Hwang, H. S. Lee, Y. Jang, J. H. Cho, S. Lee, K. Cho, *et al.*, "Effect of curing conditions of a poly (4-vinylphenol) gate dielectric on the performance of a pentacene-based thin film transistor," *Macromolecular Research*, vol. 17, no. 6, pp. 436–440, 2009.

[106] Y. Jang, D. H. Kim, Y. D. Park, J. H. Cho, M. Hwang, and K. Cho, "Influence of the dielectric constant of a polyvinyl phenol insulator on the field-effect mobility of a pentacene-based thin-film transistor," *Applied Physics Letters*, vol. 87, no. 15, pp. 152105–152105, 2005.

[107] T. A and M. University, "Thermodynamic tables of non hydrocarbons, thermodynamic research center," tech. rep., Texas A and M University, 1994.

[108] C. J. Chiu, Z. W. Pei, S. P. Chang, and S. J. Chang, "Influence of weight ratio of poly(4-vinylphenol) insulator on electronic properties of ingazno thin-film transistor," *Journal of Nanomaterials*, vol. 2012, pp. 1–7, 2012.

[109] F.-C. Chen, C.-W. Chu, J. He, Y. Yang, and J.-L. Lin, "Organic thin-film transistors with nanocomposite dielectric gate insulator," *Applied physics letters*, vol. 85, no. 15, pp. 3295–3297, 2004.

[110] S. Zhang, X. Jin, P. C. Painter, and J. Runt, "Broad-band dielectric study on poly (4-vinylphenol)/poly (ethyl methacrylate) blends," *Macromolecules*, vol. 35, no. 9, pp. 3636–3646, 2002.

[111] D. Li and J. Brisson, "Dmta and ftir investigation of the phase behavior of poly (methyl methacrylate)-poly (4-vinylphenol) blends," *Macromolecules*, vol. 29, no. 3, pp. 868–874, 1996.

[112] B. Cook, J. Cooper, and M. Tentzeris, "Multi-layer rf capacitors on flexible substrates utilizing inkjet printed dielectric polymers," *Microwave and Wireless Components Letters, IEEE*, vol. 23, no. 7, pp. 353–355, 2013.

[113] B. S. Cook, C. Mariotti, D. Revier, J. R. Cooper, L. Aluigi, and M. M. Tentzeris, "Inkjet-printed, vertically-integrated, high-performance inductors and transformers on flexible lcp substrate," *International Microwave Symposium*, pp. 1–3, 2014.

[114] A. Menicanin, L. Zivanov, M. Damnjanovic, and A. Maric, "Low-cost cpw meander inductors utilizing ink-jet printing on flexible substrate for high-frequency applications," *Electron Devices, IEEE Transactions on*, vol. 60, no. 2, pp. 827–832, 2013.

[115] D. Redinger, S. Molesa, S. Yin, R. Farschi, and V. Subramanian, "An ink-jet-deposited passive component process for rfid," *IEEE TRANSACTIONS ON ELECTRON DEVICES*, vol. 51, pp. 1978–1983, 2004.

[116] L. Yang, A. Rida, R. Vyas, , and M. M. Tentzeris, "Rfid tag and rf structures on a paper substrate using inkjet-printing technology," *Ieee Transactions on Microwave Theory and Techniques*, vol. 55, 2007.

[117] G. Shaker, S. Safavi-Naeini, N. Sangary, and M. M. Tentzeris, "Inkjet printing of ultrawideband (uwb) antennas on paper-based substrates," *IEEE Antennas and Wireless Propagation Letters*, vol. 10, pp. 111–114, 2011.

[118] B. S. Cook, B. Tehrani, J. Cooper, and E. Tentzeris, "Multi-layer inkjet printing of millimeter-wave proximity-fed patch arrays on flexible substrates," *IEEE Antennas and Wireless Propagation Letters*, 2013.

[119] S. Vajha and S. Prasad, "Design and modeling of proximity coupled patch antenna," *IEEE-APS Conference on Antennas and Propagation for Wireless Communications*, pp. 43–46, 2000.

[120] C. Balanis, ed., *Modern Antenna Handbook*. John Wiley & Sons, 2008.

[121] A. W. Martinez, S. T. Phillips, B. J. Wiley, M. Gupta, and G. M. Whitesides, "Flash: A rapid method for prototyping paper-based microfluidic devices," *Lab on a Chip*, vol. 8, pp. 2146–2150, 2008.

[122] H. Klank, J. P. Kutter, and O. Geschke, "Co2-laser micromachining and back-end processing for rapid production of pmma-based microfluidic systems," *Lab on a Chip*, vol. 2, pp. 242 – 246, 2002.

[123] P. K. Yuen and V. N. Goral, "Low-cost rapid prototyping of flexible microfluidic devices using a desktop digital craft cutter," *Lab on a Chip*, vol. 10, pp. 384–387, 2010.

[124] B. S. Cook, J. R. Cooper, S. Kim, and M. M. Tentzeris, "A novel inkjet-printed passive microfluidic rfid-based sensing platform," in *Microwave Symposium Digest (IMS), 2013 IEEE MTT-S International*, pp. 1–3, June 2013.

[125] K. Shibata, "Measurement of complex permittivity for liquid materials using the open-ended cut-off waveguide reflection method," *Microwave Conference Proceedings (CJMW)*, pp. 1 – 4, 2011.

[126] A. Tidar, S. Shafiyoddin, S. Kamble, G. Dharne, S. S. Patil, P. W. Khirade3, and s.c. Mehrotra*, "Microwave dielectric relaxation study of 1-hexanol with j-propenol mixture by using time domain reflectometry at 300k," *Applied Electromagnetics Conference (AEMC)*, pp. 1–4, 2009.

[127] N. Wiwatcharagoses, K. Y. Park, and J. Hejase, "Microwave artificially structured periodic media microfluidic sensor," *Proceedings IEEE Electronic Components and Technology Conference*, pp. 1889–1893, 2011.

[128] N. Orloff, M. Rinehart, and J. Booth, "Broadband permittivity of liquids extracted from transmission line measurements of microfluidic channels," *Proceedings IEEE/MTT-S International Microwave Symposium*, pp. 523 – 526, 2007.

[129] K. Grenier, D. Dubuc, P. Poleni, M. TKumemura, H. Toshiyoshi, T. Fujii, and H. Fujita, "New broadband and contact less rf / microfluidic sensor dedicated to bioengineering," *IEEE Transactions on Microwave Theory and Techniques*, pp. 1329 – 1332, 2009.

[130] S. Pavuluri, R. Lopez-Villarroya, E. McKeever, G. Goussetis, M. Desmulliez, and D. Kavanagh, "Integrated microfluidic capillary in a waveguide resonator for chemical and biomedical sensing," *Journal of Physics: Conference Series*, vol. 178, pp. 1–6, 2009.

[131] K. Grenier, D. Dubuc, P.-E. Poleni, M. Kumemura, H. Toshiyoshi, T. Fujii, and H. Fujita, "Integrated broadband microwave and microfluidic sensor dedicated to bioengineering," *Microwave Theory and Techniques, IEEE Transactions on*, vol. 57, no. 12, pp. 3246–3253, 2009.

[132] T. Chretiennot, D. Dubuc, and K. Grenier, "A microwave and microfluidic planar resonator for efficient and accurate complex permittivity characterization of aqueous solutions," *Microwave Theory and Techniques, IEEE Transactions on*, vol. 61, no. 2, pp. 972–978, 2013.

[133] M. Hofmann, G. Fischer, R. Weigel, and D. Kissinger, "Microwave-based noninvasive concentration measurements for biomedical applications," *Microwave Theory and Techniques, IEEE Transactions on*, vol. 61, no. 5, pp. 2195–2204, 2013.

[134] B. Laemmle, K. Schmalz, J. Scheytt, R. Weigel, and D. Kissinger, "A 125-ghz permittivity sensor with read-out circuit in a 250-nm sige bicmos technology," *Microwave Theory and Techniques, IEEE Transactions on*, vol. 61, no. 5, pp. 2185–2194, 2013.

[135] V. Sekar, W. Torke, S. Palermo, and K. Entesari, "A self-sustained microwave system for dielectric-constant measurement of lossy organic liquids," *Microwave Theory and Techniques, IEEE Transactions on*, vol. 60, no. 5, pp. 1444–1455, 2012.

[136] J. A. Gordon, C. L. Holloway, J. C. Booth, J. R. Baker-Jarvis, D. R. Novotny, S. Kim, and Y. Wang, "Fluid interactions with metafilm/metasurfaces for tuning, sensing, and microwave assisted chemical processes," *Physical Review B*, vol. B83, pp. 205130–1 – 205130–5, 2011.

[137] J. Obrzut, A. Anopchenko, K. Kano, and H. Wang, "High frequency loss mechanism in polymers filled with dielectric modifiers," *Materials Research Society Symposium Proceedings*, vol. 783, pp. B3.5.1 – B3.5.6, 2004.

[138] A. Sihvola, "Mixing rules with complex dielectric coefficients," *Subsurface Sensing Technologies and Applications*, vol. 1, pp. 393–415, 2000.

[139] T. Chen, D. Dubuc, M. Poupot, J. Fournie, and K. Grenier, "Accurate nanoliter liquid characterization up to 40 ghz for biomedical applications: Toward noninvasive living cells monitoring," *Microwave Theory and Techniques, IEEE Transactions on*, vol. 60, no. 12, pp. 4171–4177, 2012.

[140] K. Grenier, D. Dubuc, T. Chen, F. Artis, T. Chretiennot, M. Poupot, and J. Fournie, "Recent advances in microwave-based dielectric spectroscopy at the cellular level for cancer investigations," *Microwave Theory and Techniques, IEEE Transactions on*, vol. 61, no. 5, pp. 2023 – 2030, 2013.

[141] K. P. Latti, M. Kettunen, J. P. Stoem, and P. Silventoinen, "A review of microstrip t-resonator method in determining the dielectric properties of printed circuit board materials," *IEEE Transactions on Instrumentation and Measurement*, vol. 56, pp. 1845–50, 2007.

[142] S. Kim, B. S. Cook, T. Le, A. Traille, and M. M. Tentzeris, *Materials for Substrates, Green RFID Systems*. Cambridge Press, In Press.

[143] B. S. Cook, B. Tehrani, J. R. Cooper, S. Kim, and M. M. Tentzeris, *Inkjet Printing Technology for 2D/3D Flexible Electronic Systems, Handbook of flexible organic electronics, Materials, Manufacturing and Applications*. Woodhead Publishing, In Press.

[144] S. Kim, B. S. Cook, J. R. Cooper, and M. M. Tentzeris, *Inkjet-printed Artificial Magnetic Conductor (AMC) Plane for Wearable Antennas, Advancement in Wearable and Flexible Antennas*. WIT Press, In Press.

[145] B. S. Cook, "The future of inkjet printed electronics," *Circuit Cellar Magazine*, 2014.

[146] B. Cook, T. Le, S. Palacios, A. Traille, and M. Tentzeris, "Only skin deep: Inkjet-printed zero-power sensors for large-scale rfid-integrated smart skins," *Microwave Magazine, IEEE*, vol. 14, no. 3, pp. 103–114, 2013.

[147] B. Cook, J. Cooper, and M. Tentzeris, "An inkjet-printed microfluidic rfid-enabled platform for wireless lab-on-chip applications," *Microwave Theory and Techniques, IEEE Transactions on*, vol. 61, pp. 4714–4723, Dec 2013.

[148] S. Kim, B. Cook, T. Le, J. Cooper, H. Lee, V. Lakafosis, R. Vyas, R. Moro, M. Bozzi, A. Georgiadis, *et al.*, "Inkjet-printed antennas, sensors and circuits on paper substrate," *IET Microwaves, Antennas & Propagation*, vol. 7, no. 10, pp. 858–868, 2013.

[149] R. Vyas, B. Cook, Y. Kawahara, and M. Tentzeris, "E-wehp: A batteryless embedded sensor-platform wirelessly powered from ambient digital-tv signals," *Microwave Theory and Techniques, IEEE Transactions on*, vol. 61, pp. 2491–2505, June 2013.

[150] B. Cook and A. Shamim, "Utilizing wideband amc structures for high-gain inkjet-printed antennas on lossy paper substrate," *Antennas and Wireless Propagation Letters, IEEE*, vol. 12, pp. 76–79, 2013.

[151] B. Cook, A. Shamim, and M. Tentzeris, "Passive low-cost inkjet-printed smart skin sensor for structural health monitoring," *Microwaves, Antennas Propagation, IET*, vol. 6, pp. 1536–1541, November 2012.

[152] A. Maza, B. Cook, G. Jabbour, and A. Shamim, "Paper-based inkjet-printed ultra-wideband fractal antennas," *IET Microwaves, Antennas & Propagation*, vol. 6, no. 12, pp. 1366–1373, 2012.

[153] B. Tehrani, B. S. Cook, J. R. Cooper, and M. M. Tentzeris, "Inkjet printing of a wideband, high gain mm-wave vivaldi antenna on a flexible organic substrate," in *APS/URSI 2014*, 2014.

[154] B. Tehrani, J. Bito, B. S. Cook, and M. M. Tentzeris, "Fully inkjet-printed multilayer microstrip patch antenna for ku-band applications," in *APS/URSI 2014*, 2014.

[155] W. Su, C. Marioti, B. S. Cook, and M. M. Tentzeris, "A novel inkjet-printed microfluidic tunable coplanar patch antenna," in *APS/URSI 2014*, 2014.

[156] X. Yi, B. S. Cook, Y. Wang, and M. M. Tentzeris, "Crack propagation measurement using a battery-free slotted patch antenna sensor," *7th European Workshop on Structural Health Monitoring*, 2014.

[157] S. Yao, S. V. Georgakopoulos, M. M. Tentzeris, and B. S. Cook, "A novel reconfigurable origami accordion antenna," *International Microwave Symposium*, pp. 1–3, 2014.

[158] G. McKerricher, D. Conchouso, B. S. Cook, I. Foulds, and A. Shamim, "Crude oil water-cut sensing with disposable laser ablated and inkjet printed rf microfluidics," *International Microwave Symposium*, pp. 1–3, 2014.

[159] J. R. Cooper, B. S. Cook, and M. M. Tentzeris, "The first hardware-based, anti-collision methodology for frequency doubling transceivers for rfid and wireless sensing applications," *International Microwave Symposium*, pp. 1–3, 2014.

[160] G. McKerricher, D. Conchouso, B. S. Cook, I. Foulds, and A. Shamim, "A low-cost inkjet printed microwave microfluidic device for crude oil/waver cut sensing," *microTAS*, pp. 1–3, 2013.

[161] Y. Kawahara, S. Hodges, B. S. Cook, C. Zhang, and G. D. Abowd, "Instant inkjet circuits: lab-based inkjet printing to support rapid prototyping of ubicomp devices," in *Proceedings of the 2013 ACM international joint conference on Pervasive and ubiquitous computing*, pp. 363–372, ACM, 2013.

[162] B. S. Cook and M. M. Tentzeris, "A miniaturized wearable high gain and wideband inkjet-printed amc antenna," *Proceedings of the 2013 APS/URSI Symposium*, pp. 1–2, 2013.

[163] *Design and simulation of a slotted patch antenna sensor for wireless strain sensing*, vol. 8694, 2013.

[164] S. Kim, B. Cook, J. Cooper, A. Traille, A. Georgiadis, H. Aubert, and M. M. Tentzeris, "A novel dual-band retro-directive reflector array on paper utilizing substrate integrated waveguide (siw) and inkjet printing technologies for chipless rfid tag and sensor applications," in *Microwave Symposium Digest (IMS), 2013 IEEE MTT-S International*, pp. 1–4, June 2013.

[165] R. Vyas, B. Cook, Y. Kawahara, and M. Tentzeris, "A self-sustaining, autonomous, wireless-sensor beacon powered from long-range, ambient, rf energy," in *Microwave Symposium Digest (IMS), 2013 IEEE MTT-S International*, pp. 1–3, June 2013.

[166] X. Yi, C. Cho, Y. Wang, B. S. Cook, J. Cooper, R. Vyas, M. M. Tentzeris, and R. T. Leon, "Passive frequency doubling antenna sensor for wireless strain sensing," in *ASME 2012 Conference on Smart Materials, Adaptive Structures and Intelligent Systems*, 2013.

[167] T. Le, V. Lakafosis, S. Kim, B. Cook, M. M. Tentzeris, Z. Lin, and C.-p. Wong, "A novel graphene-based inkjet-printed wisp-enabled wireless gas sensor," in *Microwave Conference (EuMC), 2012 42nd European*, pp. 412–415, IEEE, 2012.

[168] B. S. Cook and M. Tentzeris, "Inkjet printed multi-layer mm-wave antennas and passive components," 2013. Provisional Patent Filing.

[169] B. S. Cook, S. Georgakopoulos, and M. Tentzeris, "Origami helical antenna with accordion-style fold & origami conical spiral antenna with twisting fold," 2013. Provisional Patent Filing.

[170] B. S. Cook, X. Yi, C. Cho, Y. Wang, M. Tentzeris, and R. Leon, "Frequency doubling antenna sensor for wireless strain and crack sensing," 2013. Provisional Patent Filing.

[171] B. S. Cook and J. Herbsommer, "Direct-write printing of metallic waveguides for sub-thz signals," 2013. Patent Filing.

[172] B. S. Cook and J. Herbsommer, "Method and manufacturing technique to match the impedance of a dielectric waveguide with signal launching mechanism for optimum power transfer," 2013. Patent Filing.

[173] B. S. Cook and J. Herbsommer, "Direct-write printing of dielectric waveguides with an antenna interface for sub-thz communication," 2013. Patent Filing.

[174] B. S. Cook and J. Herbsommer, "Method to integrate periodical structures with dielectric waveguides to control the dispersion and frequencies response of interconnects using direct-write printing manufacturing process," 2013. Patent Filing.